8-2011

Investigation of hydrodynamic scaling relationships in shallow spouted beds

Irma Deytia Lima Rojas
ilimaroj@utk.edu

To the Graduate Council:

I am submitting herewith a dissertation written by Irma Deytia Lima Rojas entitled "Investigation of hydrodynamic scaling relationships in shallow spouted beds." I have examined the final electronic copy of this dissertation for form and content and recommend that it be accepted in partial fulfillment of the requirements for the degree of Doctor of Philosophy, with a major in Chemical Engineering.

Duane D. Bruns, Major Professor

We have read this dissertation and recommend its acceptance:

Robert M. Counce, C. Stuart Daw, Ke Nguyen, Charles E A Finney, Tsewei Wang

Accepted for the Council:
Dixie L. Thompson

Vice Provost and Dean of the Graduate School

(Original signatures are on file with official student records.)

To the Graduate Council:

I am submitting a dissertation written by Irma Deytia Lima Rojas entitled “Investigation of hydrodynamic scaling relationships in shallow spouted beds”. I have examined the final electronic copy of this dissertation and I recommend it to be accepted as fulfillment of the requirements to obtain the degree of Doctor of Philosophy, with a major in Chemical Engineering.

_____
Duane D. Bruns, Major Professor

We have read this dissertation
and recommend its acceptance:

_____
Robert M. Counce

_____
C. Stuart Daw

_____
Ke Nguyen

_____
Charles E A Finney

_____
Tsewei Wang

Acceptance for the Council:

_____
Carolyn R. Hodges
Vice Provost and Dean of the Graduate School

(Original signatures are on file with official student records.)

Investigation of hydrodynamic scaling relationships in shallow spouted beds

A Dissertation Presented for the

Doctor of Philosophy

Degree

The University of Tennessee, Knoxville

Irma Deytia Lima Rojas

August 2011

DEDICATION

I dedicate this work to my God, who is the One who has supported me until this moment and helped me in different ways with everything. God is my strength and wisdom comes from Him.

ACKNOWLEDGMENTS

I acknowledge the support from the U.S. Department of Energy and the Department of Chemical and Biomolecular Engineering at University of Tennessee, Knoxville.

I thank my first advisor, Dr. Duane D. Bruns, for his help and instructions for this dissertation.

I thank my co-advisors, Dr. Ke Nguyen, Dr. Stuart Daw. Dr. Charles Finney, Dr. Tsewei Wang and Dr. Robert Counce, for their support and advising during the last two years.

I also want to thank my colleagues, Jiandong Zhou and Alok Patel, for their help in introducing me to the experimental measurement system.

I thank Messrs. Douglas E. Fielden, Dan Hackworth and Larry Smith for their help in the fabrication and design of mechanical and electronic parts of the experimental system.

I want to thank the administration, faculty and staff of the Department of Chemical and Biomolecular Engineering of the University of Tennessee, Knoxville for the guidance and help.

Finally I thank my family for their support to date.

ABSTRACT

Important global hydrodynamic relationships for shallow spouted beds of high-density particles were characterized in terms of three features: minimum spouting velocity, overall bed pressure drop at minimum spouting velocity; and fountain height. Spouted bed literature is sparse for shallow beds (static particle depth to bed diameter ≤ 1) and beds with heavy particles (density $>$ 3000 kg/m^3). Correlations for such beds were developed here by varying column diameter, static bed height, particle diameter, particle density, gas density and gas flow in an ambient temperature and pressure bed.

The degree of correlation between each of the observed hydrodynamic features and a set of selected dimensionless groups from the literature was evaluated with principal components analysis. The minimum spouting velocity correlated strongly with the ratios of particle to bed diameter, of particle to gas density, and of static bed height to particle diameter, and weakly with Archimedes number. Overall bed pressure drop at minimum spouting correlated strongly with Archimedes number, the ratio of static bed height to particle diameter and Froude number. Fountain height correlated strongly with the ratios of the superficial gas velocity to minimum spouting velocity, of static bed height to particle diameter and of the particle to the bed diameter. Principal component regression models were developed for minimum spouting velocity, bed pressure drop, and fountain height with respect to a selected set of dimensionless parameters. All models have regression coefficient values exceeding 85%. Predictions using models developed in this study were compared with correlations in the literature and found to give better results for the experimental conditions studied. Most likely the literature models were less accurate because they were extrapolated.

Distinct bed pressure drop relationships with gas flow were observed for certain ranges of particle diameter and static bed height. In addition three dynamical spouting modes were observed, and named as regular, erratic and bimodal. A spouting regime map is proposed based on the spouting regimes defined in this investigation. The correspondence between bed pressure drop relationships and spouting regimes is still unclear.

TABLE OF CONTENT

1. Introduction and Background 1

1.1 Objectives 2

1.2 Organization of Dissertation 3

1.3 Spouted-bed applications and motivation for this study 3

1.4 Hydrodynamic scaling in spouted beds 4

1.5 Empirical correlations for spouted beds 7

2. Experimental approach and methodology 13

2.1. Experimental setup 14

3. Experimental design and data analysis methodology 27

3.1. Experimental design 28

3.2. Data analysis methodology 33

3.2.1 Obtaining linear equation to correlate each response variable with respect to chosen predictor variables 33

3.2.2 Principal Component Regression (PCR) 36

3.2.3 Recovering the coefficient $\tilde{\beta}_0$ from PCR 38

3.2.4 Data analysis 39

4. Results 40

4.1. General observations 41

4.1.1 General description of bed behavior and dynamic 41

4.1.2 Bed pressure drop profiles with fluidizing gas flow 42

4.1.3 Spouting regimes defined by fountain height dynamics 47

4.1.4 Shallow bed spouting regime map 58

4.1.5 Operating conditions of experiments used to generate hydrodynamic correlation models 59

4.2. Developing regression model for U_{ms} 66

4.2.1 Correlation pattern between U_{ms} and four chosen dimensionless variables. 66

4.2.2 Regression model developed for U_{ms} with respect to the same four dimensionless variables 70

4.2.3 Extended regression model for U_{ms} with respect to the same four dimensionless variables incorporating additional experimental results. 79

4.3. Developing regression model for ΔP_{ms} 88

4.3.1 Regression model developed for ΔP_{ms} with respect to five dimensionless variables 88

4.3.2 Reduced regression model developed for ΔP_{ms} with respect to two dimensionless variables 97

4.4. Developing regression model for H_f using four dimensionless variables 103

4.5. Final hydrodynamic correlations models for shallow spouted bed for dense particles .. 111

4.5.1 Minimum spouting velocity (U_{ms}) 111

4.5.2 Bed pressure drop at U_{ms} (ΔP_{ms}) 115

4.5.3 Fountain Height (H_f) 119

5. Conclusions 124

5.1. Conclusions 125

5.2. Future Work 126

References 128

Appendix A 132

Appendix B 157

VITA 161

LIST OF FIGURES

Figure 2.1: Schematic of the spouted-bed research facility. 14
Figure 2.2: Schematic of the spouted bed 16
Figure 2.3: Photograph showing pressure-tap locations on the 60º cone of the 50 mm bed. 17
Figure 2.4: Pressure-tap locations diagram for the 60º cone of the 50 mm bed. 18
Figure 2.5: Determination of U_{ms} in the 50 mm bed for 75 g of 500 µm of YSZ particles. 19
Figure 2.6: Geldart[1] plot with the points showing the Geldart group corresponding to the particles used in this investigation (Al_2O_3, YSZ and SS) in green. 22
Figure 2.7: Composite image at 1.65 U/U_{ms}, with 0.67 H_0/D_c of 500 µm YSZ particles. Height above the top of the cone of the bed is about 22 mm. 24
Figure 2.8: Diagram illustrating the procedure for fountain height (H_f) measurement at 1.65 U/U_{ms}, with 0.67 H_0/D_c of 500 µm YSZ particles. The vertical axis indicates the grayscale intensity determined from a pixel-by-pixel analysis along the centerline of the composite digital image. A pixel is equal to 0.22 mm. 25
Figure 2.9: Gray scaled cut slice of a frame of the fountain generated at 1.1 U/U_{ms}, with 1 H_0/D_c of 500 µm Al_2O_3 particles in the 50 mm bed showing the centroid point of the fountain 26
Figure 3.1: (a) Scree plot of the variance contributed by each principal component. (b) Cumulative contribution of each principal component. 37
Figure 4.1: Typical pressure drop across the bed behavior of a spouted bed with respect to gas velocity [21] 41
Figure 4.2: Constant profile with a discontinuity at U_{ms}: Average inlet pressure drop in the 80 mm bed as a function of U/U_{ms} for 500 µm YSZ particles at H_0/D_c=0.42 using air (U_{ms} = 0.06 m/s) and helium (U_{ms}= 0.12 m/s) as the fluidizations gases. 43
Figure 4.3: Decreasing profile with a discontinuity at U_{ms}: Average inlet pressure drop in the 80 mm bed as a function of U/U_{ms} for 1000 µm YSZ particles at H_0/D_c=0.42 (U_{ms}=0.20 m/s) and 0.67 (U_{ms}=0.34 m/s) using air as the fluidizations gas. 44
Figure 4.4: Negative pressure trend with no discontinuity at U_{ms}: Average inlet pressure drop in the 50 mm bed as a function of U/U_{ms} for 2000 µm Al_2O_3 particles at H_0/D_c=0.42 (U_{ms}=0.34 m/s) and 0.67(U_{ms}=0.68 m/s) using air as the fluidizations gas. 45
Figure 4.5: Bisectionally constant trend with discontinuity at U_{ms}: Average inlet pressure drop in the 150 mm bed as a function of U/U_{ms} for 500 µm Al_2O_3 (U_{ms}=0.05 m/s) and YSZ (U_{ms}=0.06 m/s) particles at H_0/D_c=0.42 using air as the fluidizations gas. 46
Figure 4.6: Typical fountain of a spouted bed. 47
Figure 4.7: Composite images at different gas flow rates for a typical regular case, 80 mm bed for 1000 µm YSZ (U_{ms}=0.28 m/s) particles at H_0/D_c=0.67 using air as the fluidizations gas. 49
Figure 4.8: Composite images at different gas flow rates for a typical erratic case, 50 mm bed for 500 µm Al_2O_3 (U_{ms}=0.18 m/s) particles at H_0/D_c=1 using air as the fluidizations gas. 50
Figure 4.9: Distribution of centroid distance of fountain height for typical regular (Case 10 at 1.4U_{ms}) and erratic (Case 5 at 1.2U_{ms}) spouting cases. 52
Figure 4.10: Standard deviation of centroid distance of fountain height for typical regular and erratic spouting cases. Note that the cases are defined in Table 3.2 in Section 3.1. 53

Figure 4.11: Coefficient of variation of centroid distance of fountain height with respect to gas flow rate for typical regular and erratic spouting cases. Note that the cases are defined in Table 3.2 in Section 3.1. 54
Figure 4.12: Coefficient of variation of bed pressure drop with respect of gas flow rate for typical regular and erratic spouting cases. Note that the cases are defined in Table 3.2 in Section 3.1... 55
Figure 4.14: Frames extracted from a video with respect of time for a typical bimodal showing the differences through the time of fountain height. 50 mm bed for 2000 μm Al_2O_3 ($U=1.6U_{ms}$) particles at $H_0/D_c=0.42$ using air as the fluidizations gas. 57
Figure 4.15: Preliminary shallow bed spouting regime map for different particle size, particle density, solid density, gas density, column diameter and static height..... 58
Figure 4.16: Scree plot showing the cumulative variance contributed by the principal components. 69
Figure 4.17: Scree plot showing the cumulative variance contributed by the principal components. 72
Figure 4.18: Relative make up of each principal component. 73
Figure 4.19: Measured versus predicted U_{ms}/U_t values for 30 reference data points using the regression model, showing the relatively little scattering between the measured and the predicted U_{ms} values. 75
Figure 4.20: Fitting residuals from modeling PCR, using 30 experimental points against index number of sample points, showing the even distribution around 0 (suggesting that the noise contained in the data is not biased). 76
Figure 4.21: Measured versus predicted U_{ms}/U_t values for 23 validation data points, showing the relatively little scattering between the measured and the predicted U_{ms}/U_t values. 77
Figure 4.22: Fitting residuals from modeling PCR, using 23 validation sets against index number of sample points, showing the even distribution around 0 (suggesting that the noise contained in the data is indeed Gaussian, and not biased)..... 78
Figure 4.23: Scree plot showing the cumulative variance contributed by the principal components for the reference data set..... 81
Figure 4.24: Relative make up of each principal component. 82
Figure 4.25: Measured versus predicted U_{ms}/U_t values for the 40 reference data points, showing the relatively little scattering between the measured and the predicted U_{ms}/U_t. 84
Figure 4.26: Fitting residuals from the PCR using the 40 reference sets of experimental data.... 85
Figure 4.27: Measured versus predicted U_{ms} values from the regression model for the 35 validation sets..... 86
Figure 4.28: Fitting residuals from the PCR for the 35 validation sets. 87
Figure 4.29: Scree plot showing the cumulative variance contributed by the principal components for pressure drop modeling. 90
Figure 4.30: Relative make up of each principal component. 91
Figure 4.31: Measured versus predicted $\Delta P_{ms}/(\rho_s H_0 g)$ values from the regression model showing the relatively little scattering between the measured and the predicted $\Delta P_{ms}/(\rho_s H_0 g)$ values using 27 sets of experimental data. 93
Figure 4.32: Fitting residuals from the PCR using the 27 reference sets of experimental data.... 94
Figure 4.33: Measured versus predicted $\Delta P_{ms}/(\rho_s H_0 g)$ values from the regression model for the 20 validation sets..... 95

Figure 4.34: Fitting residuals from the PCR for the 20 validation sets. 96
Figure 4.35: Measured versus predicted $\Delta P_{ms}/(\rho_s H_0 g)$ values from the regression model showing the relatively little scattering between the measured and the predicted $\Delta P/(\rho_s H_0 g)$ values using 27 sets of experimental data. 99
Figure 4.36: Fitting residuals from the PCR using the 27 reference sets of experimental data.. 100
Figure 4.37: Measured versus predicted $\Delta P_{ms}/(\rho_s H_0 g)$ values from the regression model for the 20 validation sets 101
Figure 4.38: Fitting residuals from the PCR for the 20 validation sets. 102
Figure 4.39: Scree plot showing the cumulative variance contributed by the principal components. 105
Figure 4.40: Relative make up of each principal component. 106
Figure 4.41: Measured versus predicted H_f/H_{f_max} values from the regression model showing the scattering between the measured and the predicted H_f/H_{f_max} values using 66 data points. 107
Figure 4.42: Fitting residuals from the PCR model using the 66 reference data points. 108
Figure 4.43: Measured versus predicted H_f/H_{f_max} values from the regression model for the 62 validation data points. 109
Figure 4.44: Fitting residuals from the PCR for the 62 validation data points. 110
Figure 4.45: U_{ms} measured vs. predicted by different correlations. 114
Figure 4.46: ΔP_{ms} measured vs. predicted by different correlations. 119
Figure 4.47: H_f measured vs. predicted by different correlations. 122

LIST OF TABLES

Table 1.1: Scaling studies 5
Table 1.2: Literature survey of minimum spouting correlations 8
Table 1.3: Literature survey of bed pressure drop correlations 11
Table 1.4: Literature survey of fountain height correlations 12
Table 2.1: Particle properties 20
Table 2.2: Gas properties 22
Table 3.1: Design parameters and treatment levels for factorial designed experiments 28
Table 3.2: Operating conditions for experiments performed in phase A and B 30
Table 3.3: Dimensionless $\tilde{y}$ variables 34
Table 4.1: Classification of bed pressure drop profile behavior after U_{ms} is reached. 42
Table 4.2: Classification of spouting regimes based on fountain height dynamics. 48
Table 4.3: Operating conditions of cases used to correlate bed pressure drop at minimum spouting condition 60
Table 4.4: Operating conditions of cases used to correlate fountain height 62
Table 4.5: V vectors and S values 67
Table 4.6: V vectors and S values 71
Table 4.7: V vectors and S values 80
Table 4.8: V vectors and S values 89
Table 4.9: V vectors and S values 97
Table 4.10: V vectors and S values 104
Table 4.11: Parameters variations in U_{ms} correlations 113
Table 4.12: Parameters variations in ΔP_{ms} correlations 117
Table 4.13: Parameters variations in H_f correlations 121

LIST OF ATTACHMENTS

File 1 Erratic spouted bed with 500 µm Al_2O_3 particles, H_0/D_c = 0.42 in the 150mm bed at $2.6U_{ms}$ with air as fluidizing gas (Video file) 150-Air-Al2O3-H42-500-f2.6.avi
File 2 Erratic spouted bed with 500 µm Al_2O_3 particles, H_0/D_c = 0.42 in the 150mm bed at $1.6U_{ms}$ with air as fluidizing gas (Video file) 150-Air-Al2O3-H42-500-f1.6.avi
File 3 Regular spouted bed with 500 µm YSZ particles, H_0/D_c = 1 in the 80mm bed at $1.25U_{ms}$ with air as fluidizing gas (Video file) 80-Air-YSZ-H100-500-f1.25.avi
File 4 Erratic spouted bed with 500 µm YSZ particles, H_0/D_c = 1 in the 80mm bed at $1.25U_{ms}$ with helium as fluidizing gas (Video file) 80-He-YSZ-H100-500-f1.25.avi
File 5 Bimodal spouted bed with 2000 µm Al_2O_3 particles, H_0/D_c = 0.42 in the 50mm bed at $2.5U_{ms}$ with air as fluidizing gas (Video file) 80-Air-YSZ-H100-500-f2.5.avi
File 6 Bimodal spouted bed with 2000 µm Al_2O_3 particles, H_0/D_c = 0.42 in the 50mm bed at $1.6U_{ms}$ with air as fluidizing gas (Video file) 80-Air-YSZ-H100-500-f1.6.avi

NOMENCLATURE

A	Cross sectional area of the bed
Ar	Archimedes number $Ar = \frac{d_p^3 \rho_g (\rho_p - \rho_g) g}{\mu_g^2}$
Cd	Centroid distance
CV	Coefficient of variation
d3	Variance contributed by each principal component
d4	Cummulative variance vector
d_p	Particle diameter
D_b	Upper diameter of stagnant bed
D_c	Bed cylinder diameter
D_{bc}	Cone base diameter
D_i	Inlet diameter
D_s	Spout diameter
Fr	Froude number $Fr = \frac{U^2}{g d_p}$
g	Local gravitational acceleration
G	Fluid mass flow rate at minimum spouting
G_s	Mass flux of solid
H_{bottom}	Bed bottom height
H_c	Conical section height
H_{cyl}	Bed cylinder depth
H_f	Fountain height
H_{f_max}	Maximum fountain height of specific set of experiments
H_{equiv}	Cylinder equivalent depth
H_0	Static height
L	Dimension of bed
L_1,L_2	Relevant physical dimensions of the system.
m	Charged mass
m_a	Magnification of length scale
Q_{ms}	Minimum spouting gas flow rate
Re	Reynolds number $\mathrm{Re} = \frac{\rho_s d_p U}{\mu_g}$
Re_{mf}	Minimum fluidization Reynolds number $\mathrm{Re}_{mf} = \frac{\rho_g d_p U_{mf}}{\mu_g}$
Re_{ms}	Minimum spouting Reynolds number $\mathrm{Re}_{ms} = \frac{\rho_g d_p U_{ms}}{\mu_g}$

$(Re_i)_{ms}$	Minimum spouting Reynolds number $\left(\mathrm{Re}_i\right)_{ms} = \dfrac{\rho_g d_p U_{ims}}{\mu_g}$
Re_{pt}	Minimum spouting Reynolds number $\mathrm{Re}_{pt} = \dfrac{\rho_g d_p U_t}{\mu_g}$
Re_z	Minimum spouting Reynolds number $\mathrm{Re}_z = \dfrac{\rho_g d_p U_z}{\mu_g}$
U	Superficial gas velocity
U^o	Superficial gas velocity at the base condition
U_i	Inlet gas velocity
U_{ims}	Minimum spouting inlet gas velocity (referred to D_i)
U_{mf}	Minimum fluidization velocity
$U_{mf}{}^o$	Minimum fluidization velocity at the base condition
U_{mff}	Minimum full fluidized velocity
U_{ms}	Minimum spouting velocity
U_t	Terminal velocity
U_z	Superficial gas velocity of auxiliary gas
u_r	Ratio of U to U_{ms}
V	Volume of the charged packed bed
V_{bottom}	Volume of the cone
V_{solid}	Volume of the solids loaded
V_{total}	Volume of the vessel
$v_{sH}(0)$	Vertical component of the solid velocity in the axis of the contactor at the base of the fountain
w_A	error of cross sectional area
w_Q	error of gas flow rate
w_U	error of superficial velocity

Greek letters

β	Regression coefficients vector
β_d	Coefficient of interface drag
β_v	Coefficient of interface drag
γ	Regression coefficients in the 'V' frame
ρ_b	Bulk particles density
ρ_g	Gas density
ρ_f	Fluid density
ρ_s	Solid density
ε	Static voidage

ε_o	Loose packed voidage
ε_{mf}	Minimum fluidization voidage
ε_{ms}	Minimum spouting voidage
φ	Internal friction angle
ϕ_s	Sphericity of particles
μ	Gas viscosity
ΔP	Bed pressure drop
ΔP_s	Bed pressure drop across the particles inside the spouted bed stable operation in spouting regime
ΔP_{ms}	Bed pressure drop across the particles inside the spouted bed at minimum spouting condition

Acronyms

CSB	Conventional Spouted Bed
CVD	Chemical Vapor Deposition
DPSD	Dimensionless Particle Size Distribution
DTSB	Draft Tube Spouted Bed
HTGR	High-Temperature Gas-cooled Reactors
MFC	Mass Flow Controller
MKS	System of units based on measuring lengths in Meters, mass in Kilograms, and time in Seconds
ORNL	Oak Ridge National Laboratory
PC	Principal component
PCA	Principal Component Analysis
PCR	Principal Component Regression
RAM	Random Access Memory
SB	Spouted Bed
SCR	Solid Circulation Rate
slpm	Standard liters per minute
TRISO	Tristructural-isotropic
UTK	University of Tennessee at Knoxville
YSZ	Yttrium Stabilized Zirconia

1. Introduction and Background

Introduction

The present research is targeted at developing improved scaling relationships for the hydrodynamics of shallow, gas-spouted beds of dense particles. This work is motivated by the need to more effectively scale up shallow spouted beds used in processes such as in the coating of nuclear fuel particles where precise control of solids and gas circulation is critically important. Since the spouted-bed literature contains very little data about such beds, this study focuses on generating new understanding that can be used to reduce the empiricism in spouted-bed design and operation.

The approach includes a set of initial screening experiments that utilize a fractional factorial design to identify the experimental parameters having the greatest impact on the observed minimum-spouting velocity. Subsequently, more detailed experiments were implemented to further refine empirical correlations among those parameters and key measures of the hydrodynamics. The experimental parameters explored at ambient temperature and pressure included column (bed) diameter, packed bed height, particle diameter, particle density, gas density and gas flow. For both preliminary screening and detailed experiments, the bed hydrodynamics were characterized in terms of minimum spouting velocity, mean and transient global pressure drop, time-averaged pressure profiles in the lower part of bed, and fountain height. The experimental objectives are presented in Section 1.1.

1.1 Objectives

The main objectives of this experimental investigation are:

- To identify the most important dimensionless parametric groups that control the hydrodynamics of shallow cylindrical spouted beds of dense particles; and
- To increase the range for which accurate scaling predictions can be made using these dimensionless groups.

Consistent with the above objectives, the relative hydrodynamic impact of experimental operating parameters (including bed height, gas flow, and gas viscosity and density) and column bed diameter are quantified in terms of empirical dimensionless scaling correlations. In addition, the scaling relationships and characteristic spouting features observed in these experiments are compared with the behavior of deep, lower-density beds reported in the literature.

1.2 Organization of Dissertation

This dissertation is organized into five major chapters. The current chapter introduces the problem of shallow spouted bed hydrodynamics and summarizes previously reported hydrodynamic studies of spouted beds. Chapter 2 describes the experimental approach used, and Chapter 3 explains the data analysis methodology. Chapter 4 summarizes the general observations, presents correlations developed among the key dimensionless groups and the measured output variables of interest, namely, minimum spouting velocity, bed pressure drop at minimum spouting condition and fountain height. The final chapter (5) summarizes the overall conclusions and identifies future research needs.

1.3 Spouted-bed applications and motivation for this study

Spouted beds are widely used for gas-solids contacting where high solids circulation is important. Typically, spouted beds have a central gas jet that entrains solids near the bottom of the bed and transports them upward through a central zone toward the top. As the upward-moving solids exit the top of the bed and separate from the gas, they fall back to the bed surface and move slowly downward in an outer annular zone toward the bottom [1]. The net effect of these two opposing solid flows is to create a toroidal-like circulation cell that defines the overall solids circulation. The interface between the upward- and downward-moving solids is not fixed but can vary in space and time. In some cases a cylindrical draft tube is inserted in the center of the bed to stabilize the interface [2,3]. This enhances the separation between the upward and downward flow zones and increases the overall circulation rate.

Industrial applications of spouted beds include combustion, coating, drying, and gasification [4-6]. There are at least four widely used spouted-bed configurations: flat-base cylindrical, cone-base cylindrical, conical and dilute jet. Bi [7] reviews many of the salient differences among these designs. The most widely used configuration is the conical-base cylindrical bed. In the majority of applications, the solids bed height in the cylindrical section is deeper than the height of the conical bottom [17].

One important recent application of shallow spouted beds is for the production of tri-structural-isotropic (TRISO) nuclear fuel particles used in high temperature gas-cooled nuclear reactors (HTGR). These fuel particles are formed by coating a kernel of uranium oxycarbide (UCO) with multiple layers of carbon and silicon carbide. The coating process is carried out via chemical vapor deposition (CVD) in high-temperature spouted beds up to 30 cm in diameter, where the solids are circulated repeatedly for several hours through zones of different temperature and gas composition to create the desired ‘onion-skin’ structure (layers). In this context, it is critical to make the circulation as uniform as possible in order to minimize particle-to-particle variations in coating thickness and quality. Such high uniformity, with low failure rates, is critical for meeting the extremely stringent nuclear fuel specifications.

1.4 Hydrodynamic scaling in spouted beds

For many types of unit operations, proper scaling consideration is critical in relating laboratory studies to full-scale production. This is also true for spouted beds, where it is desirable to conduct laboratory studies at ambient conditions that can still be relevant to commercial units operating at elevated pressure and temperature. However scaling up a process involves more than the usual laboratory studies; it requires that some parameters for the larger beds preserve the same values of the small one, which in turn imposes uncertainty on scale-up criteria. The basic groundwork for scaling in fluidized beds in general (which includes spouted beds as a subset) has been discussed in numerous previous studies, most notably in the pioneering work of Glicksman [8,9]. In spite of this work, however, scaling of spouted beds still remains a relatively undeveloped area. Table 1.1 summarizes reports about scaling studies done by different authors for fluidized beds and deep spouted beds.

Table 1.1: Scaling studies

N	Correlation	Author	Year	Observations
1	Bubbling, jetting, and interstitial flow in a fluidized bed can be made geometrically similar with those in the beds of different scales if the column structure is similar and if the conditions for geometrically similar bubble coalescence, $U - U_{mf} = \sqrt{m_a}(U^o - U^o_{mf})$, and for geometrically similar flow field around a bubble and for similar bubble splitting $(U_{mf} = \sqrt{m}_a U^o_{mf})$ are satisfied.	Horio et al. [12]	1986	For fluidized bed using Geldart Group B particles
2	The full set scaling relationships were obtained by non-dimensionalizing the equations of motion for the particles and the fluid in a fluidized bed along with their boundary conditions; $\frac{gL}{U^2}, \frac{\rho_s}{\rho_f}, \frac{\beta_d L}{\rho_s U}, \frac{L_1}{L_2}, \frac{G_s}{\rho_s U}$	Glicksman [11]	1988	For fluidized beds
3	A simplified scaling law was proposed, when the gas-to-particle drag can be represented by the Ergun equation or similar expression. This set is developed for viscous dominated and gas inertial dominated limits. $\frac{gL}{U^2}, \frac{U}{U_{mf}}, \frac{\rho_s}{\rho_f}, \frac{L_1}{L_2}, \frac{G_s}{\rho_s U_0}, \phi_s$ and DPSD	Glicksman et al. [9]	1993	For fluidized beds
4	$\frac{gd_p}{U^2}, \frac{\rho_s d_p U}{\mu_g}, \frac{\rho_g}{\rho_s}, \frac{H_0}{d_p}, \frac{D_c}{d_p}, \phi_s$, DPSD and dimensionless bed geometry.	Glicksman et. al. [10]	1994	For fluidized beds
5	φ, ε_o added to Glicksman scaling parameters	He et al. [13]	1997	For deep spouted beds
6	Glicksman scaling parameters were modified to obtain scaling parameters for a rectangular spouted vessel operated with a draft duct; $\frac{gd_p}{U^2}, \frac{\rho_s \rho_g d_p{}^3 g}{\mu_g{}^2}, \frac{\rho_g}{\rho_s}, \frac{V_{solid}}{V_{total}}, \frac{D_c}{d_p}, \phi_s, \varphi, \varepsilon_o$, DPSD and dimensionless bed geometry; these parameters were validated by using CFD model.	Shirvanian et al. [16]	2004	For rectangular spouted vessels with a draft duct
7	A method is proposed to compare and properly scale 2D–3D hydrodynamic data. This methodology, which may also be used to validate 3D–3D dynamic scaling, is based on the deterministic chaos theory and takes into account the main force balances of the system (represented by Froude and Re numbers).	Villa and Guardiola [6]	2005	For fluidized beds
8	Coefficient of restitution e_{ss} is added to Glicksman scaling parameters	Xu et al. [14]	2007	For deep spouted beds

To address scaling, it is first necessary to identify the key dimensionless groups that control the hydrodynamics. In the approach of Glicksman [10,11], Horio [12] and others, the principal dimensionless groups underlying fluidized-bed hydrodynamics are identified by non-dimensionalizing the appropriate momentum and mass-conservation equations for the gas and solids. As a result of his analysis, Glicksman [10] determined that the appropriate dimensionless groups defining the hydrodynamics of fluidized beds are $\frac{gd_p}{U^2}, \frac{\rho_s d_p U}{\mu_g}, \frac{\rho_g}{\rho_s}, \frac{H_0}{d_p}, \frac{D_c}{d_p}, \frac{L_1}{L_2}, DPSD$ and

ϕ_s . In more recent work, He et al. [13], from considering mechanical effects in the annulus zone, proposed two additional dimensionless numbers: the internal friction angle, φ, and the loose packed voidage, ε_o. They experimentally validated their predictions on the basis of measurements of maximum spoutable depth, spout diameter, fountain height, and pressure profile in the annulus as functions of static bed height.

Still more recently, Xu et al. [14] added the particle-particle coefficient of restitution (e_{ss}) to the scaling relationships of spouted beds proposed by He et al. This parameter was included based on their analysis of the kinetic energy of colliding particles in the spout and annulus regions. Their conclusions seem to be supported by Goldschmidt et al. [15], who also claimed that the flow dynamics of gas-solids systems, such as the bed expansion ratio, are sensitive to e_{ss}. Xu et al. [14] experimentally validated their predictions on the basis of measurements of fountain height, spout diameter, and voidage profiles with changing coefficients of restitution.

Considering the above, the complete list of key dimensionless groups to consider in spouted-bed scaling should include: $\frac{gd_p}{U^2}, \frac{\rho_s d_p U}{\mu_g}, \frac{\rho_g}{\rho_s}, \frac{H_0}{d_p}, \frac{D_c}{d_p}, \frac{L_1}{L_2}, DPSD, \phi_s, \varphi, \varepsilon_o$ and e_{ss}. This list of dimensionless groups is by no means exhaustive. One would also expect that geometric ratios associated with bed shape and configuration would be important for scaling, as they are needed to define the boundary conditions for the continuity and momentum equations. Finally, it should be noted that actual particles almost always have distributions of size and shape that cannot be captured in the single-value descriptors used in the above dimensionless groups. As yet, rigorous ways to include this variability aspect in dimensionless terms have not been defined.

Given the above key scaling groups, it should be theoretically possible to accurately scale from any spouted bed to any other, as long as the same values are maintained for each of the groups. In practice, however, it is virtually impossible to match all of the groups simultaneously on two different beds; thus one is typically constrained to focus on recognizing the most important groups in a particular context and matching those as much as possible. Such reduced-order scaling can still be effective as long as the local hydrodynamic features are dominated by the accessible subset of dimensionless groups. The difficulty of experimentally controlling all of the dimensionless groups simultaneously, including the local gravitational acceleration, is also why only a subset of the above dimensionless groups (or a rearrangement of a subset) is typically included in experimentally derived correlations. Once the range of conditions utilized to derive correlations is exceeded (i.e., one uses them to extrapolate), the potential accuracy of predictions can be decreased considerably. Such loss of accuracy should not be surprising since the relative importance of the missing dimensionless groups can increase considerably outside the experimental limits. Furthermore, the fact that scaling fluidized or spouted beds commonly require some fixed parameters such as materials and shape among others, justifies the lack of some unimportant dimensionless groups on the scaling and hydrodynamic predictions.

1.5 Empirical correlations for spouted beds

Many empirical correlations have been developed to relate spouted-bed hydrodynamics to operating and geometric parameters [17-31]. These are summarized in tables Table 1.2 to Table 1.4. However most of these cover a limited range of fluid and particle properties; in particular, there is very little information for shallow spouted beds and spouted beds with dense particles [32]. The need for expanded data range and correlations for shallow spouted beds is made evident by previous studies such as those by Bi [7], who found different functional relationships between minimum spouting velocity and static bed height in shallow and deep beds. Likewise, Xua et al. [33] found that the pressure fluctuations in shallow beds were quite random, while those in deeper beds showed strong periodic behavior. It has been speculated that in shallow conical beds, the inlet fluidizing gas is unable to spread out radially as much as in deep beds, thus changing the shape of the toroidal solids flow; the annulus is smaller and the wall is closer to the center of the bed [34].

Table 1.2: Literature survey of minimum spouting correlations

N.	Correlation	Author	Year	Observations
1	$U_{ms} = (d_p / D_c)(D_i / D_c)^{1/3} \sqrt{2gH(\rho_s - \rho_g)/\rho_g}$	Mathur and Gishler [41]	1955	For $D_c \leq 0.3$m $H_0/D_c \geq 1.3$ $\gamma = 85°$ d_p= 0.5-3.1mm ρ_s=1.1-2.67g/cm^3 Conical
2	$U_{ms} = k(1-\varepsilon)^{1/2}(D_i / D_c)^2 \sqrt{2gH_0(\rho_s - \rho_g)/\rho_g}$	Madonna and Lama [45]	1958	Theoretical
3	$(\mathrm{Re}_i)_{ms} = 0.051 Ar^{0.59}(H_0 / D_c)^{0.25}(D_i / D_c)^{0.1}$	Nicolaev and Golubev [7,32]	1964	D_c=12cm D_o=D_i=20-50mm H_0=90-150mm d_p=1.75-5.6mm Conical
4	$(\mathrm{Re}_i)_{ms} = 0.174 Ar^{0.5}(1 + 2\tan(\gamma/2) H_0 / D_i)^{0.25} \tan(\gamma/2)^{-1.25}$	Gorshtein and Mukhlenov [7,32]	1964	D_i H_o/D_i=1.3-8.5 H_o=30-150mm γ=12-60° D_c=5-10cm d_p=0.5-2.5mm ρ_s=0.98-2.36g/cm^3 Conical
5	$(\mathrm{Re}_i)_{ms} = 3.32 Ar^{0.33}(H_0 / D_i)\tan(\gamma/2)^{0.55}$	Mukhlenov and Gorshtein [36]	1965	D_i=2-5cm H_0=9-15cm γ: not given Conical
6	$U_{ms} = k(d_p / D_c)(D_i / D_c)^2 \sqrt{2gH_0(\rho_s - \rho_g)/\rho_g}$	Ghosh [7]	1965	Conical
7	$(\mathrm{Re}_i)_{ms} = 73 Ar^{0.14}(H_0 / D_i)^{0.9}(\rho_s / \rho_g)^{0.47}$	Goltsiker [7,32]	1967	D_i=0.41-1.23cm H_0=5-31cm γ=26-60° d_p=0.5-2.5mm ρ_s=0.8-1.63g/cm^3 Conical
8	$(\mathrm{Re}_i)_{ms} = 0.4 Ar^{0.52}(H_0 / D_i)^{1.24} \tan(\gamma/2)^{0.42}$	Tsvik et al. [7,32]	1967	H_0/D_i=1.6-8.7 H_0=10-50cm γ=20-50° D_c=4-29.4cm d_p =1.5-4mm ρ_s=1.65-1.7g/cm^3 Conical
9	$(\mathrm{Re}_i)_{ms} = 1.24\,\mathrm{Re}_t (H_0 / D_i)^{0.82} \tan(\gamma/2)^{0.92}$	Wan-Fyong et al [7,32]	1969	D_i=2.6-7.6cm H_0=7-30cm γ=10-70° D_c=11.2-20cm d_p=0.35-4mm ρ_s=0.45-1.39g/cm^3

Table 1.2: Literature survey of minimum spouting correlations (Continued)

N.	Correlation	Author	Year	Observations
10	$\mathrm{Re}_{ms} = 0.0176 Ar^{0.714} \left(H_0/D_c\right)^{1.535} \gamma^{0.714} \varepsilon_{ms}^{2.21}$	Kmiec [7,32]	1977	D_i=15-35mm H_o=50-60 cm D_c=8.8, 18cm γ=24°-60° d_p=0.875-6.17mm ρ_s=1.29-2.99g/cm^3 Conical
11	$\left(\mathrm{Re}_i\right)_{ms}^2 \left(1.75 + 150(1-\varepsilon_{ms})/(\mathrm{Re}_i)_{ms}\right) =$ $31.31 Ar \left(H_0/D_i\right)^{1.757} \left(D_i/D_c\right)^{0.029} \left(\tan(\gamma/2)\right)^{2.07} \varepsilon_{ms}^3$	Markwski and Kaminski [7,32]	1983	D_i=15-82mm H_0/D_i=1.3-8.5 H_0=30-150mm γ=24-60
12	$U_{ms} = 2D_c^{1-\exp(-7D_c^2)} \left(d_p/D_c\right)\left(D_i/D_c\right)^{1/3} \sqrt{2gH_0(\rho_s-\rho_g)/\rho_g}$	Fane and Mitchellm [28]	1984	D_c=14-110 mm H_0/D_c=1-2 γ=60° D_i/D_c=1/6 d_p=2.5-6.5mm ρ_s=1.14-1.37g/cm^3 Conical
13	$U_{ms} = k\varepsilon^{3/2} \left(d_p/D_c\right)^{1/2} \left(D_i/D_c\right)^2 \sqrt{2gH_0(\rho_s-\rho_g)/\rho_g}$	Chen and Lam [7,32]	1985	Conical
14	$U_{ms}/\sqrt{2gH_0} = 0.147 \left((\rho_p-\rho_g)/\rho_g\right)^{0.477} \left(d_p/D_c\right)^{0.61} \left(H_0/D_c\right)^{0.5087} \left(D_i/D_c\right)^{0.243}$	Choi and Meisen [34]	1992	H_0= 24-53cm D_c=24, 45cm γ=60° D_i=21-35mm d_p=2.16-2.8mm ρ_s=1.05-1.09g/cm^3 Conical
15	$\left(\mathrm{Re}_i\right)_{ms} = 0.126 Ar^{0.5} \left(1 + 2\tan(\gamma/2)\, H_0/D_i\right)^{1.68} \left(\tan(\gamma/2)\right)^{0.57}$	Olazar et al. [46]	1992	D_c=36cm D_i=3-6cm H_o=36-61cm γ=28-45° d_p=1-25mm ρ_s=0.24-3.52g/cm^3 Conical
16	$\frac{\varepsilon}{1-\varepsilon}\left(\mathrm{Re}_i\right)_{ms} = \left(\frac{H_0}{D_c}\right)^{0.38} \left(\frac{d_p}{D_c}\right)^{2.54} \left(\frac{D_i}{D_c}\right)^{0.33} \left(\frac{\rho_g(\rho_s-\rho_g)gD_c^3}{\mu^2}\right)^{0.75} \mathrm{Re}_z^{-0.54}$	Zhang et al [23]	1993	$13 \le \mathrm{Re}_a \le 72$ For spouted bed with auxiliary gas
17	$Q_{ms} = 5.92\times10^{-5} \left(d_p/(D_c\phi)\right)^{0.05} \left(D_i/D_c\right)^{-2.6} \left(2gH_0(\rho_s-\rho_g)/\rho_g\right) \left(\tan(\gamma/2)\right)^{0.06}$	Rocha et al. [7,32]	1995	H_0=5.41-28cm γ=30-60° D_c=5-8.57cm d_p=6.49mm Φ=0.857 ρ_s=1.02g/cm^3 Conical

N.	Correlation	Author	Year	Observations
18	$U_{ms} = \left(D_i^2 / D_c^2\right)\left(\mu / \rho_g d_p\right)\left[\left(\mathrm{Re}_i\right)_{ms}\right]_{cone} + \left(U_{ms}\right)_{cylinder}$ $\left[\left(\mathrm{Re}_i\right)_{ms}\right]_{cone} = 0.126 Ar^{0.5}\left(D_c/D_i\right)^{1.68}\left(\tan(\gamma/2)\right)^{-0.57}$ $\left(U_{ms}\right)_{cylinder} = \left(d_p/D_c\right)\left(D_i/D_c\right)^{0.1}\sqrt{2gH_0(H_0-H_c)(\rho_s-\rho_g)/\rho_g}$	San José et al. [17]	1996	H_0=up to 35cm γ=30-150° D_c=15cm D_b=6cm D_i=2-6cm d_p=1-8mm Φ=0.857 ρ_s=2.42g/cm^3 Conical
19	$\left(\mathrm{Re}_i\right)_{ms} = \left[0.30 - 0.27/(D_b/D_i)^2\right]\sqrt{Ar\left(D_b/D_i\right)\left[\left(D_b/D_i\right)^2 + \left(D_b/D_i\right) + 1\right]/3}$	Bi et al. [26]	1997	D_c=8.8-110cm H_0/D_c<1 γ=24-60° D_i=1.5-30cm d_p=0.88-6.17mm ρ_s=0.85-2.99g/cm^3 Conical For $\left(D_b/D_i\right)$ >1.66
20	$\left(\mathrm{Re}_i\right)_{ms} = 0.202\sqrt{Ar\left(D_b/D_i\right)\left[\left(D_b/D_i\right)^2 + \left(D_b/D_i\right) + 1\right]/3}$	Bi et al. [26]	1997	For $\left(D_b/D_i\right)$ <1.66
21	$\left(\mathrm{Re}_i\right)_{ms} = 0.023 Ar^{0.63}\left(H_0/D_c\right)^1\left(D_i/D_c\right)^{0.2}\left(\sin(\gamma/2)\right)^{0.5}$	Aravinth Murugesan [25]	1997	D_c=8-90cm γ=24-180 H_0=5-183cm H_0/D_c<1 D_i=0.95-5cm d_p=0.5-7.8mm ρ_s=0.855-2.96g/cm^3 Conical
22	$\left(\mathrm{Re}_i\right)_{ms} = 0.03 Ar^{0.63}\left(H_0/D_c\right)^{0.25}\left(D_i/D_c\right)^{0.2}\left(\sin(\gamma/2)\right)^{-0.2}$	Aravinth Murugesan [25]	1997	D_c=8-90cm γ=24-180 H_0=5-183cm H_0/D_c>1 D_i=0.95-5cm d_p=0.5-7.8mm ρ_s=0.855-2.96g/cm^3 Conical
23	$\frac{\varepsilon}{1-\varepsilon}\left(\mathrm{Re}_i\right)_{ms} = \left(\frac{H_0}{D_c}\right)^{0.38}\left(\frac{d_p}{D_c}\right)^{2.54}\left(\frac{D_i}{D_c}\right)^{0.33}\left(\frac{\rho_g(\rho_s-\rho_g)gD_c^3}{\mu^2}\right)^{0.75}\mathrm{Re}_z^{-0.6}$	Wang et al. [23]	2001	D_c=19cm γ=60 H_0=20-30cm D_i=2.1cm d_p=1.45-2.5mm ρ_p=0.836-2.4g/cm^3 $13 \le \mathrm{Re}_a \le 82$ For spouted bed with auxiliary gas

Table 1.2: Literature survey of minimum spouting correlations (Continued)

N	Correlation	Author	Year	Observations
24	$U_{ms}/U_{mf} = \left(H/H_m\right)^{(1-0.5H/H_m)}$	Bi [7]	2004	Exponent approaching 1 for small H/H_m and 0.5 for large H/H_m for $\gamma=60^o$
25	$\mathrm{Re}_{ms} = 0.0015\,Ar^{0.86}\left(\frac{H_0}{D_c}\right)^{1.59}\tan\left(\frac{\gamma}{2}\right)^{0.87}$	Zhou [32]	2005	D_c=5cm H_0/D_c=0.5-1 γ=45-75° D_i=4mm d_p=0.3-0.65mm ρ_p=6g/cm^3 Conical

Table 1.3: Literature survey of bed pressure drop correlations

No.	Correlation	Author	Year	Observations
1	$\Delta P_s/(\rho_g H_0 g) = 1/[(0.81(\tan\gamma)^{1.5}/\phi^2)(D_c d_p/D_o^2)^{0.78}(D_c/H_0)]$	Manu-rung [32]	1964	D_c=15cm γ=60° d_i = 1.3cm d_p=1-4mm H_0=34-93cm ρ_s=0.92-1.43g/cm^3 Conical
2	$-\Delta P_s/H_0\rho_b g = 7.68\left[\tan(\gamma/2)\right]^{0.2}\left(\mathrm{Re}_i\right)_{ms}^{-0.2}\left(H_0/D_i\right)^{-0.33}$	Mukhlenov and Gorshtein [36]	1965	D_i=1.03-1.29cm H_0=3-15cm d_p=0.5-2.5mm D_c= 5cm γ=12-60° ρ_s=1-2.36g/cm^3 Conical
3	$\left(-\Delta P_s/H_c\rho_b g\right)_{cone} = 1.2\left[\tan(\gamma/2)\right]^{-0.11}\left(\mathrm{Re}_i\right)_{ms}^{-0.06}\left(H_c/D_i\right)^{0.08}$	Olazar et al. [30]	1993	D_c=36cm γ=28-45° D_i=3-6cm H_0=36-61cm. d_p=1-25mm ρ_s=0.24-3.5g/cm^3 Conical
4	$-\Delta P_s = \left(-\Delta P_s\right)_{cone} + \left(-\Delta P_s\right)_{cylinder}$ $\left(-\Delta P_s/H_c\rho_b g\right)_{cone} = 1.2\left[\tan(\gamma/2)\right]^{-0.11}\left(\mathrm{Re}_i\right)_{ms}^{-0.06}\left(H_c/D_i\right)^{0.08}$ $\left(-\Delta P_s/(H_0-H_c)\rho_b g\right)_{cylinder} = 3.85\times10^{-2}\left[(H_0-H_c)/D_i\right]^{0.12}\left(D_c/D_i\right)^{0.69}$(Re	San Jose et al. [17]	1996	H_0=up to 35cm γ=30-150° D_c=15cm, D_b=6cm, D_i=2-6cm d_p=1-8mm Φ=0.857 ρ_s=2.42g/cm^3 Conical
5	$\frac{\Delta P_s}{\rho_s H_0 g} = 1.05\left[\tan\left(\frac{\gamma}{2}\right)\right]^{0.057}\mathrm{Re}_{ms}^{-0.1}\left(\frac{H_0}{D_c}\right)^{0.224}$	Zhou [32]	2008	D_c=5cm H_0/D_c=0.5-1 γ=45-75° D_i=4mm d_p=0.3-0.65mm ρ_s=6g/cm^3 Conical base

Table 1.4: Literature survey of fountain height correlations

No.	Correlation	Author	Year	Observations
1	$H_f = \frac{v_{sH}(0)^2}{2g}\frac{\rho_s}{\rho_s - \rho_g}$	Olazar et al. [30]	2004	γ=30-180º D_c=0.152m H_0=0.05-0.35m D_0=0.03-0.05m D_i=0.062m d_p=2-5mm ρ_s=2.42g/cm^3 Conical base
2	$H_f = 1.01x10^{-2}\gamma^{-0.14}\left(\frac{D_i}{D_{bc}}\right)^{-1.14}\left(\frac{d_p}{D_i}\right)^{-0.83}\left(\frac{H_0}{D_{bc}}\right)^{-0.52}u_r^{4.8}\rho_s^{-0.12}\phi^{-1.45}$	San José et al. [39]	2005	γ= 28-45º, D_c=0.36m, D_0=0.03m d_p=3.5mm ρ_s=0.07-1.03g/cm^3 Conical
3	$\frac{H_f}{H_0} = 7.15\gamma^{0.64}\left(\frac{d_p}{D_c}\right)^{0.20}\left(\frac{H_0}{D_c}\right)^{0.34}\left(\frac{U}{U_{ms}}\right)^{1.03}$	Zhou [32]	2008	D_c=5cm H_0/D_c=0.5-1 γ=45-75° D_i=4mm d_p=0.3-0.65mm ρ_s=6g/cm^3 Conical base

As noted previously, the correlations in the spouted-bed literature are dominated by deep beds of particles with densities of less than 3000 kg/m^3. The only correlations relevant to the shallow, dense category are those developed by Zhou [32]. Thus the focus of this study will be on expanding the earlier work of Zhou to include more of the key dimensionless groups and increase the range for accurate scaling predictions, especially scaling predictions involving changes in bed size, static height, particle diameter, particle density and gas density. Bed size and gas properties are included because they directly relate to scaling from small, ambient laboratory experiments to hot, production-scale beds.

2. Experimental approach and methodology

Experimental approach and methodology

2.1. Experimental setup

Figure 2.1 is a schematic of the spouted-bed research facility located in Room 428 of the Dougherty Engineering Building. The experimental setup consists of an inlet-gas humidification system, three spouted beds of different diameters, pressure transducers, five analog bandpass filters, a data-acquisition system, and an image acquisition system. Early in this study, several experiments were carried out to verify and benchmark the functionality of the different components of this experimental setup. Each component is described in detail in the rest of this section.

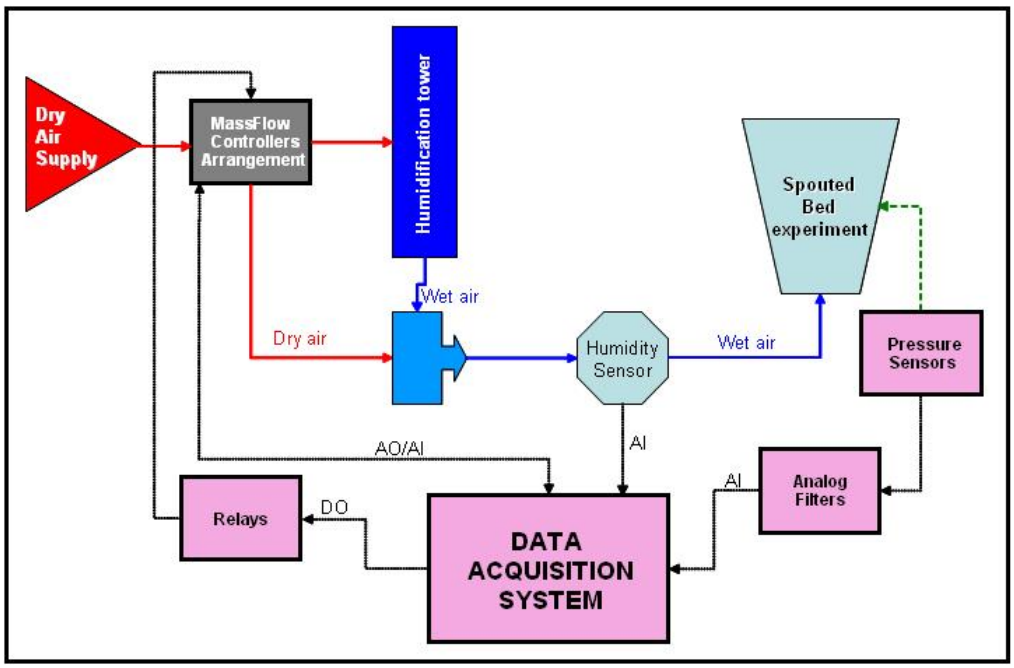

Figure 2.1: Schematic of the spouted-bed research facility.

The humidification system

In order to minimize static charge accumulation from particulate motion inside the spouted beds, the humidification system is used to maintain a nearly constant relative humidity of 40% of the fluidizing gas. The humidification system consists of a packed-bed bubbling column. A LabVIEW computer program is used to regulate the amount of humidified fluidizing gas produced by the humidification tower via five MKS mass flow controllers (MFCs) of different flow rates of 20, 50, 100, 200 and 300 slpm, ten STC on/off solenoid valves (model 2S040-3/8") and one OMEGA humidity sensor (model HX93A). The MFCs are connected in parallel to attain the desired flow rate as required by the experiments by using various combinations of MFCs. This program implements a proportional-integral type controller to continuously maintain the

required wet/dry ratio to achieve the desired relative humidity. The humidification of the fluidizing gas is achieved as follows:

1. Activate appropriate MFCs depending on the desired flow rate.
2. Gas flow from each MFC enters two on/off solenoid valves of which one is connected to the humidification tower and the other connected to a mixing junction downstream from the humidification tower.

Pressure transducers

Six pressure transducers are used to measure the pressure drops at the six pressure taps, of which two are Endevco 8510B which utilize a piezo-resistive four active arm strain gauge bridge mounted on a silicon diaphragm. The remaining four transducers are MKS Baratron differential pressure transducers that use an internal metal diaphragm. In both transducer types, the diaphragm is deflected by the fluidizing gas.

Depending on the dynamic pressure range, taps were connected to either single-sided Endevco 8510B (6894 and 34470 Pa) transducers or to MKS Baratron 223B-type differential pressure transducers with different full-scale ranges (133, 1,333 and 12,454 Pa).

Analog bandpass filters

Five bandpass analog filters are used to eliminate aliased high frequencies of the six analog differential pressure input signals. The filters used are a Rockland Model 852, a Rockland-Wavetek Model 852, a Wavetek Brickwall Model 753A, a Rockland Series 2000 and a Wavetek Model 452.

The spouted beds

Three different spouted beds with diameters of 50, 80 and 150 mm are used in the present investigation. A schematic of a typical spouted-bed setup is shown in Figure 2.2. The 50 and 80 mm diameter beds are fabricated of quartz tubes of 150 mm in length, and 60º included angle aluminum cones with a height equal to 0.86 D_c, whereas the 150 mm bed is fabricated of a glass tube of 450 mm in length, and a 60º included angle aluminum cone of 150 mm of height. . All beds have a ratio of inlet diameter to bed diameter (D_i/D_c) of 0.08. A leveler located right below the cone is used to check whether the spouted bed is plumb. At the end of each experiment the solid particles inside the spouted bed are drained to a collection vessel via a discharge valve.

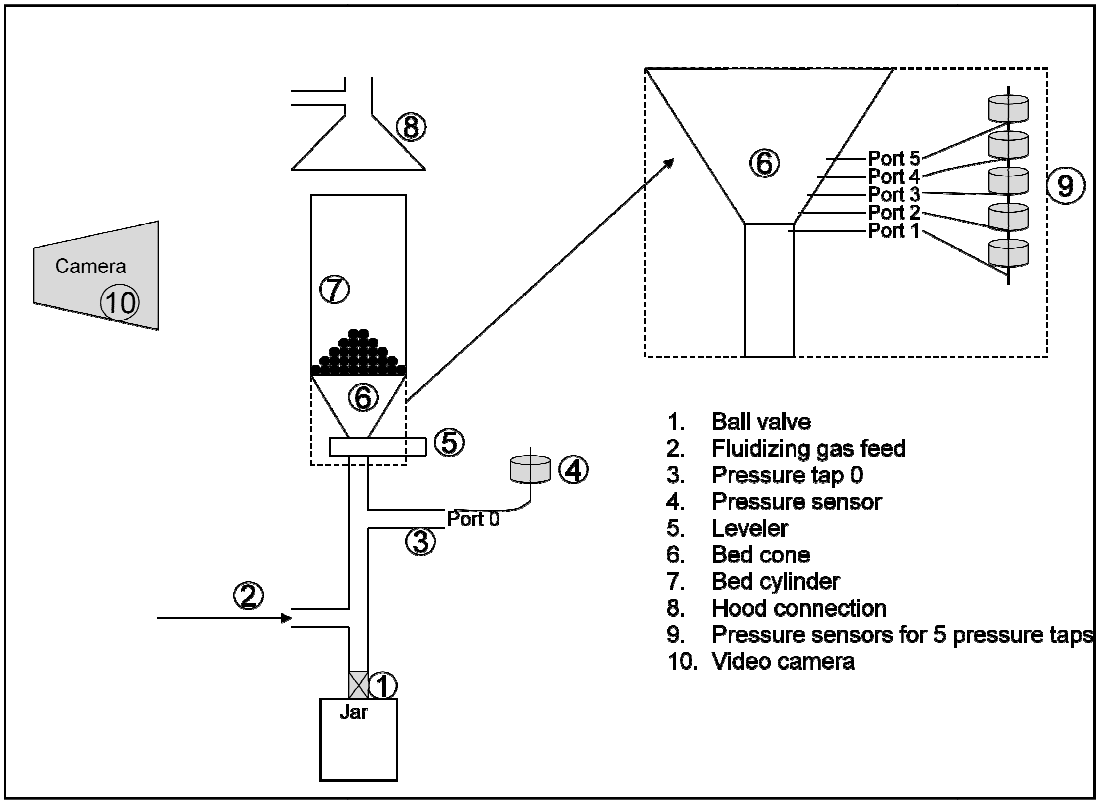

Figure 2.2: Schematic of the spouted bed

All the spouted beds have 6 pressure taps as shown in Figure 2.3 for the 50 mm bed. The taps are constructed by drilling 0.2 mm holes through the cone wall that are perpendicular to the wall. Then these holes are countersunk part way through the wall to accommodate 3.17 mm/0.125 in stainless steel tubes that provide connections for the pressure transducers. The sizing of the holes through the wall was selected to be smaller than the smallest particles so no particles would be lost from the bed. The first pressure tap, designated as 'Port 0', is located 10 diameters of the cone inlet upstream from the base of the aluminum cone and is used to measure transient global pressure drops. A pressure drop time series is averaged to obtain an average pressure drop. This configuration is the same as that used by Zhou [32] in earlier experiments conducted in our laboratory. From the average global pressure profile as the gas flow is decreased from a fully spouted condition, the minimum spouting velocity is determined. Of the remaining five pressure taps (local pressure drops), four are located on the side of the cone. For the 50mm bed these taps are placed at 2, 4, 8 and 16 mm above the inlet measured from the base of the cone for Ports 2, 3, 4 and 5, respectively, and one tap is placed 2 mm below the vertex of the cone for Port 1 as shown in Figure 2.4 and their inner diameter is around 0.2 mm. For larger beds the pressure-tap locations are scaled with respect to the diameter of the spouted bed. These ports are used to obtain non-intrusive measurements at the wall (compared with Pitot static probes) of axial pressure distributions.

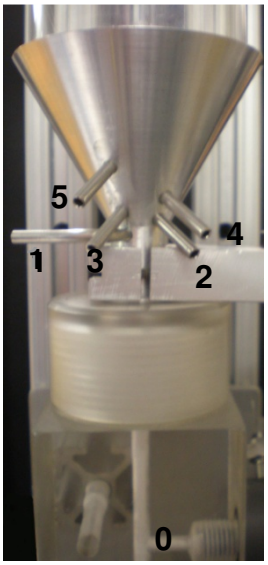

Figure 2.3: Photograph showing pressure-tap locations on the 60º cone of the 50 mm bed.

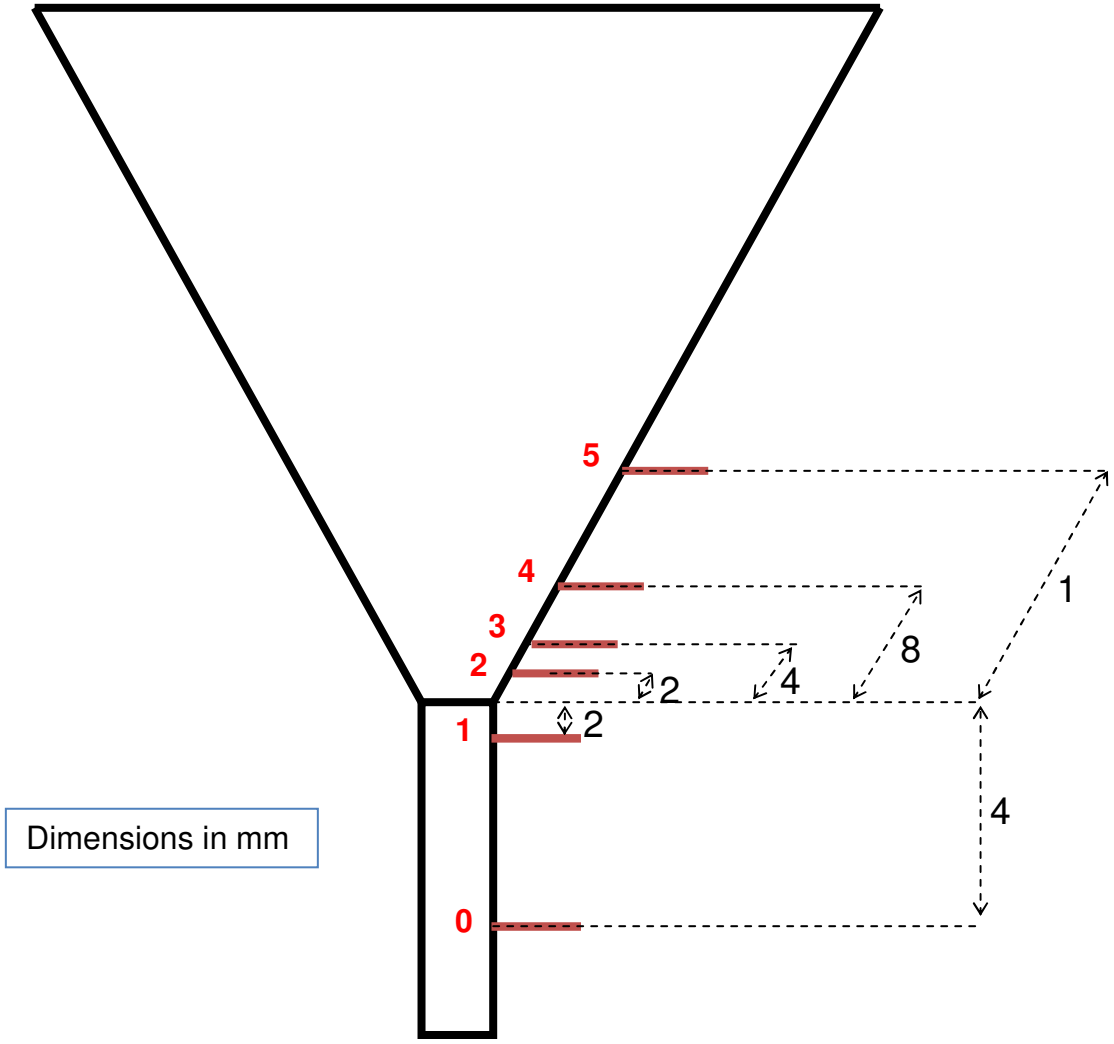

Figure 2.4: Pressure-tap locations diagram for the 60º cone of the 50 mm bed.

The minimum spouting velocity (U_{ms}) was determined by monitoring the average bed pressure drop as gas flow was reduced from a fully spouting condition to a nearly packed bed. The flow rate was incrementally decreased and then the bed was run at the new flow rate for 5 minutes to let the bed reach stationarity before the pressure time series was collected. In general the increments in flow rate were smaller in the region of U_{ms} to obtain an accurate value of Ums. Since four patterns of bed pressure drop profile were observed beyond U_{ms} (refer to Section 4.1), minimum spouting velocity was defined in two different ways:

1) For the cases where the bed pressure drop profile exhibited a discontinuity, the bed pressure drop abruptly increased as the fluidizing gas flow rate was decreased, the flow rate at the discontinuity defined Ums, the minimum spouting velocity [32]. This method was applied mostly for 500 and 1000 μm particles and is illustrated in Figure 2.5.
2) For the cases where the bed pressure drop with decreasing flow did not exhibit the anticipated discontinuity at U_{ms}, the minimum spouting velocity was defined visually as the flow where the observed fountain height was reduced to negligible levels; this method was applied mostly for 2000 μm particles.

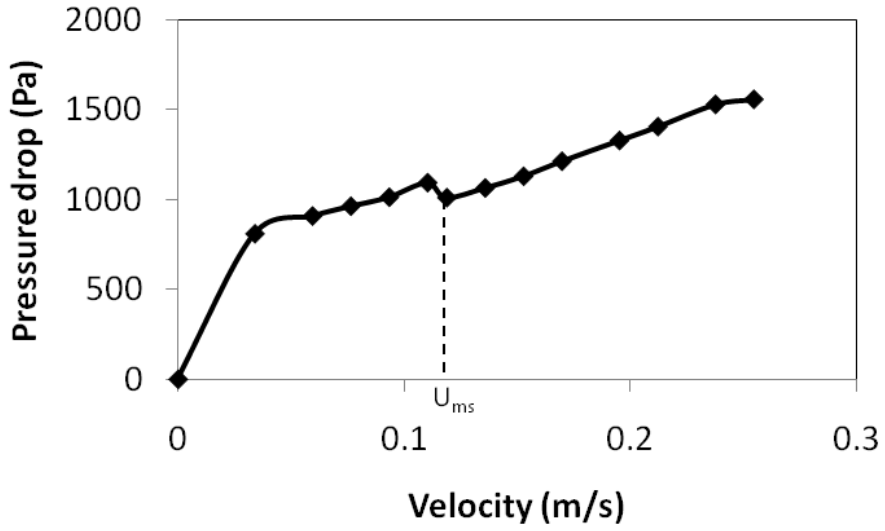

Figure 2.5: Determination of U_{ms} in the 50 mm bed for 75 g of 500 μm of YSZ particles.

In addition, axial pressure drop profiles measured on ports 1-5 were used to confirm the U_{ms} values observing the increase of pressure drop at the minimum spouting condition as the fluidizing gas flow rate was decreased. (Refer to Appendix A).

Particles

Three types of particles were used in this study: alumina (Al_2O_3), yttrium-stabilized zirconia (ZrO_2) (YSZ), and 316-alloy stainless steel (SS). Table 2.1 contains a summary of the particle properties for the three sizes employed (500, 1000, and 2000 μm) of each particle kind, including the material density and mean diameter, and fluidizing properties for the two gases used.

Table 2.1: Particle properties

Particle	ρ [kg/m^3]	d_p [μm]	U_{mf} [m/s] (1)		U_t [m/s] (2)		Geldart Group [1]
			Air	He	Air	He	
Al_2O_3	3880	500	0.35	0.40	5.41	10.18	B
		1000	0.84	1.34	9.35	20.54	D
		2000	1.47	3.18	13.86	35.53	D
YSZ	6000	500	0.51	0.60	7.11	13.81	D
		1000	1.11	1.92	11.88	27.01	D
		2000	1.87	4.22	17.17	45.14	D
SS	7600	500	0.61	0.75	8.23	16.25	D
		1000	1.29	2.32	13.49	31.24	D
		2000	2.12	4.89	19.26	51.25	D

(1) *Estimates minimum fluidizing velocity from gas and particle properties using the full Ergun [1] pressure-drop model.*
(2) *Estimates particle terminal velocity from gas using the Haider & Levenspiel [1] drag correlation.*

The Ergun [1] equation to solve for minimum fluidizing velocity (U_{mf}) is as follows:

$$\frac{1.75}{\phi_s \varepsilon_{mf}^3}\mathrm{Re}_{mf}^2 + \frac{150(1-\varepsilon_{mf})}{\phi_s^2 \varepsilon_{mf}^3}\mathrm{Re}_{mf} = \frac{d_p^3 \rho_g (\rho_s - \rho_g) g}{\mu^2} \qquad 2.1$$

Where $\mathrm{Re}_{mf} = \dfrac{\rho_g d_p U_{mf}}{\mu_g}$

And the terminal velocity (U_t) correlation is as follows:

$$U_t = \sqrt{\frac{4 d_p (\rho_s - \rho_g) g}{3 \rho_g C_D}} \qquad 2.2$$

where C_D denotes the drag coefficient computed by Haider and Levenspiel [1] which is expressed as follows:

$$C_D = \frac{24}{\mathrm{Re}_{pt}}\left[1 + \left(8.1716e^{-4.0655\phi_s}\right)\mathrm{Re}_{pt}^{0.0964+0.5565\phi_s}\right] + \frac{73.69\left(e^{-5.0748\phi_s}\right)\mathrm{Re}_{pt}}{\mathrm{Re}_{pt} + 5.378e^{6.2122\phi_s}} \qquad 2.3$$

where $\mathrm{Re}_{pt} = \frac{\rho_g d_p U_t}{\mu}$.

In the correlations for minimum fluidizing velocity and terminal velocity the particle sphericity (ϕ_s) was assumed to be 1, the gas void fraction at minimum fluidization (ε_{mf}) is assumed to be 0.42, and gas properties were evaluated at standard atmospheric conditions. Particle material densities were measured using mass from weighing particles and volume of water displace by the weighed particles. The particle size distribution was not measured and in all correlations and modeling, it is assumed to be monodisperse with small variance. The 1000 µm SS particles were sieved in the range of 18 to 16 of the A.S.T.M E-11 specification (1000-1180 µm) and the 500 µm SS were sieved in the range of 35 to 30 of the same specification (500-600 µm).

Figure 2.6 shows the Geldart chart with group designations of the particles depending on which region their parameters place them. Since the density of the particles is much greater than that of either fluidizing gas, the chart axes are basically particle diameter and density. The chart is strictly for constant cross section fluidized beds and provides a prediction of the fluidization behavior of the particles. It is commonly used as a guide for the fluidization of particles in other types of fluidized beds. This is the source of the Geldart Group classification in Table 2.1. Notice that all points fall in the D-spoutable zone except one which is in the group B next to the border of group D, this point corresponds to the 500µm particle of Al_2O_3.

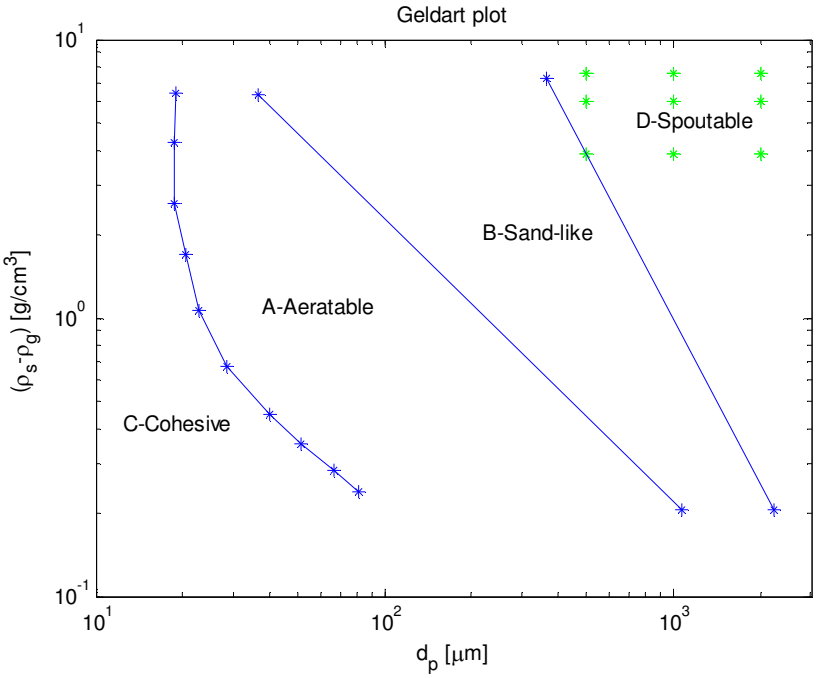

Figure 2.6: Geldart[1] plot with the points showing the Geldart group corresponding to the particles used in this investigation (Al_2O_3, YSZ and SS) in green.

Fluidizing gases

Helium and air fluidizing gases are used to simulate the effect of temperature on the hydrodynamic behavior of the spouted bed. Properties of the gases are listed below. The temperature used for the gas properties is 25 ^oC while the pressure is 1 atmosphere. . Note that for this pair of gases the viscosities are essentially the same.

Table 2.2: Gas properties

Gas	ρ_g [kg/m^3]	μ [kg/m·s]
Helium (He)	0.17	1.98×10^{-5}
Air	1.18	1.87×10^{-5}

Experiments and measurements

Experiments are performed in the 50, 80 and 150 mm-diameter spouted beds at ambient temperature and pressure with different particle densities, particle diameters, static bed heights, gas densities and gas flow rates. Table 2.1 lists the general characteristics of particles used to

perform the experiments of this investigation. At each flow condition, the following measurements are made to characterize the hydrodynamic state of the bed:

- Mean over time and transient global pressure drops at six different locations on the bed.
- Time-averaged fountain height.

The transient pressure signals at the six tap locations aforementioned are acquired with and without band-pass filtering at a sampling rate of 1000 Hertz (Hz) for duration of one minute after running at least 5 minutes to allow the bed to become stationary

From the unfiltered transient pressure signals the mean pressure drops at different locations are determined by averaging the transient pressure signals. Band-pass filtering is used to attenuate signals with frequencies less than 1 Hz to remove DC bias and greater than 100 Hz to remove higher frequency noise outside the range of dynamical interest as well as to prevent aliasing. Dynamic features of the transient pressure signals (such as Fourier power spectra) are used to characterize the time-varying component of the hydrodynamics. For example a transition in the Fourier power spectrum from a broad band to a sharp peak indicates a change from complex to nearly periodic hydrodynamic behavior.

Data acquisition system

The output of the MFCs, pressure sensors and the humidity sensor are acquired via a data acquisition system designed on a National Instruments PXI system. This system consists of the following components housed in the same PXI-1011 chassis:

- NI PXI-8186 embedded controller,
- NI PXI-6052E data acquisition card,
- NI SCXI 1123 D/A Converter module
- NI SCXI 1162 HV module for Digital Inputs (DI),
- NI SCXI 1163 module for Digital Outputs (DO),
- NI SCXI 1102B module for Analog Inputs (AI).

In addition an external NI BNC 2120 module directly connected via a 64-pin cable to the controller was used to add additional 8 AI, 2 AO and 8 DI/DO to this system. The software used in the controller to manage this system is a combination of LabVIEW v7.1 running on Windows XP, and a custom LabVIEW program, which records all the input data signals, and controls the humidity of the fluidizing gas.

Image acquisition system

The image acquisition system consists of a color MiniDV Sony camcorder model DCR-HC42 capable of capturing a maximum of 30 interlaced frames per second, each with 525 lines of resolution. The camcorder positioned in front of the spouted bed is used to record the fountain of the spouted bed at different fluidizing gas flow rates. The recordings are initially stored in MiniDV tapes and later imported into Matlab for post-processing.

The average fountain height is obtained by creating a composite image (see Figure 2.7) from a set of 30 randomly selected frames from one-minute video recordings and then using image analysis to determine the mean fountain height as illustrated in Figure 2.8. The centerline is selected manually. Black has a grayscale value of 0 and white has a value of 255. For this particular case, the sharp edge around 430 is from the top of the cone and the noisy edge around 325 is the top of the fountain at the centerline. This image analysis procedure captures the maximum fountain height in cases where the fountain height varies with time (see Section 4.1.3). A pixel corresponds to 0.22 mm which is calibrated by computing the total pixels corresponding to a section of the rule attached to the bed in the figure, this is done manually. The difference between the pixel index for top of the cone and top of the fountain in Figure 2.8 is about 100 pixels. Thus the height of the fountain above the cone from this analysis is 22 mm.

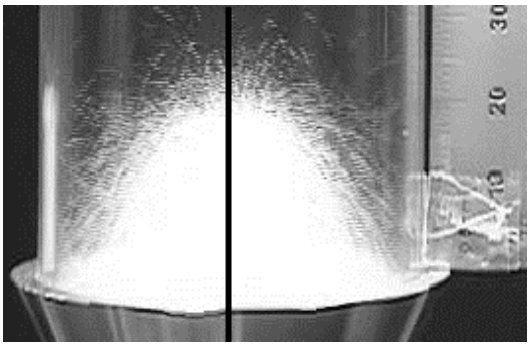

Figure 2.7: Composite image at 1.65 U/U_{ms}, with 0.67 H_0/D_c of 500 µm YSZ particles. Height above the top of the cone of the bed is about 22 mm.

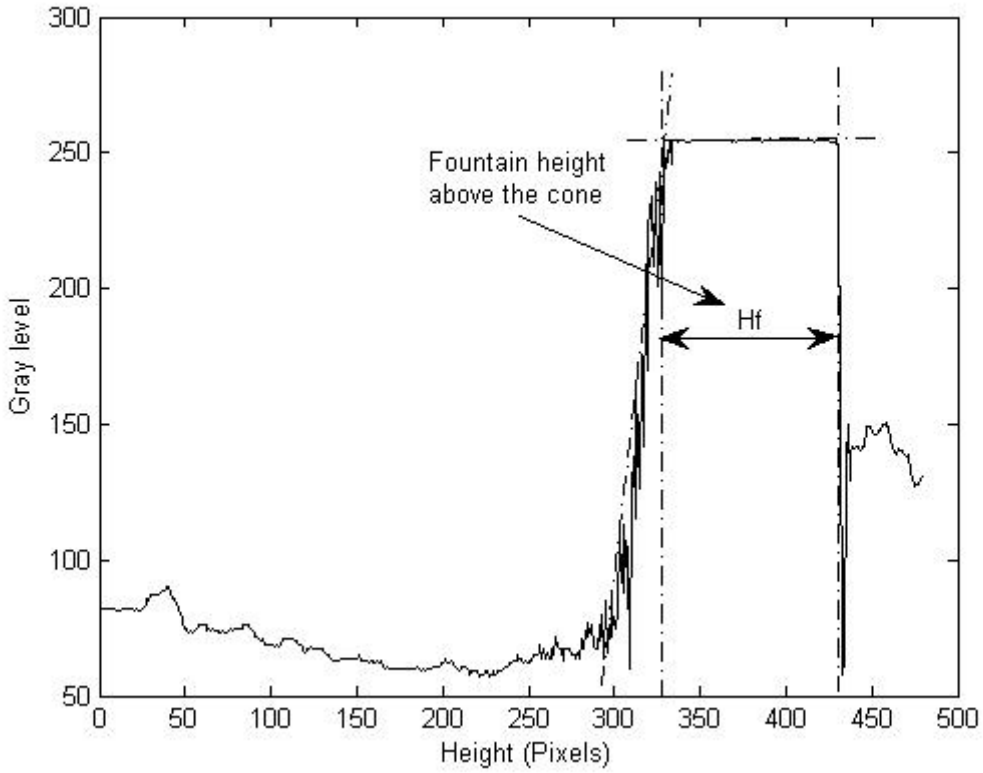

Figure 2.8: Diagram illustrating the procedure for fountain height (H_f) measurement at 1.65 U/U_{ms}, with 0.67 H_0/D_c of 500 µm YSZ particles. The vertical axis indicates the grayscale intensity determined from a pixel-by-pixel analysis along the centerline of the composite digital image. A pixel is equal to 0.22 mm.

To convert the fountain height above the cone to the total fountain height, the height above the surface of the bed to the cone edge was added to the fountain height above the surface of the bed for H_0/D_c=0.42 and 0.67. For H_0/D_c=1, the height of the bed surface above the cone edge was subtracted from the fountain height above the surface of the bed. . (Note that for a 60° inclusive bed angle and 4mm inner diameter the height of the cone is $0.86D_c$.)

In addition, for a few selected cases a distribution of centroid distances (Cd) of a fountain was generated in order to further characterize the regular and erratic spouting regimes (refer to Section 4.1), since the height and shape of the fountains for erratic spouting regimes changes over time. The centroid distance corresponds to the distance measured from the top of the cone to the centroid point of the fountain plus the cone height. The centroid distance was obtained for individual images. The centroid point (see Figure 2.9) of a fountain is obtained by computing the weighted average of every row of pixels of the grayscale version of a predefined cut slice from the cone edge to the top of the fountain along the predefined vertical center of the fountain. The weighted average uses the averaged grayscale intensity as the weight for each row of pixels of the cut slice. The cone edge is determined manually and the top of the fountain is defined by

locating the index of the row that corresponds to the freeboard whose grayscale intensity is less than a predetermined gray-white intensity value (200).

Figure 2.9: Gray scaled cut slice of a frame of the fountain generated at 1.1 U/U_{ms}, with 1 H_0/D_c of 500 µm Al_2O_3 particles in the 50 mm bed showing the centroid point of the fountain

The distribution of centroid distances over time of fountain height was generated frame by frame for 30 to 180 seconds of video time depending of the length of the video file. The process to compute the centroid distances of a fountain requires a large amount of available RAM computer memory, because every frame of the video needs to be loaded into memory to be processed one at a time. The longer the input video the more memory will be required to compute the centroid distances.

3. Experimental design and data analysis methodology

3.1.Experimental design

Using an experimental design approach, experiments were performed at ambient temperature and pressure in two Phases, designated Phase A and Phase B. Phase A, experiments were performed to explore the correlation pattern between several hydrodynamic dimensionless variables and the minimum spouting velocity (U_{ms}), to identify the parameters having the greatest impact on the minimum spouting velocity and to arrive at an empirical model for U_{ms} as a function of the design parameters grouped into dimensionless variables. In Phase B, additional experiments were performed to incorporate the biggest column diameter (150mm) and the biggest diameter particle (2000 µm) and to extend the regression model for U_{ms}. Phase A and Phase B results were used to develop empirical correlations for bed pressure drop at minimum spouting condition and fountain height by identifying the more influential parameters. Randomization, replication and blocking techniques [35] were applied to the design of experiments in order to decrease systematic errors and increase range of validity and precision. The spouted bed design parameters considered include column diameter (D_c), static bed height (H_0), particle density (ρ_s), particle diameter (d_p) and gas density (ρ_g), listed in **Table 3.1**. The temperature used for the gas properties is 25 ^oC while the pressure is 1 atmosphere. Note that viscosity is not considered as a parameter as the viscosity of the two gases at standard temperature and pressure is essentially the same.

Table 3.1: Design parameters and treatment levels for factorial designed experiments

No.	Factor	Level 1	Level 2	Level 3
1	D_c [mm]	50	80	150
2	H_0/D_c	0.42	0.67	1
3	d_p [µm]**	500	1000	2000*
4	U/U_{ms}	Minimally spouting (1.2)	Moderately Spouting (1.65)	Vigorously spouting (2.1)
5	ρ_s [kg/m^3]**	Alumina (3880)	Yttrium Stabilized Zirconia (6000)	Stainless Steel** (7600)
6	Gas ρ_g [kg/m^3] μ_g [kg/m·s]	Helium*** 0.17 1.98×10^{-5}	Air*** 1.18 1.87×10^{-5}	

** only for alumina and YSZ particles*

*** d_p and ρ_s partially used since the 2000 µm stainless steel particles were not available for any bed, and the 500 and 1000 µm stainless steel particles were only available for the 50 mm beds.*

**** Temperature=25^oC and Pressure=1 atm.*

Fifty three experiments were carried out in Phase A using the 50 and 80 mm-diameter spouted beds, based on a mixed fractional factorial design. The factors considered were three levels of packed bed height, three levels of particle density, two levels of particle diameter and two levels of gas density listed in **Table 3.2**. Results obtained from the 53 experiments were subjected to principal component analysis and regression to analyze the data to detect correlation patterns and to develop a regression model to predict the minimum spouting velocity as a function of the design parameters cast in dimensionless variables.

In Phase B, additional experiments were performed to complete mixed-level experimental design which includes a bigger diameter bed (150 mm) and a bigger particle diameter (2000 μm) as listed in **Table 3.2**. The goal is to detect correlation patterns and develop expanded regression models for minimum spouting velocity, pressure drop across the bed at the minimum spouting condition and fountain height to characterize the hydrodynamic behavior of shallow spouted beds with dense particles.

Table 3.2: Operating conditions for experiments performed in phase A and B

No.	D_c [mm]	ρ_s [kg/m^3]	H_0/D_c	d_p [µm]	Gas	U_{ms} A	U_{ms} B	ΔP_{ms}	H_f
Phase A									
1	50	3880	0.42	500	Helium	R	V	V	V
2	50	3880	0.42	500	Air	V	R	R	R
3	50	3880	0.67	500	Helium	V	V	V	V
4	50	3880	0.67	500	Air	R	V	V	V
5	50	3880	1	500	Air	R	R	X	R
6	50	6000	0.42	500	Helium	V	R	R	R
7	50	6000	0.42	500	Air	R	R	R	R
8	50	6000	0.67	500	Helium	R	V	V	V
9	50	6000	0.67	500	Air	V	V	V	V
10	50	6000	1	500	Air	R	R	R	R
11	50	7600	0.42	500	Air	R	R	R	R
12	50	7600	0.67	500	Air	R	R	R	R
13	50	7600	1	500	Helium	R	R	R	R
14	50	7600	1	500	Air	V	V	X	V
15	50	3880	0.42	1000	Helium	V	R	R	R
16	50	3880	0.42	1000	Air	R	V	V	V
17	50	3880	0.67	1000	Helium	V	V	V	V
18	50	3880	0.67	1000	Air	R	V	V	V
19	50	3880	1	1000	Helium	R	V	X	V
20	50	3880	1	1000	Air	V	V	V	V
21	50	6000	0.42	1000	Helium	R	V	V	V
22	50	6000	0.42	1000	Air	V	V	V	V
23	50	6000	0.67	1000	Helium	V	R	R	R
24	50	6000	0.67	1000	Air	R	V	V	V
25	50	6000	1	1000	Air	R	R	R	R

Table 3.2: Operating conditions for preliminary experiments (Continued)

No.	D_c [mm]	ρ_s [kg/m^3]	H_0/D_c	d_p [µm]	Gas	U_{ms} A	U_{ms} B	ΔP_{ms}	H_f
26	50	7600	0.42	1000	Air	R	V	X	V
27	50	7600	0.67	1000	Helium	R	R	X	R
28	50	7600	0.67	1000	Air	V	R	R	R
29	50	7600	1	1000	Air	R	R	X	R
30	80	3880	0.42	500	Helium	R	V	X	V
31	80	3880	0.42	500	Air	V	R	R	R
32	80	3880	0.67	500	Helium	R	R	R	R
33	80	3880	0.67	500	Air	V	R	R	R
34	80	3880	1	500	Helium	R	R	R	X
35	80	3880	1	500	Air	V	V	V	V
36	80	6000	0.42	500	Helium	V	V	X	V
37	80	6000	0.42	500	Air	R	R	R	R
38	80	6000	0.67	500	Helium	V	V	X	V
39	80	6000	0.67	500	Air	R	R	R	R
40	80	6000	1	500	Helium	V	V	V	V
41	80	6000	1	500	Air	R	R	R	R
42	80	3880	0.42	1000	Helium	V	R	R	R
43	80	3880	0.42	1000	Air	R	R	R	R
44	80	3880	0.67	1000	Helium	V	V	V	V
45	80	3880	0.67	1000	Air	R	V	V	X
46	80	3880	1	1000	Helium	V	R	R	R
47	80	3880	1	1000	Air	R	R	R	X
48	80	6000	0.42	1000	Helium	R	R	R	R
49	80	6000	0.42	1000	Air	V	V	V	V
50	80	6000	0.67	1000	Helium	R	V	X	V

Table 3.2: Operating conditions for preliminary experiments (Continued)

No.	D_c [mm]	ρ_s [kg/m^3]	H_0/D_c	d_p [µm]	Gas	U_{ms} A	U_{ms} B	ΔP_{ms}	H_f
51	80	6000	0.67	1000	Air	V	R	R	R
52	80	6000	1	1000	Helium	R	V	V	V
53	80	6000	1	1000	Air	V	V	X	V
Phase B									
54	50	3880	0.42	2000	Helium		R	X	R
55	50	3880	0.42	2000	Air		R	X	X
56	50	3880	0.67	2000	Helium		R	X	R
57	50	3880	0.67	2000	Air		V	X	V
58	50	3880	1	2000	Air		V	X	V
59	50	6000	0.42	2000	Helium		R	X	R
60	50	6000	0.42	2000	Air		R	X	R
61	50	6000	0.67	2000	Air		R	R	R
62	50	6000	1	2000	Air		R	X	R
63	80	3880	0.42	2000	Air		V	X	V
64	80	3880	0.67	2000	Helium		R	X	R
65	80	3880	0.67	2000	Air		V	X	V
66	80	3880	1	2000	Air		R	X	X
67	80	6000	0.42	2000	Air		V	X	V
68	80	6000	0.67	2000	Helium		V	X	V
69	80	6000	0.67	2000	Air		R	X	R
70	150	3880	0.42	500	Air		V	V	X
71	150	3880	0.67	500	Air		V	V	X
72	150	3880	1	500	Air		V	X	X
73	150	6000	0.42	500	Air		R	R	X
74	150	6000	0.67	500	Air		R	X	X
75	150	6000	1	500	Air		R	R	X

In the table, R denotes a reference data set for that particular phase and correlation, V denotes a verification set, and X denotes that the set was excluded. The Phase A experiments were also used in the superset of Phase B for the U_{ms} correlation, so there are two columns to denote their use in each phase.

3.2.Data analysis methodology

3.2.1 *Obtaining linear equation to correlate each response variable with respect to chosen predictor variables*

Relationships of design parameters grouped into dimensionless variables (treatment variables) accounting for the effects on each measured output variable are analyzed to detect correlation patterns and to develop a regression model for prediction.

The relationship between a measured variable $\tilde{y}$ and a set of dimensionless variables $\{\tilde{x}_1, \tilde{x}_2 ....\tilde{x}_k\}$ is expressed by the following nonlinear power equation:

$$\tilde{y} = \tilde{\beta}_0 \tilde{x}_1^{\beta_1} \tilde{x}_2^{\beta_2} ....\tilde{x}_k^{\beta_k} \qquad 3.1$$

In order to convert Equation 3.1 into a pseudo-linear form, natural logarithm of both sides are taken to result in the following equation.

$$\ln \tilde{y} = \ln \tilde{\beta}_0 + \beta_1 \ln \tilde{x}_1 + \beta_2 \ln \tilde{x}_2 + ...\beta_k \ln \tilde{x}_k \qquad 3.2$$

After redefining $\beta_0 \equiv \ln \tilde{\beta}_0$, $y \equiv \ln \tilde{y}$ and $x_i \equiv \ln \tilde{x}_i$ for i=1,…k , the Equation 3.2 becomes a linear equation, shown below, with $\beta_0, \beta_1, ...\beta_k$ as the intercept and multiple regression slopes respectively.

$$y = \beta_0 + \beta_1 x_1 + \beta_2 x_2 + ...\beta_k x_k \qquad 3.3$$

The form of Equation 3.1 is normally used in the literature to express hydrodynamic correlations of spouted beds (see Table **1.2**-Table **1.4** in Chapter 2). In Equation 3.1, the response variable, $\tilde{y}$, corresponds to a measured variable such as minimum spouting velocity, bed pressure drop and fountain height expressed in dimensionless form, and a set of the predictor variables, $\{\tilde{x}_j\}_{j=1}^{k}$, corresponds to dimensionless variables such as Ar, Re, Fr, $\frac{H_0}{D_c}$, $\frac{d_p}{D_c}$, $\frac{D_i}{D_c}$, $\frac{\rho_s}{\rho_g}$, $\frac{H_0}{d_p}$, and $\frac{U}{U_{ms}}$. Terms that involve U or U_{ms} are used commonly in the development of a model for fountain height and bed pressure drop. Each β_j can be regarded as a sensitivity coefficient between $\tilde{y}$ and the j^{th} $\tilde{x}$ variable.

The dimensionless form of the measured variables,' $\tilde{y}$ ', considered in this investigation are listed in Table 3.3.

Table 3.3: Dimensionless $\tilde{y}$ variables

No.	Response Variable	Dimensionless form
1	Minimum spouting velocity	$\frac{U_{ms}}{U_t}$
2	Bed pressure drop at minimum spouting velocity	$\frac{\Delta P_{ms}}{g\rho_s H_0}$
3	Fountain height	$\frac{H_f}{H_{f-\max}}$

Let 'n' denote the number of combinations of the treatment variables expressed in a dimensionless form. Treatment data from all n sets of experiments are to be collected into a matrix $\tilde{\chi}$, with n rows and k columns. The i[th] row represents the i[th] treatment values of the k $\tilde{x}$ variables; and each column is the n treatment values of the corresponding $\tilde{x}$ variable.

$$\tilde{\chi} = \begin{bmatrix} \tilde{x}_{11} & \tilde{x}_{12} & \cdots & \tilde{x}_{1k} \\ \tilde{x}_{21} & \tilde{x}_{22} & \cdots & \tilde{x}_{2k} \\ \vdots & \vdots & \cdots & \vdots \\ \tilde{x}_{n1} & \tilde{x}_{n2} & \cdots & \tilde{x}_{nk} \end{bmatrix} \qquad 3.4$$

Likewise, the n measurements of a response variable are collected into a column vector $\tilde{y}$. Each element $\tilde{y}_i$ represents an individual measurement of the response variable at the i[th] set of treatment values of the k $\tilde{x}$ variables.

$$\tilde{y} = \begin{bmatrix} \tilde{y}_1 \\ \tilde{y}_2 \\ \\ \tilde{y}_n \end{bmatrix} \qquad 3.5$$

Collected data, $\tilde{y}$ and $\tilde{\chi}$, are pre-treated as follows:

a) Scaling: collected data, $\tilde{y}$ and $\tilde{\chi}$, are scaled by dividing each column by the maximum value of that column: each element of the vector $\tilde{y}$, is divided by the maximum value of the vector $\tilde{y}$, $\tilde{y}_{\max}$, and each element of the j[th] column of $\tilde{\chi}$ matrix, is divided by the

maximum value of the j[th] column, $\tilde{x}_{j,\max}$. Thus, each element of the scaled data matrix is expressed as follows: $\frac{\tilde{y}_i}{\tilde{y}_{\max}}$ and $\frac{\tilde{x}_{ij}}{\tilde{x}_{j,\max}}$ for i=1..n and j=1…..k

b) The natural log of the elements of the scaled data is taken; defining the new variables y_i and x_{ij} as follows: $y_i \equiv \ln\frac{\tilde{y}_i}{\tilde{y}_{\max}}$ and $x_{ij} \equiv \ln\frac{\tilde{x}_{ij}}{\tilde{x}_{j,\max}}$

c) Centering: the mean of the *y* column, $\bar{y}$, is subtracted from each element of the *y* vector; and the mean of the x_j column, $\bar{x}_j$, is subtracted from each element of x_j, so that the mean of each column is '0'.

After mean centering, the linear equation is converted to a linear equation without intercept (β_0):

$$\Delta y = (\Delta\chi)\beta \qquad 3.6$$

where $\Delta y = \left(y - \bar{y}\right)$ and $\Delta\chi = \left(\chi - \bar{\chi}\right)$, and where the mean of the j[th] column of χ data matrix, $\bar{x}_j$, is subtracted from each element of the j[th] column of χ, x_j.

And the vector Δy, the matrix $\Delta\chi$ and β are expressed as follows:

$$\Delta y = \begin{bmatrix} \Delta y_1 \\ \Delta y_2 \\ \vdots \\ \Delta y_n \end{bmatrix} \qquad \Delta\chi = \begin{bmatrix} \Delta x_{11} & \Delta x_{12} & \dots & \Delta x_{1k} \\ \vdots & \vdots & \vdots & \vdots \\ \Delta x_{n1} & \Delta x_{n2} & \dots & \Delta x_{nk} \end{bmatrix} \qquad \beta = \begin{bmatrix} \beta_1 \\ \beta_2 \\ \vdots \\ \beta_k \end{bmatrix} \qquad 3.7$$

Defining $Y \equiv \Delta y$ and $X \equiv \Delta\chi$, Equation 3.6 becomes

$$Y = X\beta \qquad 3.8$$

3.2.2 *Principal Component Regression (PCR)*

Due to correlation among the independent dimensionless x variables, principal component model regression was carried out instead of a normal multiple-least-square regression (MLSR). PCR will also shed light on the degree of colinearity among the k x variables.

PCR method was chosen to deal with the correlated dimensionless variables as a way to take care of the multicolinearity problem. Correlation among the x variables manifests in the data matrix X, having possibly a big conditional number. If this is the case, the dimension of the data matrix X is then reduced by projecting it down to an r-dimensional subspace of the original k-dimensional space, where 'r' is deemed to be the effective rank of 'X'. Regression using reduced data results in robust regression coefficients, insensitive to perturbations in, y. The effective dimension 'r' is to be determined by first performing a singular-value-decomposition (SVD) [43] on the X data matrix. Using diagnostic tools, such as scree plots, and engineering judgment, the effective dimension 'r' is determined. A set of orthogonal vectors that spans the r-dimensional row space of X is given by the right singular vectors of X. These orthonormal vectors are referred to as the 'principal component (PC) vectors' of X. The first PC is such that it maximizes the sum of squares of the projections of the row vectors of X onto this PC; in other words, it maximizes the variance of the n data points of X when projected onto it. The second PC maximizes the residual of the data matrix after the projection onto PC1 has been subtracted from it, and on down to the next PC. The last PC has the smallest variance of the original data when projected onto it.

SVD is a matrix factorization; $X=U\Sigma V^T$, the columns of U are orthonormal and are the left singular vectors of X, the diagonal elements of Σ are all positive and are the singular values arranged in descending order, and the columns of V are orthonormal and are the right singular vectors of X. SVD of a matrix results in new basis vectors, V, to span the row space of X. V vectors represent the new orthogonal variables each of which is a linear combination of the original variables. The signs and relative values of the elements in each V vector reveal the correlation pattern among the original x variables.

Scree plots help, at a glance, to gauge the number of PC's to retain. Figure 3.1 (a) and (b) show an example of the scree and cumulative plot respectively. A scree plot depicts the relative variance contributed by each principal component. It is computed by taking the ratio of the square of each singular value with respect to the sum of the squares of all the singular values. The latter is the quantitative measure of the total variance embedded in the X data matrix. Since the PC vectors are orthogonal, projection of the original data onto each PC vector is decoupled from that onto other PC's. A cumulative scree plot shows the stepwise cumulative variance contributed by the first PC, the first two PC's,…, and by all PC's.

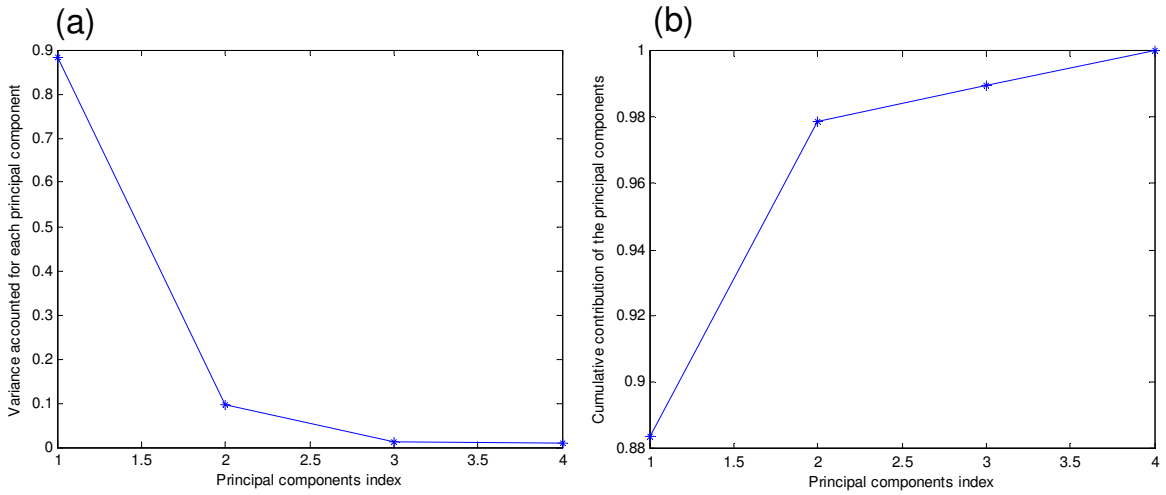

Figure 3.1: (a) Scree plot of the variance contributed by each principal component. (b) Cumulative contribution of each principal component.

The steps in performing a PCR to derive the β vector of regression coefficients for Equation 3.6 are described as follows.

a) Compute SVD of the matrix $X=U\Sigma V^T$.
b) Choose the number, '*r*', of principal components to retain, based on scree plot and engineering judgment.
c) Project X down to the reduced *r*-dimensional principal component space as X_v, $X_v=XV_r$ and compute the regression vector in the v frame $\beta_v=X_v^+Y$, where X_v^+ denotes the pseudoinverse of X_v.
d) Transform the regression coefficients in v frame back to the original space by $\beta=V_r\beta_v$ and recover the intercept: $\left(\ln\tilde{\beta}_0\right)=\bar{y}-\bar{X}\beta$, where $\bar{y}$ and $\bar{X}$ denote the mean of y and the k X columns respectively.

3.2.3 *Recovering the coefficient $\tilde{\beta}_0$ from PCR*

After the regression coefficients of a PCR model are obtained, the intercept $\tilde{\beta}_0$ can be recovered. The coefficient $\tilde{\beta}_0$ is obtained from the following pseudo linear equation derived from equation 3.1 after taking the natural log of the scaled raw data.

$$y = \ln\left[\frac{\tilde{\beta}_0\left(\tilde{x}_{1\max}^{\beta_1}\tilde{x}_{2\max}^{\beta_2}....\tilde{x}_{k\max}^{\beta_k}\right)}{\tilde{y}_{\max}}\right] + \beta_1 x_1 + \beta_2 x_2 + ...\beta_k x_k \qquad 3.9$$

where: $y_i \equiv \ln\frac{\tilde{y}_i}{\tilde{y}_{\max}}$ and $x_{ij} \equiv \ln\frac{\tilde{x}_{ij}}{\tilde{x}_{j,\max}}$ for j=1…k.

Then, developing Equation 3.9,

$$y = \ln\tilde{\beta}_0 + \ln\left(\tilde{x}_{1\max}^{\beta_1}\right) + \ln\left(\tilde{x}_{2\max}^{\beta_2}\right)....+ \ln\left(\tilde{x}_{k\max}^{\beta_k}\right) - \ln\tilde{y}_{\max} + \beta_1 x_1 + \beta_2 x_2 + ...\beta_k x_k \qquad 3.10$$

And defining a new constant 'C' to include the maximum values of columns y and x respectively, derived from the scaling procedure described in Section 3.2.1.

$$C \equiv \beta_1 \ln\left(\tilde{x}_{1\max}\right) + \beta_2 \ln\left(\tilde{x}_{2\max}\right)....+ \beta_k \ln\left(\tilde{x}_{k\max}\right) - \ln\tilde{y}_{\max} \qquad 3.11$$

Substituting constant C in Equation 3.10,

$$y = \ln\tilde{\beta}_0 + C + \beta_1 x_1 + \beta_2 x_2 + ...\beta_k x_k \qquad 3.12$$

where y denotes the vector with n log values of the scaled response variable and x_j denotes the vector with n log values of the j^{th} scaled treatment variable.

Then, Equation 3.12 is rewritten as follows:

$$y = \ln\tilde{\beta}_0 + C + \sum_{j=1}^{k}\beta_j x_j = \ln\tilde{\beta}_0 + C + \chi\beta \qquad 3.13$$

where χ is the data matrix of n rows of k treatment log scaled values.

Taking the column mean of both sides, it yields:

$$\bar{y} = \ln \tilde{\beta}_0 + C + \bar{\chi}\beta \qquad 3.14$$

where ' $\bar{y}$ ' =mean of '*y*' vector

and $\bar{X}\beta$ has the following form:

$$\bar{X}\beta = \begin{bmatrix} \bar{x}_1 & \bar{x}_2 & \dots & \bar{x}_k \end{bmatrix} \begin{bmatrix} \beta_1 \\ \beta_2 \\ \vdots \\ \beta_k \end{bmatrix} = \sum_{j=1}^{k} \beta_j \bar{x}_j \qquad 3.15$$

where ' $\bar{x}_j$ '=mean of the j[th] column of the χ data matrix.

The coefficient, $\tilde{\beta}_0$ can be recovered by rearranging Equation 3.14:

$$\ln \tilde{\beta}_0 = \bar{y} - \bar{X}\beta - C \qquad 3.16$$

and

$$\tilde{\beta}_0 = e^{\ln \tilde{\beta}_0} = e^{\bar{y} - \bar{X}\beta - C} \qquad 3.17$$

Notice that $\tilde{\beta}_0$ takes into account the constant C which includes the maximum numbers of each column x and y, derived from the scaling process (see Section 3.2.1).

3.2.4 *Data analysis*

Principal component analysis (PCA) is useful to identify patterns in data, i.e. how the variables of X data correlate with Y response variable. PCA is carried out by first concatenating 'y' the response variable to the X data matrix as a new column. This is following by taking the SVD of the augmented X matrix. Each right singular vector in V of the SVD of X reveals the make-up of the singular vector with respect to the original variables, thus showing the correlation pattern of the original variables. One looks for the singular vector which is weighted relatively heavily with the original response variable and some of the original X variables. The relative weighting shows the correlation pattern between the response variable and the corresponding original treatment variables. If the matrix is rank-deficient, then the last right singular vector in V also shows the correlation pattern among the original variables of the augmented X matrix, to further reinforce the correlation pattern observed from the first few strong V vectors.

4. Results

4.1. General observations

4.1.1 *General description of bed behavior and dynamic*

Typically, spouted beds have a central gas jet that entrains solids near the bottom of the bed and transports them upward through a central zone toward the top. As the upward-moving solids exit the top of the bed and separate from the gas, they fall back to the bed surface and move slowly downward in an outer annular zone toward the bottom [1]. Hydrodynamics of a spouted bed has been characterized by means of hydrodynamic correlations to determine minimum spouting velocity, pressure drop across the bed, fountain height, bed voidage, spout diameter, etc. The effect of several operating conditions such as gas velocity, inlet diameter, bed height, cone angle, and particle properties among others has been studied and used to correlate such hydrodynamic correlations mainly for deep spouted beds ($H_0/D_c \geq 1$) and light-density particles ($\rho_s < 3000$ kg/m^3). In this study three hydrodynamic indicators are measured; minimum spouting velocity, pressure drop across the bed and fountain height. The operating conditions varied in this study are column diameter (D_c=50, 80 and 150 mm), static bed height (H_0/D_c=0.42, 0.67 and 1), particle density (3800, 6000 and 7600 kg/m^3), particle diameter (500, 1000 and 2000 µm) and fluidizing gas (air and helium). The literature is replete with studies of these effects for deep beds of lighter particles, with only one significant study [32] focusing on shallow beds of denser particles. This study focuses on the behavior of shallow spouted beds ($H_0/D_c \leq 1$) fluidizing high-density particles.

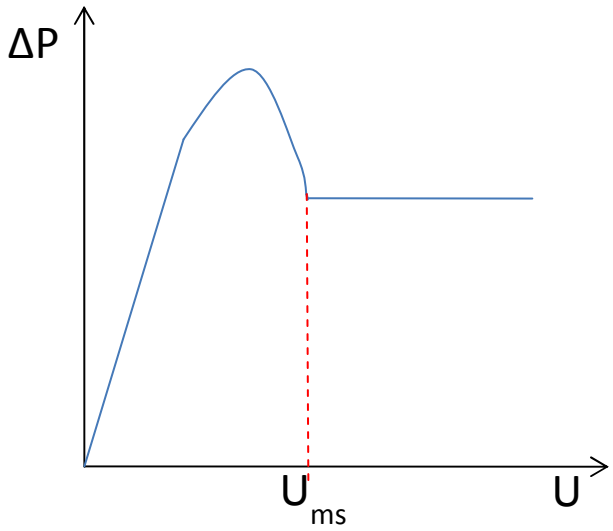

Figure 4.1: Typical pressure drop across the bed behavior of a spouted bed with respect to gas velocity [21]

In general, the minimum spouting velocity (U_{ms}) is defined as the minimum fluid velocity required to sustain spouting while decreasing or increasing gas velocity [21]. In this investigation

U_{ms} was measured by *decreasing* the gas velocity from a highly fluidized state. The gas velocity was initially set at approximately 2 U_{ms}. At each flow rate the bed was run for at least five minutes to allow the bed to reach stationary before collecting data to calculate the average pressure. Classically the typical bed pressure drop profile with increasing gas flow rate shows the bed pressure drop increase up to a maximum point, then it decreases until U_{ms} is reached and finally remains nearly constant at still higher flow rates (see Figure 4.1). A key feature is the discontinuity at U_{ms}. In this investigation four different patterns of bed pressure drop profile behavior were observed and are reported later.

Often the fountain has a regular shape and size. One characteristic of the fountain is its height which is commonly measured as the distance above of the surface of the bed. The mean fountain height is directly related to gas velocity which affects the distribution of the particles in the fountain modifying the global circulation of the particles throughout the bed.

In the present research, atypical behavior was observed in the bed pressure drop profile with fluidizing gas flow rate at values of $U/U_{ms}>1$ and in the spouting fountain height at fixed flow rates. We have not seen these phenomena presented in the literature. These phenomena are discussed by classifying the bed pressure drop profiles into four patterns and classifying the spouting behavior based on the dynamics of fountain height into three spouting regimes. Relationship between spouting regimes and bed pressure drop patterns beyond $U/U_{ms}=1$ is unclear.

4.1.2 *Bed pressure drop profiles with fluidizing gas flow*

The bed pressure drop profile behavior for several cases differed from the idealized description represented in Figure 4.1 for values of U from U_{ms} and higher velocities. These cases are classified in this work into three additional patterns.

Four patterns of bed pressure drop profile behavior that were observed at values of $U/U_{ms}>1$ are classified as listed in **Table 4.1**.

Table 4.1: Classification of bed pressure drop profile behavior after U_{ms} is reached.

Num.	Classification of ΔP bed profile	Presented mostly(1) for:
1	Constant or slight positive slope	Small particles (500 µm)
2	Decreasing (slope is negative)	Medium particles (1000 µm)
3	Decreasing and negative	Largest particles (2000 µm)
4	Bisectionally constant	Small particles (500 µm) First section: $U_{ms} \leq U \leq 2U_{ms}$ Second section: $U>2U_{ms}$

(1) Refer to Appendix B to see the classification of bed pressure drop profiles for all the experiments performed in this investigation.

The first pattern of bed pressure drop profile is the classically reported pattern presented in Figure 4.1. Figure 4.2 presents data from two cases in this research where bed pressure drop remains nearly constant within $1 \leq U/U_{ms} \leq 2.2$ with either air or helium as the fluidizing gas. Bed pressure drop remains constant mainly for the cases where 500 μm particles were fluidized. When fluidizing small particles, the velocities in the range of 1–2 U/U_{ms} are low enough that the wall drag penetrates the bed so the particles behave more like a Newtonian fluid, where the viscous forces are more important and make the fluidized particles act more like water.

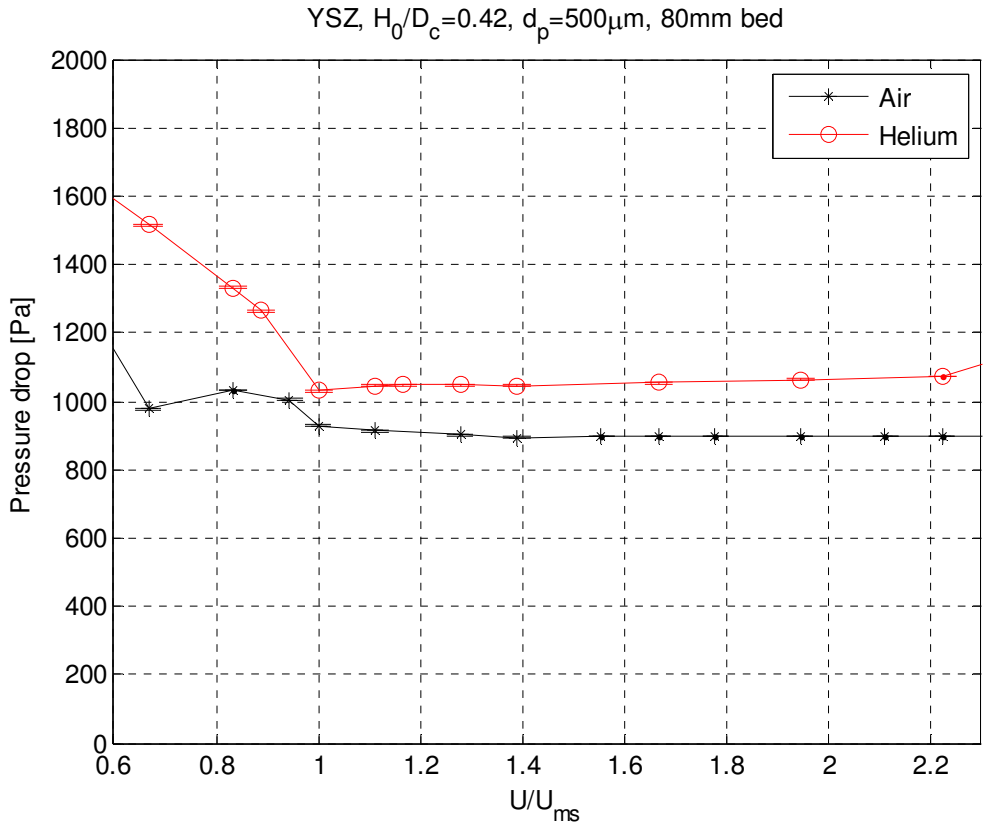

Figure 4.2: Constant profile with a discontinuity at U_{ms}: Average inlet pressure drop in the 80 mm bed as a function of U/U_{ms} for 500 μm YSZ particles at H_0/D_c=0.42 using air (U_{ms} = 0.06 m/s) and helium (U_{ms}= 0.12 m/s) as the fluidizations gases.

The second pattern of bed pressure drop profile is illustrated in Figure 4.3 showing how bed pressure drop decreases with increasing values of U/U_{ms} beyond 1; this behavior was normally found for beds with 1000 μm particles. Note the discontinuity or change in slope at U/U_{ms}=1 is present. A possible explanation for this negative slope is given in the discussion of the third pattern.

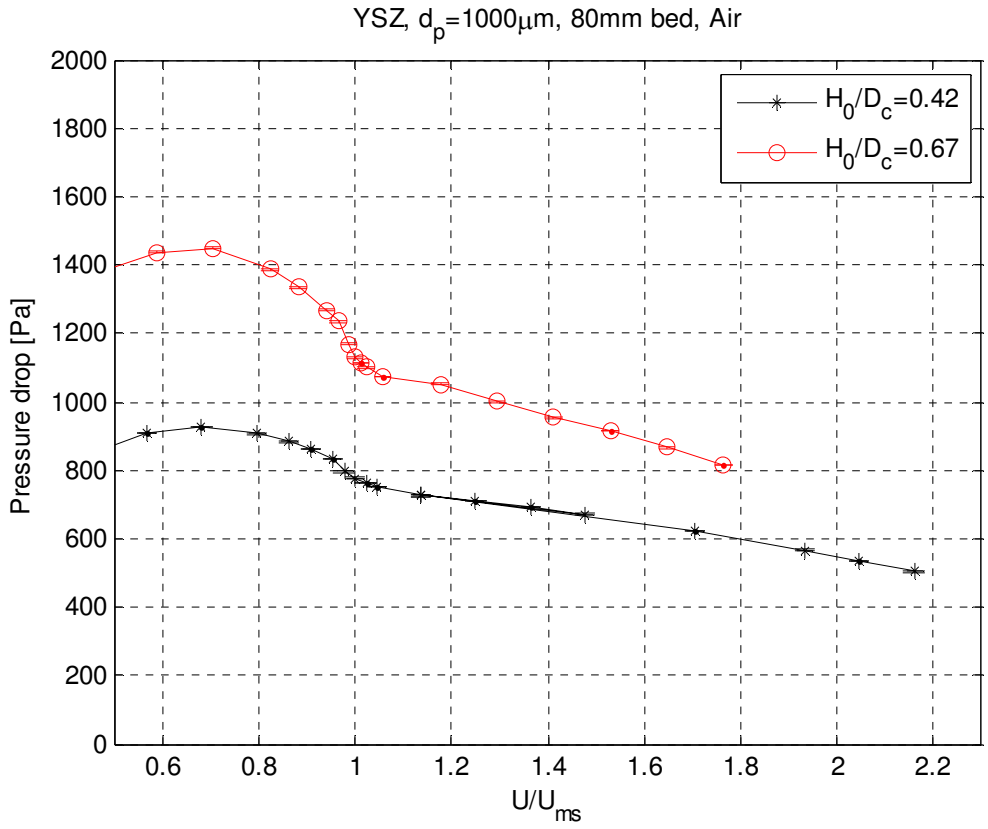

Figure 4.3: Decreasing profile with a discontinuity at U_{ms}: Average inlet pressure drop in the 80 mm bed as a function of U/U_{ms} for 1000 μm YSZ particles at H_0/D_c=0.42 (U_{ms}=0.20 m/s) and 0.67 (U_{ms}=0.34 m/s) using air as the fluidizations gas.

The third pattern of bed pressure drop profile is illustrated in Figure 4.4 showing how bed pressure drop decreases at values beyond U/U_{ms}=1 and reaches negative values of pressure drop. A discontinuity is no longer discernable at U_{ms}. This necessitated using visual observation to identify U_{ms}. This behavior was normally found for beds with 2000 μm particles. The negative values of bed pressure drop when the bed contains larger diameter particles may be due to the venturi effect as the fluidizing gas expands from the inlet tube into the conical section near the local pressure ports. This suction effect has not been reported in the spouted-bed literature and is a novel finding of this study. The venturi effect is likely the reason the pressure profile in Figure 4.3 has a negative slope but it has not overwhelmed the discontinuity. Different ways to identify U_{ms} to avoid having to use image analysis (or visual observation) should be developed.

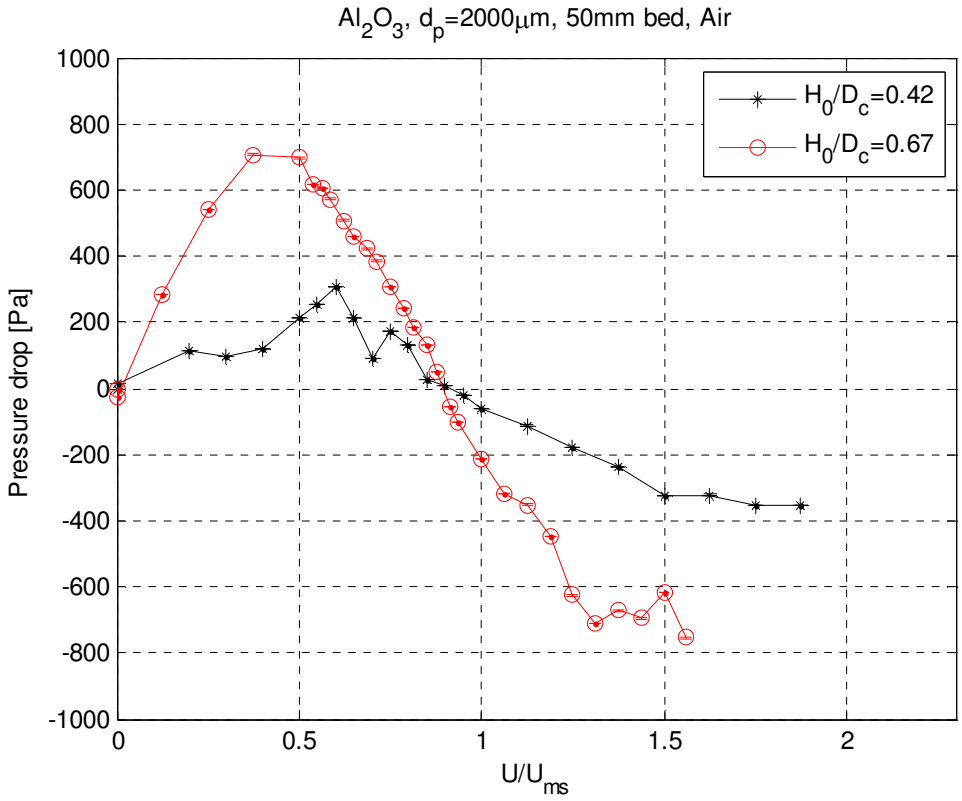

Figure 4.4: Negative pressure trend with no discontinuity at U_{ms}: Average inlet pressure drop in the 50 mm bed as a function of U/U_{ms} for 2000 µm Al_2O_3 particles at H_0/D_c=0.42 (U_{ms}=0.34 m/s) and 0.67(U_{ms}=0.68 m/s) using air as the fluidizations gas.

The fourth pattern of bed pressure drop profile is illustrated in Figure 4.5. It is observed that there are two regions where the pressure drop remains relatively constant at values beyond U/U_{ms}=1; the first region occurs in the range of $1<U/U_{ms}<2$, and the second region occurs for $U/U_{ms}>2$. This phenomenon was observed in most of the cases that were run at $U/U_{ms}>2$. It appears that the bed dynamics become more complex, with large, erratic fluctuations, commonly presenting a peak or a fountain top with lateral oscillations about the bed central axis. Video files showing this effect are attached to this dissertation (Files 1 and 2, 150-Air-Al2O3-H42-500-f2.6.avi and 150-Air-Al2O3-H42-500-f1.6.avi) displaying the behavior of the same case at $2.6U_{ms}$ and $1.6U_{ms}$. Notice that average bed pressure drop in the second region remains nearly constant despite the complex or erratic spouting behavior, which is also observed when fluidizing 500 µm particles in the 150 mm bed. The parameter matrix for this investigation was $U/U_{ms} < 2$ so only a small number of cases had data for $U/U_{ms} > 2$.

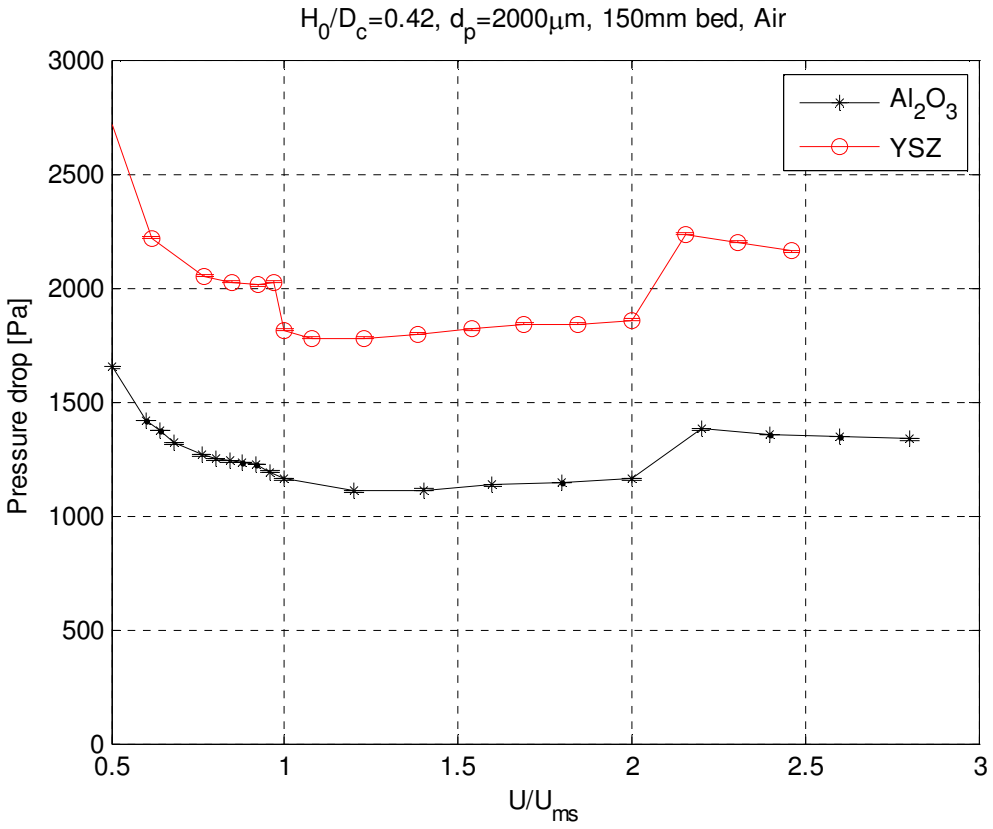

Figure 4.5: Bisectionally constant trend with discontinuity at U_{ms}: Average inlet pressure drop in the 150 mm bed as a function of U/U_{ms} for 500 μm Al_2O_3 (U_{ms}=0.05 m/s) and YSZ (U_{ms}=0.06 m/s) particles at H_0/D_c=0.42 using air as the fluidizations gas.

The aforementioned pressure-drop patterns address the need to look for better ways to measure pressure drop in shallow spouted beds at high gas flow rates that are needed when larger particles are fluidized. There is apparently a substantial radial pressure profile [32]. This is left to future investigations.

In addition of pressure drop patterns already classified beyond U/U_{ms}=1, three fountain height dynamics were observed in this investigation and are presented in the following section. Relationship between pressure drop patterns and fountain height dynamics is still unclear.

4.1.3 *Spouting regimes defined by fountain height dynamics*

The literature description of the fountain in a regular spouted bed is illustrated in Figure 4.6. The fountain is generated as the upward-moving fluidizing gas transports solids through the spout. The particles exit the top of the spout and separate from the gas. The disengaged particles then fall back around the fountain to the bed surface and move slowly downward in the outer annular zone toward the bottom of the cone where they are again entrained by the entering fluidizing gas and reenter the spout [1]. In this work additional regimes of spouting behavior that are more complex than 'regular' spouting are reported.

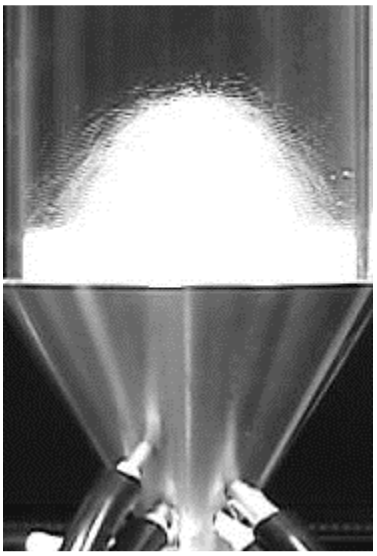

Figure 4.6: Typical fountain of a spouted bed.

Three dominant spouting regimes were defined based on visual observation of fountain height dynamics and are summarized in Table 4.2. Notice that, the already defined pressure drop patterns do not have any apparent relationship with the spouting regimes defined in this investigation.

Table 4.2: Classification of spouting regimes based on fountain height dynamics.

Num.	Classification	H_f	Common cases[(1)] that exhibit this behavior
1	Regular spouting	Constant	H_0/D_c=0.42-0.67 except 150 mm bed, more often when fluidizing with air
2	Erratic spouting	Not constant	Mostly Al_2O_3 500 µm particles, mainly at H_0/D_c=1 and, more frequently observed when fluidizing with helium.
3	Bimodal spouting	Not constant	2000 µm particles at H_0/D_c=0.42

(1) Refer to Appendix B to see the classification of spouting regimes for all the experiments performed in this investigation.

In this work shallow regular spouted beds, the first regime classification, correspond to the cases where the fountain size and shape was fairly stable at any gas flow rate from U_{ms} to $2U_{ms}$. Thus the fountain height was nearly constant with time. Cases that fall into the regular spouting regime include:

- 1000-2000 µm particles at H_0/D_c=0.67-1 in the 50 mm bed
- 1000-2000 µm particles at H_0/D_c=0.42-1 in the 80 mm bed
- 500 µm particles at H_0/D_c=0.42-0.67 in the 50 mm bed.

Fountain height is more constant over time when using air, whose density is roughly 7 times that of helium, as fluidizing gas. Figure 4.7 shows composite images at different gas flow rates for a typical regular shallow spouted bed. It is seen that the fountain height decreases as expected with decreasing gas flow rate.

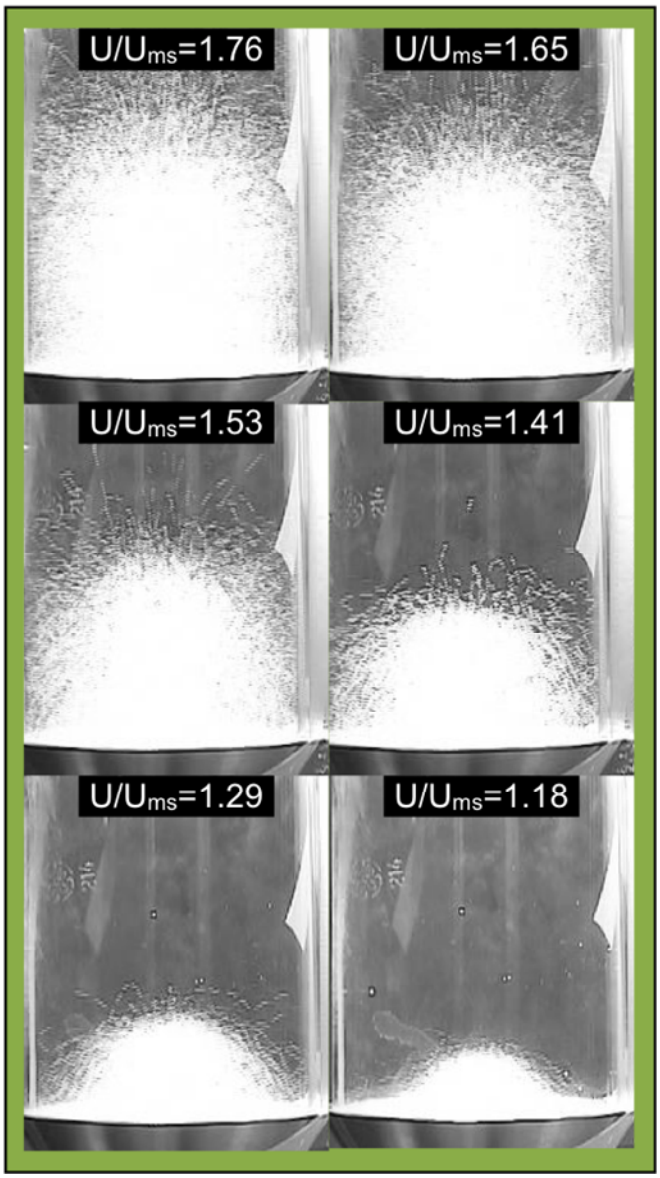

Figure 4.7: Composite images at different gas flow rates for a typical regular case, 80 mm bed for 1000 μm YSZ (U_{ms}=0.28 m/s) particles at H_0/D_c=0.67 using air as the fluidizations gas.

A second regime is termed shallow erratic spouted beds. This regime corresponds to the cases where the fountain height was not constant (varied with time): the bulk density of particles within the fountain varies according to the different fountain shapes over time, making prediction of fountain height difficult. Figure 4.8 shows the composite images at different gas flow rates for a typical erratic shallow spouted bed. Recall that these composite images are composed of 30 different randomly selected images taken from a 30-60 second digital video. Five of the six images contain 'shadows' showing that the fountain height is varying with time. The shadows

indicate that there are preferential fountain heights. For example, in the composite image at a gas flow rate of 1.19 U/U_{ms}, the superposition of at least two fountain sizes is observed. This is addressed further below by looking at the distribution of centroid distances of fountain measured from individual images.

The variability of the fountain height with time is further emphasized by the replicates of composite images at the two flow rates of U/U_{ms} = 1.29 and 1.1. These replicates were derived from the same digital video segment by making composites of 30 different randomly selected images. These replicate pairs look very different and obviously have different average fountain height. The maximum height, however, is close to the same.

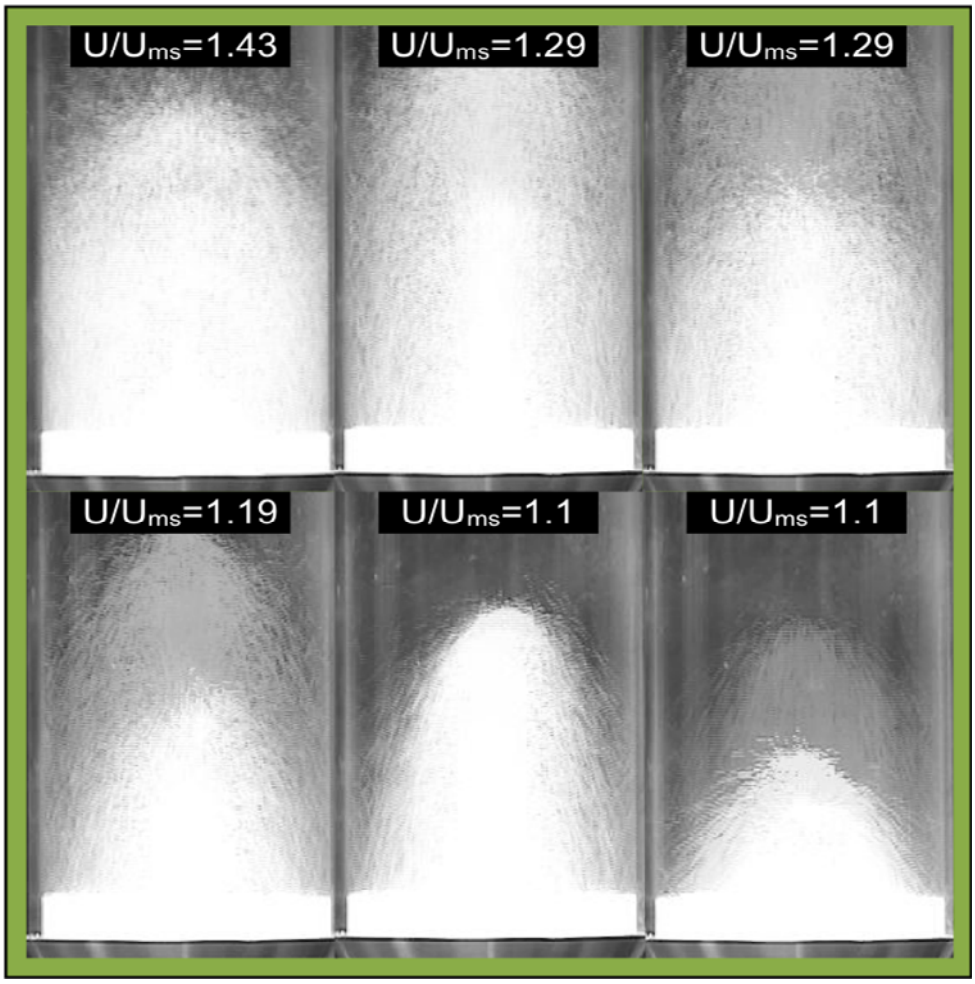

Figure 4.8: Composite images at different gas flow rates for a typical erratic case, 50 mm bed for 500 μm Al_2O_3 (U_{ms}=0.18 m/s) particles at H_0/D_c=1 using air as the fluidizations gas.

It is important to note that many replicates for several cases were constructed to validate the procedure for measuring H_f and all replicates for 'regular spouting' looked the same. Similar to the regular spouting regime case, the average fountain height for the erratic regime case decreases with decreasing gas flow rate. This correlation is not as clear as in that shown in Figure 4.7 for regular spouting. Looking at maximum fountain height, the decrease in maximum height with decreasing flow is clearer.

Erratic behavior of spouted bed fountain height was present when fluidizing the following:

- Al_2O_3 500 μm particles at $H_0/D_c=1$ in the 50 and 80 mm bed.
- At any static height ($H_0/D_c<1$) in the 150 mm bed with either Al_2O_3 or YSZ 500 μm particles. The behavior was even more erratic when fluidizing with helium.
- However, only the cases at $H_0/D_c=1$ are finally designated as erratic, since using the maximum fountain height for the cases where $H_0/D_c<1$ fit well with the final H_f correlation. The cases at $H_0/D_c=1$ were considerably more variable and degraded the correlation.

A possible explanation for this regime, when fountain size and form are very variable, is that the fluidizing gas is not penetrating the annulus area easily, meaning that the annulus area is not well aerated and particles tend to stagnate which provokes temporary irregular particle circulation in that area. The lack of uniform circulation in the annulus area can be due to the following reasons:

a) There is a high amount of particles packing towards the walls that makes void fraction low. This can explain common erratic behavior of 500 μm at $H_0/D_c=1$ and 500 μm at any static height for the 150 mm bed.
b) Low drag force of the fluidizing gas. This can explain the tendency of erratic behavior of the cases when fluidizing with helium.
c) Low inertial forces of particles due to the low particle density which allows the gas to flow through the annulus through different pathways making the particle circulation nonuniform. This effect can explain the erratic behavior of 500 μm Al_2O_3 particles at $H_0/D_c=1$ when fluidizing with air.

Erratic spouting cases were identified by visual observations. In order to further characterize the regular and erratic spouting regimes a distribution of centroid distances was generated for selected cases (see Figure 4.9). The centroid distance corresponds to the distance measured from the top of the cone to the centroid point of the fountain adding the cone height (refer to Section 2).

Distributions of centroid distances for typical erratic and regular spouting cases are shown in Figure 4.9 to illustrate the variability of the fountain height over time. Notice the much narrower span in the x-axis (centroid distance) for regular spouting. The height variation in the regular regime case is less than 2 mm out of an average distance of about 18 mm while it varies by 35 mm out of an average distance of roughly 30 mm in the erratic regime. Besides the broad spectrum, the erratic case exhibits two peaks showing the fountain tendency to spout at two

different heights. In this case one height is about twice the other height. This would be the kind of distribution expected from the case shown in Figure 4.7 with 1.19 $U/U_{ms.}$ In addition, Figure 4.10 shows the standard deviation of the centroid distance at different gas flow rates for typical regular and erratic spouting cases. Notice that as expected the standard deviation curves for regular spouting cases are much lower than those for erratic cases.

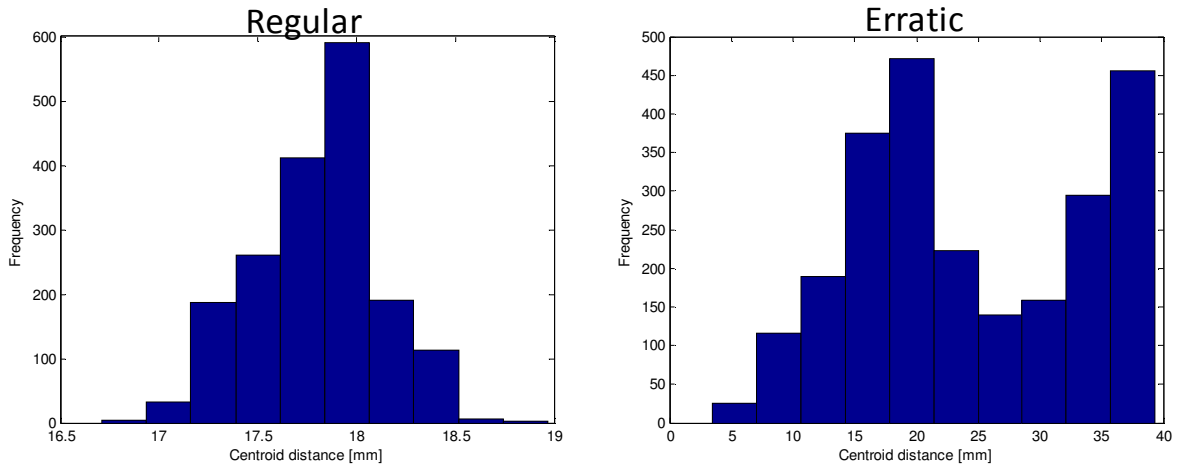

Figure 4.9: Distribution of centroid distance of fountain height for typical regular (Case 10 at $1.4U_{ms}$) and erratic (Case 5 at $1.2U_{ms}$) spouting cases.

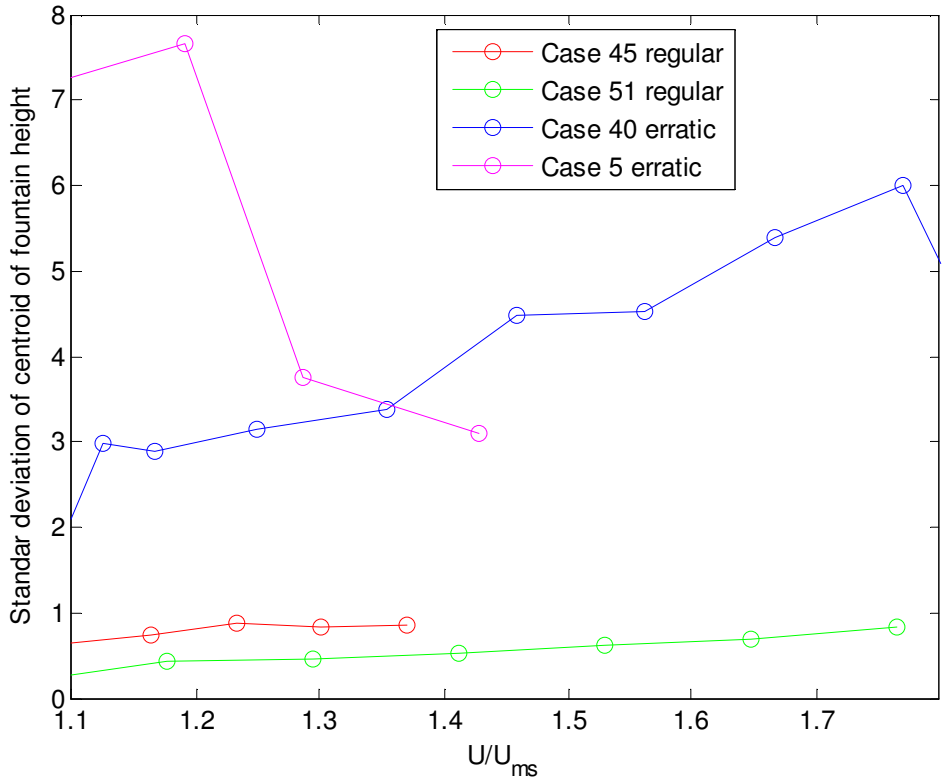

Figure 4.10: Standard deviation of centroid distance of fountain height for typical regular and erratic spouting cases. Note that the cases are defined in Table 3.2 in Section 3.1.

In addition, the coefficient of variation (CV) was determined by the ratio between the standard deviation of the centroid distance (Cd) and the mean of centroid distance (See Equation 4.1).

$$CV = \left[\frac{\sigma_{cd}}{mean(Cd)} \right] \qquad 4.1$$

where Cd denotes centroid distance (refer to Section 2).

The coefficients of variation are lower than 0.01 for regular spouting cases and between 0.02 and 0.1 for erratic cases (see Figure 4.11).

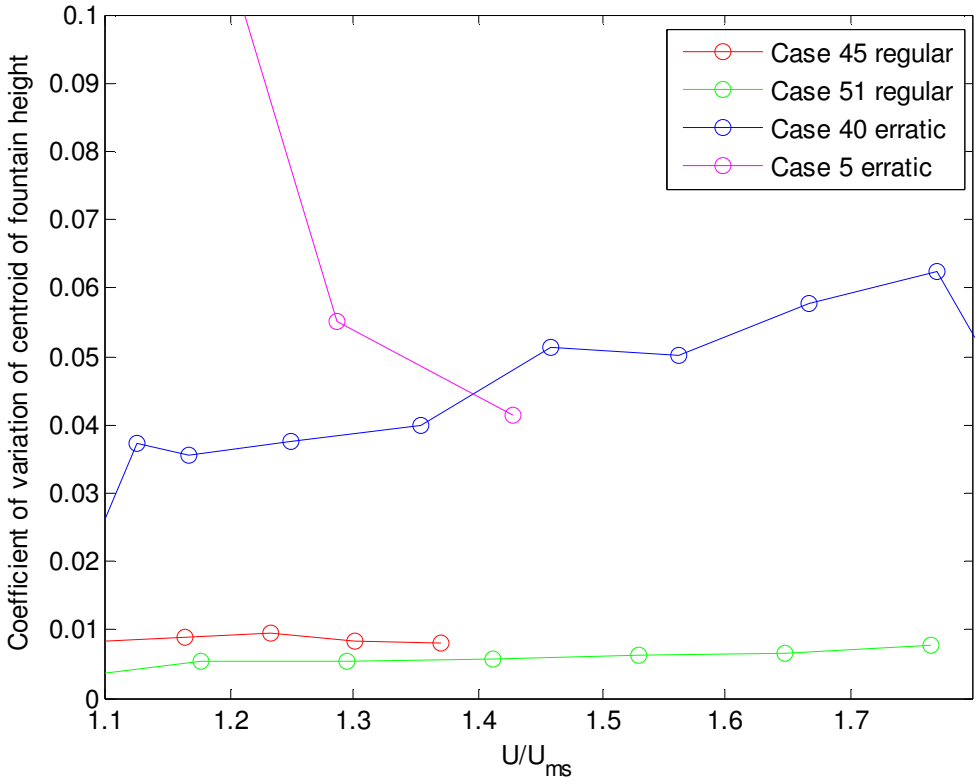

Figure 4.11: Coefficient of variation of centroid distance of fountain height with respect to gas flow rate for typical regular and erratic spouting cases. Note that the cases are defined in Table 3.2 in Section 3.1.

Another way to determine the variability of fountain height is shown in Figure 4.12, which presents the coefficient of variation of the average inlet differential pressure (equal to the average bed pressure drop) with respect to gas flow rate for erratic and regular spouting beds. The procedure to obtain centroid distances of fountain height is restricted because of the limited video records especially for very shallow spouted beds (H_0/D_c=0.42), in addition, this procedure is very computationally intensive as analysis of an image is needed to obtain each measurement.

Therefore using pressure measurements as a surrogate for fountain height in classifying the spouting regime is very attractive since pressure data is available for all operating conditions and does not involve image analysis. The statistics of the bed pressure drop time series for a subset of cases were calculated. The coefficients of variation of bed pressure drop are lower than 0.1 for regular spouting cases and are between 0.1 and 1 for erratic cases. Notice the order of magnitude difference between coefficients of variation of centroid distance and those for bed pressure drop. Therefore a criteria to define erratic cases could be a CV of bed pressure drop greater than 0.1 or a CV of centroid distance of fountain height greater than 0.01.

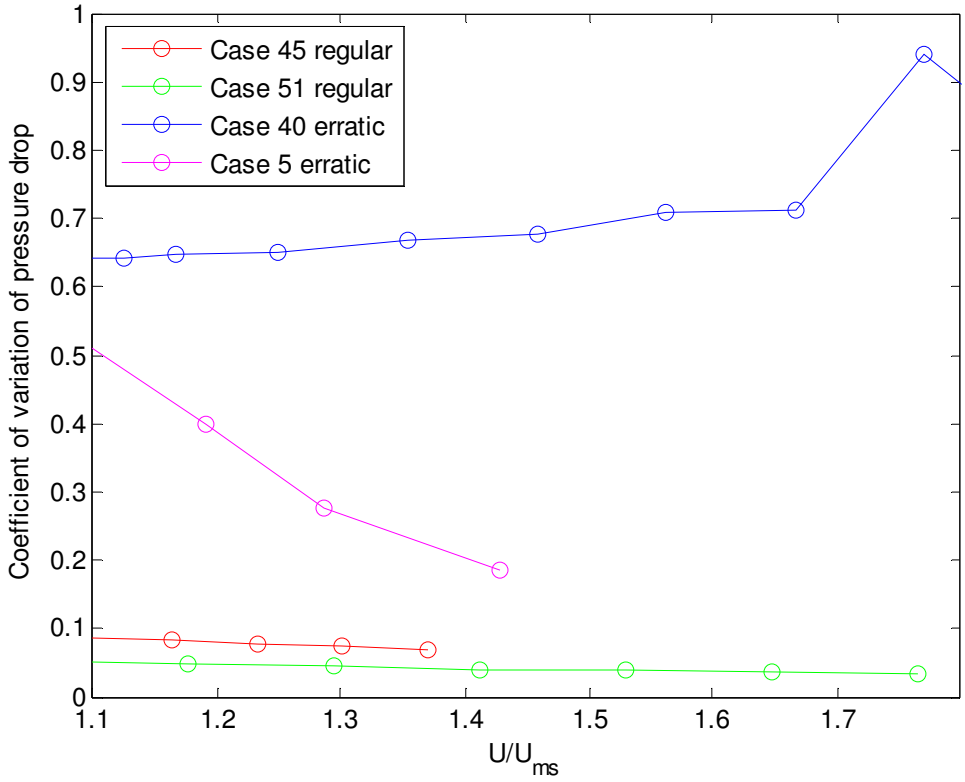

Figure 4.12: Coefficient of variation of bed pressure drop with respect of gas flow rate for typical regular and erratic spouting cases. Note that the cases are defined in Table 3.2 in Section 3.1.

The bimodal spouting regime, the third regime, was identified for very shallow spouted beds (H_0/D_c=0.42) with the largest particles (2000 µm) in the 50 mm bed. At 2 U/U_{ms} the fully spouting bed behaves as a jet spouted bed, while decreasing the gas flow the bed still exhibits jet spouting up to a point where the fountain height and form begins to change intermittently. The intermittent change is driven by the fact that particles accumulate at the bed wall from time to time creating a stagnant wall which makes the fountain height increase as if the diameter of the bed were smaller; and then, groups of particles leave the wall collapsing to form a small mountain of particles that leads to the bed behaving as a regular spouted bed. This intermittent behavior is termed the bimodal spouting regime. Variations of these two spouting modes (jetting and regular) continue to be exhibited while decreasing the gas flow rate, up to a value close to the minimum spouting velocity. Figure 4.13 shows the composite images at different gas flow rates for a typical bimodal regime shallow spouted bed. The fountain height decreases with the gas flow rate from values of U/U_{ms} of 2.67 to 1.96. The apparent increase of fountain height at

U/U_{ms}=1.78 is due to the fact that part of the particles are accumulating on the walls from time to time, changing the fountain height through the time (see
Figure 4.14). The images in this figure show very few particles due to the very shallow spouted bed condition (H_0/D_c=0.42) for the largest particles (2000 µm). The bimodal spouting regime behavior might be related to the relatively small number of particles in the bed making the fluidized particles behave in a very granular form. The accumulation of particles on the wall could be eliminated by increasing the inlet diameter or decreasing the cone angle; an optimal ratio between inlet diameter and column diameter should be investigated in order to guarantee that the annulus area is well aerated to pursue the regular spouting condition; this optimization is left for future research.

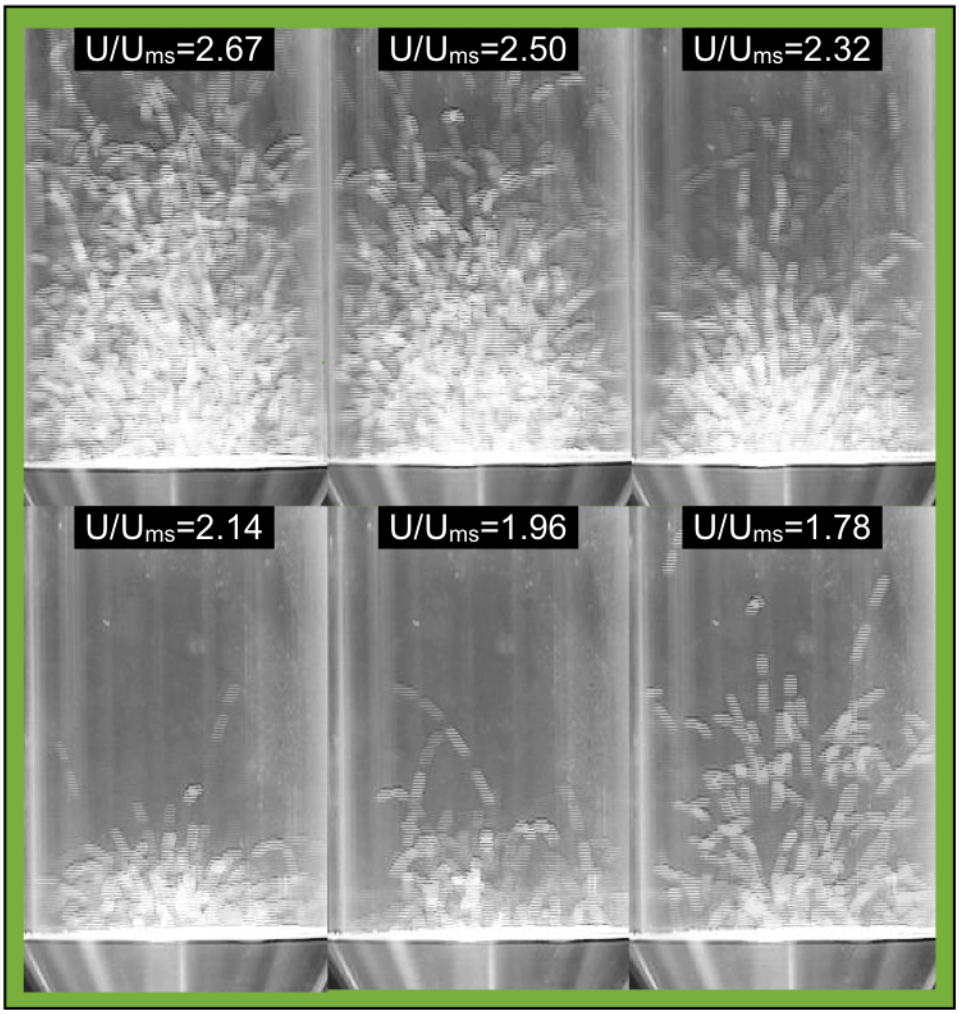

Figure 4.13: Composite images at different gas flow rates for a typical bimodal case. 50 mm bed for 2000 µm Al_2O_3 (U_{ms}=0.24 m/s) particles at H_0/D_c=0.42 using air as the fluidizations gas.

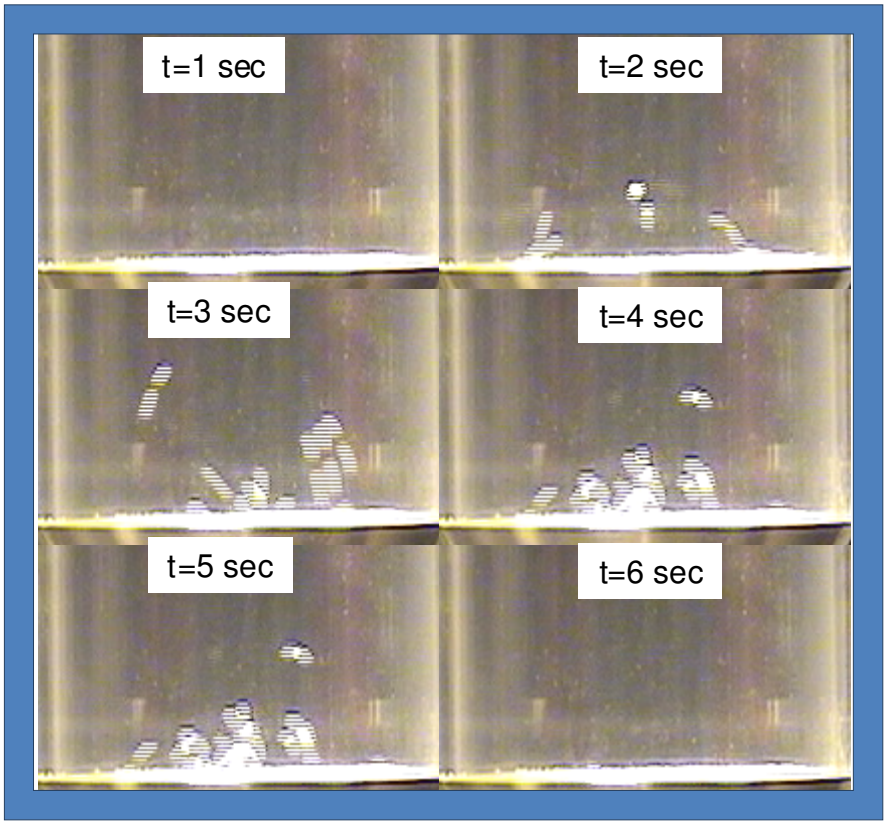

Figure 4.14: Frames extracted from a video with respect of time for a typical bimodal showing the differences through the time of fountain height. 50 mm bed for 2000 μm Al_2O_3 ($U=1.6U_{ms}$) particles at $H_0/D_c=0.42$ using air as the fluidizations gas.

Video files showing the three regimes observed are attached to this dissertation; a video for regular spouting is displayed (File 3, 80-Air-YSZ-H100-500-f1.25.avi), three video files that display erratic spouting cases (File 1,2 and 4, 150-Air-Al2O3-H42-500-f2.6.avi, 150-Air-Al2O3-H42-500-f1.6.avi and 80-He-YSZ-H100-500-f1.25.avi), and two video files that display the bimodal spouting regime (Files 5-6, 80-Air-YSZ-H100-500-f2.5.avi and 80-Air-YSZ-H100-500-f1.6.avi).

4.1.4 *Shallow bed spouting regime map*

A preliminary shallow bed spouting regime map (see Figure 4.15) is proposed to delimit all spouting regimes defined in this research. The placement of each case into a regime was determined by visual observations of fountain height dynamics. A confirmation of the preliminary regime assignments using the coefficient of variation of bed pressure drop and, to a lesser extent, the centroid distance of fountain height as indicators to delimit spouting regimes has been conducted for selected cases and is a promising tool. However, full development of these assessment tools is left for future investigations.

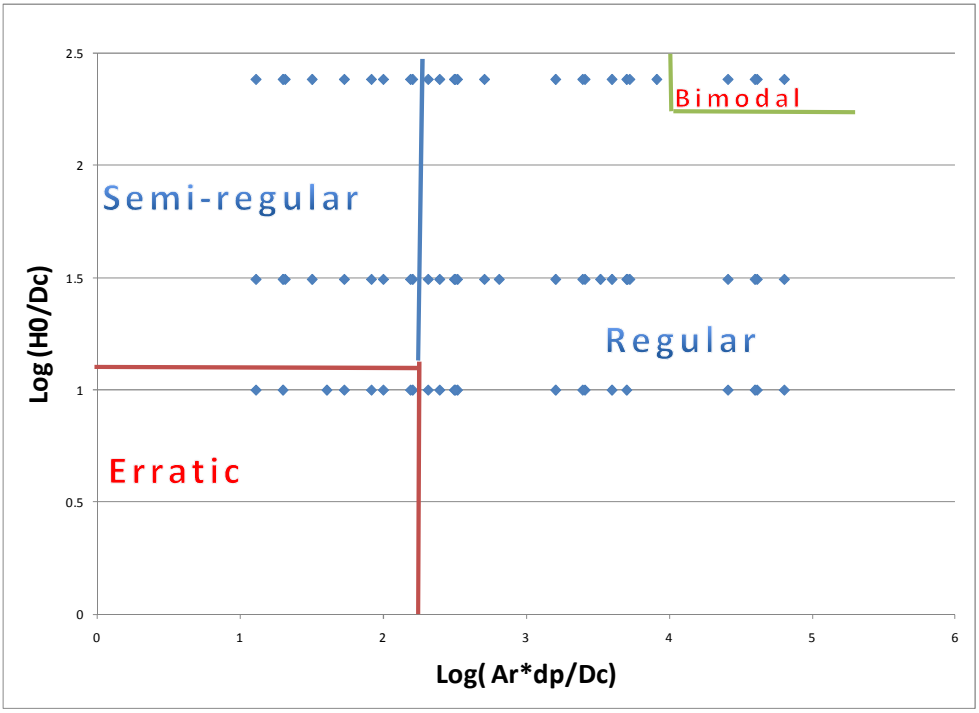

Figure 4.15: Preliminary shallow bed spouting regime map for different particle size, particle density, solid density, gas density, column diameter and static height.

Besides the three spouting regimes already defined, a fourth regime called the 'semi-regular' spouted regime is delimited in the present spouted regime map. The 'semi-regular' regime is a subset of the erratic regime. It corresponds to the cases where the variability in the fountain height was relatively small compared with all of the erratic cases. This reclassification was prompted by the fact that using the maximum fountain height measurements as data points in the H_f correlation did not hurt the performance of the correlation. Thus for this investigation about 2/3 (see Figure 4.15) of the originally identified erratic spouting cases were redefined as semi-regular spouting cases and included with the regular spouting cases in developing correlations for shallow spouted beds. The use of this spouting regime map is recommended to guide the selection of protocols used in shallow bed scaling where appropriate.

The next section lists the operating condition of the experiments considered to develop the hydrodynamic correlations of minimum spouting velocity, bed pressure drop at U_{ms} and fountain height based on the spouting regimes and pressure drop patterns observed and described in this section.

4.1.5 *Operating conditions of experiments used to generate hydrodynamic correlation models*

In this investigation, hydrodynamics of shallow spouted beds for dense particles were characterized by three hydrodynamic variables; minimum spouting velocity, bed pressure drop at minimum spouting condition and fountain height. The effect of the following operating parameters, at ambient temperature and pressure, were studied: particle diameter (500, 1000, 2000 μm), particle density (Alumina, YSZ and SS), column diameter (50, 80 and 150 mm), gas density (0.17 and 1.18 kg/m^3), static bed heights to column diameter ratio (0.42, 0.67 and 1) and gas flow rate. The matrix of cases that include the variations of such operating conditions are listed in Table 3.2. Results from all cases were used to develop the hydrodynamic correlations of minimum spouting velocity while some cases were excluded in developing correlations of fountain height and bed pressure drop depending on the different spouting behavior regimes and bed pressure drop patterns described in the last section.

The minimum spouting velocity correlation was developed considering all experiments performed in Phase A and B of this investigation (see Table 3.2) since U_{ms} was defined independently of spouting regimes. Correlation was analyzed in two stages, one using results from Phase A alone and one using results from both Phase A and B

The bed pressure drop correlation at minimum spouting velocity was developed utilizing only the results of cases listed in Table 4.3. These cases correspond to the experiments where the bed pressure drop is positive at values of $U/U_{ms}>1$. These cases exhibit mostly the first, second and fourth bed pressure drop classifications listed in Table 4.1.

Table 4.3: Operating conditions of cases used to correlate bed pressure drop at minimum spouting condition

No.	D_c [mm]	ρ_s [kg/m^3]	H_0/D_c	d_p	ρ_g [kg/m^3]	Reference or validation for ΔP_{ms} models
1	50	3880	0.42	500	0.17	V
2	50	3880	0.67	500	0.17	V
3	50	3880	0.42	500	1.18	R
4	50	3880	0.67	500	1.18	V
5	50	6000	0.42	500	0.17	R
6	50	6000	0.67	500	0.17	V
7	50	6000	1	500	1.18	R
8	50	6000	0.42	500	1.18	R
9	50	6000	0.67	500	1.18	V
10	50	7600	1	500	0.17	R
11	50	7600	0.67	500	1.18	R
12	50	7600	0.42	500	1.18	R
13	50	3880	0.42	1000	0.17	R
14	50	3880	0.67	1000	0.17	V
15	50	3880	1	1000	1.18	V
16	50	3880	0.67	1000	1.18	V
17	50	3880	0.42	1000	1.18	V
18	50	6000	0.67	1000	0.17	R
19	50	6000	0.42	1000	0.17	V
20	50	6000	1	1000	1.18	R
21	50	6000	0.67	1000	1.18	V
22	50	6000	0.42	1000	1.18	V
23	50	7600	0.67	1000	1.18	R
24	50	6000	0.67	2000	1.18	R
25	80	3880	0.67	500	0.17	R

Table 4.3: Operating conditions of cases used to correlate bed pressure drop at minimum spouting condition (Continued)

No.	D_c [mm]	ρ_s [kg/m^3]	H_0/D_c	d_p	ρ_g [kg/m^3]	Reference or validation for ΔP_{ms} models
26	80	3880	1	500	0.17	R
27	80	3880	0.67	500	1.18	R
28	80	3880	0.42	500	1.18	R
29	80	3880	1	500	1.18	V
30	80	6000	1	500	0.17	V
31	80	6000	0.67	500	1.18	R
32	80	6000	1	500	1.18	R
33	80	6000	0.42	500	1.18	R
34	80	3880	1	1000	0.17	R
35	80	3880	0.42	1000	0.17	R
36	80	3880	0.67	1000	0.17	V
37	80	3880	0.42	1000	1.18	R
38	80	3880	1	1000	1.18	R
39	80	3880	0.67	1000	1.18	V
40	80	6000	0.42	1000	0.17	R
41	80	6000	1	1000	0.17	V
42	80	6000	0.67	1000	1.18	R
43	80	6000	0.42	1000	1.18	V
44	150	3880	0.42	500	1.18	V
45	150	3880	0.67	500	1.18	V
46	150	6000	1	500	1.18	R
47	150	6000	0.42	500	1.18	R

The fountain height correlation was developed employing the results of regular and semiregular cases listed in Table 4.4. Several cases where the fountain height exhibited instability in size and form were excluded from the total experiments performed in Phases A and B. Cases excluded correspond mostly to the erratic and bimodal spouting behaviors as listed in Table 4.2. See Figure 4.15 for the classification of the cases into regions delineated by H_o/D_c and Ar^*d_p/D_c.

Table 4.4: Operating conditions of cases used to correlate fountain height

No.	D_c [mm]	ρ_s [kg/m^3]	H_0/D_c	d_p	ρ_g [kg/m^3]	U/U_{ms}	Reference or validation for H_f model
1	50	3880	0.42	500	0.17	1.2	V
	50	3880	0.42	500	0.17	1.8	V
2	50	3880	0.42	500	1.18	1.2	R
	50	3880	0.42	500	1.18	1.8	R
3	50	3880	0.67	500	0.17	1.2	V
	50	3880	0.67	500	0.17	1.8	V
4	50	3880	0.67	500	1.18	1.2	V
	50	3880	0.67	500	1.18	1.8	V
5	50	3880	1	500	1.18	1.2	R
	50	3880	1	500	1.18	1.8	R
6	50	6000	0.42	500	0.17	1.2	R
	50	6000	0.42	500	0.17	1.8	R
7	50	6000	0.42	500	1.18	1.2	R
	50	6000	0.42	500	1.18	1.8	R
8	50	6000	0.67	500	0.17	1.2	V
	50	6000	0.67	500	0.17	1.8	V
9	50	6000	0.67	500	1.18	1.2	V
	50	6000	0.67	500	1.18	1.8	V
10	50	6000	1	500	1.18	1.2	R
	50	6000	1	500	1.18	1.8	R
11	50	7600	0.42	500	1.18	1.2	R
	50	7600	0.42	500	1.18	1.8	R
12	50	7600	0.67	500	1.18	1.2	R
	50	7600	0.67	500	1.18	1.8	R
13	50	7600	1	500	0.17	1.2	R
	50	7600	1	500	0.17	1.8	R
14	50	7600	1	500	1.18	1.2	V
	50	7600	1	500	1.18	1.8	V
15	50	3880	0.42	1000	0.17	1.2	R
	50	3880	0.42	1000	0.17	1.8	R
16	50	3880	0.42	1000	1.18	1.2	V
	50	3880	0.42	1000	1.18	1.8	V

Table 4.4: Operating conditions of cases used to correlate fountain height (Continued)

No.	D_c [mm]	ρ_s [kg/m^3]	H_0/D_c	d_p	ρ_g [kg/m^3]	U/U_{ms}	Reference or validation for H_f model
17	50	3880	0.67	1000	0.17	1.2	V
	50	3880	0.67	1000	0.17	1.8	V
18	50	3880	0.67	1000	1.18	1.2	V
	50	3880	0.67	1000	1.18	1.8	V
19	50	3880	1	1000	0.17	1.2	V
	50	3880	1	1000	0.17	1.8	V
20	50	3880	1	1000	1.18	1.2	V
	50	3880	1	1000	1.18	1.8	V
21	50	6000	0.42	1000	0.17	1.2	V
	50	6000	0.42	1000	0.17	1.8	V
22	50	6000	0.42	1000	1.18	1.2	V
	50	6000	0.42	1000	1.18	1.8	V
23	50	6000	0.67	1000	0.17	1.2	R
	50	6000	0.67	1000	0.17	1.8	R
24	50	6000	0.67	1000	1.18	1.2	V
	50	6000	0.67	1000	1.18	1.8	V
25	50	6000	1	1000	1.18	1.2	R
	50	6000	1	1000	1.18	1.8	R
26	50	7600	0.42	1000	1.18	1.2	V
	50	7600	0.42	1000	1.18	1.8	V
27	50	7600	0.67	1000	0.17	1.2	R
	50	7600	0.67	1000	0.17	1.8	R
28	50	7600	0.67	1000	1.18	1.2	R
	50	7600	0.67	1000	1.18	1.8	R
29	50	7600	1	1000	1.18	1.2	R
	50	7600	1	1000	1.18	1.8	R
30	50	3880	0.42	2000	0.17	1.2	R
	50	3880	0.42	2000	0.17	1.8	R
31	50	3880	0.67	2000	0.17	1.2	R
	50	3880	0.67	2000	0.17	1.8	R
32	50	3880	0.67	2000	1.18	1.2	V
	50	3880	0.67	2000	1.18	1.8	V
33	50	3880	1	2000	1.18	1.2	V
	50	3880	1	2000	1.18	1.8	V
34	50	6000	0.42	2000	0.17	1.2	R
	50	6000	0.42	2000	0.17	1.8	R

Table 4.4: Operating conditions of cases used to correlate fountain height (Continued)

No.	D_c [mm]	ρ_s [kg/m^3]	H_0/D_c	d_p	ρ_g [kg/m^3]	U/U_{ms}	Reference or validation for H_f model
35	50	6000	0.42	2000	1.18	1.2	R
	50	6000	0.42	2000	1.18	1.8	R
36	50	6000	0.67	2000	1.18	1.2	R
	50	6000	0.67	2000	1.18	1.8	R
37	50	6000	1	2000	1.18	1.2	R
	50	6000	1	2000	1.18	1.8	R
38	80	3880	0.42	500	0.17	1.2	V
	80	3880	0.42	500	0.17	1.8	V
39	80	3880	0.42	500	1.18	1.2	R
	80	3880	0.42	500	1.18	1.8	R
40	80	3880	0.67	500	0.17	1.2	R
	80	3880	0.67	500	0.17	1.8	R
41	80	3880	0.67	500	1.18	1.2	R
	80	3880	0.67	500	1.18	1.8	R
42	80	3880	1	500	1.18	1.2	V
	80	3880	1	500	1.18	1.8	V
43	80	6000	0.42	500	0.17	1.2	V
	80	6000	0.42	500	0.17	1.8	V
44	80	6000	0.42	500	1.18	1.2	R
	80	6000	0.42	500	1.18	1.8	R
45	80	6000	0.67	500	0.17	1.2	V
	80	6000	0.67	500	0.17	1.8	V
46	80	6000	0.67	500	1.18	1.2	R
	80	6000	0.67	500	1.18	1.8	R
47	80	6000	1	500	0.17	1.2	V
	80	6000	1	500	0.17	1.8	V
48	80	6000	1	500	1.18	1.2	R
	80	6000	1	500	1.18	1.8	R
49	80	3880	0.42	1000	0.17	1.2	R
	80	3880	0.42	1000	0.17	1.8	R
50	80	3880	0.42	1000	1.18	1.2	R
	80	3880	0.42	1000	1.18	1.8	R

Table 4.4: Operating conditions of cases used to correlate fountain height (Continued)

No.	D_c [mm]	ρ_s [kg/m^3]	H_0/D_c	d_p	ρ_g [kg/m^3]	U/U_{ms}	Reference or validation for H_f model
51	80	3880	0.67	1000	0.17	1.2	V
	80	3880	0.67	1000	0.17	1.8	V
52	80	3880	1	1000	0.17	1.2	R
	80	3880	1	1000	0.17	1.8	R
53	80	6000	0.42	1000	0.17	1.2	R
	80	6000	0.42	1000	0.17	1.8	R
54	80	6000	0.42	1000	1.18	1.2	V
	80	6000	0.42	1000	1.18	1.8	V
55	80	6000	0.67	1000	0.17	1.2	V
	80	6000	0.67	1000	0.17	1.8	V
56	80	6000	0.67	1000	1.18	1.2	R
	80	6000	0.67	1000	1.18	1.8	R
57	80	6000	1	1000	0.17	1.2	V
	80	6000	1	1000	0.17	1.8	V
58	80	6000	1	1000	1.18	1.2	V
	80	6000	1	1000	1.18	1.8	V
59	80	3880	0.42	2000	1.18	1.2	V
	80	3880	0.42	2000	1.18	1.8	V
60	80	3880	0.67	2000	0.17	1.2	R
	80	3880	0.67	2000	0.17	1.8	R
61	80	3880	0.67	2000	1.18	1.2	V
	80	3880	0.67	2000	1.18	1.8	V
62	80	6000	0.42	2000	1.18	1.2	V
	80	6000	0.42	2000	1.18	1.8	V
63	80	6000	0.67	2000	0.17	1.2	V
	80	6000	0.67	2000	0.17	1.8	V
64	80	6000	0.67	2000	1.18	1.2	R
	80	6000	0.67	2000	1.18	1.8	R

Following sections presents the analysis and results of correlating minimum spouting velocity, pressure drop and fountain height as a function of different parameters varied in this investigation expressed as dimensionless variables.

4.2. Developing regression model for U_{ms}

This section presents the analysis and results of correlating U_{ms} as a function of four dimensionless variables, which are derived from published literature on scaling factors [14] for deep spouted beds, and from the most commonly used dimensionless variables in the reported U_{ms} correlations (see Table 1.2). These variables include $\frac{gd_p}{U^2}, \frac{\rho_s d_p U}{\mu_g}, \frac{\rho_g}{\rho_s}, \frac{H_0}{d_p}, \frac{D_c}{d_p}, Ar$. From Phase A, results from 30 reference experiments (see Table 3.2), were analyzed. The correlation pattern between dimensionless variables and U_{ms} was explored by applying principal component analysis (PCA) as described in Section 3. The more dominant variables in determining U_{ms} are identified. Subsequently, a regression model using the same set of results was carried out for U_{ms} with respect to four dimensionless variables $\left(\frac{d_p}{D_c}, Ar, \frac{\rho_s}{\rho_g}, \frac{H_0}{d_p}\right)$ by applying principal component regression (PCR), also described in Section 4. Results from additional 23 experiments are used to validate the developed regression model. Finally, from Phase B experiments, an expanded regression model was developed by incorporating two additional variations; a bigger column diameter (150 mm) and a bigger particle diameter (2000 μm) as listed in Table 3.2. Results of PCA and PCR presented in this section suggest that d_p/D_c, H_0/d_p and ρ_s/ρ_g are more influential in defining minimum spouting velocity.

4.2.1 *Correlation pattern between U_{ms} and four chosen dimensionless variables.*

The correlation pattern between four dimensionless variables X (Equation 4.2) and normalized U_{ms} was explored first using PCA. The objective is to see which variables are more correlated to and which have relatively little influence with U_{ms}.

The four dimensionless variables used are:

$$X = \left[\frac{d_p}{D_c}, Ar, \frac{\rho_s}{\rho_g}, \frac{H_0}{d_p}\right] \qquad 4.2$$

Where $Ar = \frac{d_p^3 \rho_g (\rho_s - \rho_g) g}{\mu^2}$ is the Archimedes number, denoting the buoyancy effect.

Values for these four dimensionless variables are derived from the values of the various design parameters as listed in Table 3.2. They are static bed height (H_0), particle diameter (d_p), column diameter (D_c), and particle and gas densities (ρ_s and ρ_g). According to literature reference, these dimensionless variables are found to have influence on U_{ms} for spouted beds (see Table 1.2). So we start with these parameters also.

30 experiments from the experiments of Phase A were used for PCA (see Table 3.2). Those experiments were performed based on fractional design of experiments, involving 2 particle diameters, 3 particle densities, 2 bed sizes, 2 fluidization gases, 3 static bed heights. The minimum spouting velocity was the measured dependent variable.

A data matrix was created by concatenating the measured U_{ms} vector column with the 30×4 treatment level data matrix to create a 30×5 overall data matrix as shown below.

$$\begin{bmatrix} \vdots & \vdots & \vdots & \vdots & \vdots \\ \frac{U_{ms}}{U_t} & \frac{d_p}{D_c} & Ar & \frac{\rho_s}{\rho_g} & \frac{H_0}{d_p} \\ \vdots & \vdots & \vdots & \vdots & \vdots \end{bmatrix}$$

The raw data were preprocessed according to procedures described in section 4, resulting in normalized and mean centered data. The preprocessed data matrix, referred to as X, was then subjected to a SVD, and the SVD results are listed in **Table 4.5**.

In SVD of X, X=USV', where S represents the singular value matrix whose diagonal elements are the singular values of X and the column vectors of V represent the principal component(PC) vectors, and V is an orthogonal matrix.

Table 4.5: V vectors and S values

V =

0.1765	-0.0098	0.8127	0.3975	0.3877
0.1545	-0.3412	0.0449	0.5545	-0.7418
0.8644	-0.2521	0.0332	-0.4329	-0.0256
-0.4183	-0.8024	0.2373	-0.3518	0.0333
-0.1508	0.4196	0.5293	-0.4726	-0.5456

S =

9.2447	0	0	0	0
0	4.4198	0	0	0
0	0	3.2540	0	0
0	0	0	1.6246	0
0	0	0	0	0.2908

Columns of V show the makeup of the principal components from the original variables. Principal component spacing vectors are orthonormal to each other. Each of the principal component vectors is a linear combination of the five original *x*-variables and displays the correlation pattern between U_{ms}/U_t and the four dimensionless variables $\left(\frac{d_p}{D_c}, Ar, \frac{\rho_s}{\rho_g}, \frac{H_0}{d_p}\right)$. Each of the singular values squared ratioed to the sum of squares of all singular values indicates the relative percent of variance that each principal component contributes to the overall variance captured in the X data matrix. The variance contributed by each principal component is as follows.

d3 =
0.7224
0.1651
0.0895
0.0223
0.0007

Cumulative variance vector is shown below and it is shown as scree plot in Figure 4.16.

d4 =
0.7224
0.8875
0.9770
0.9993
1.0000

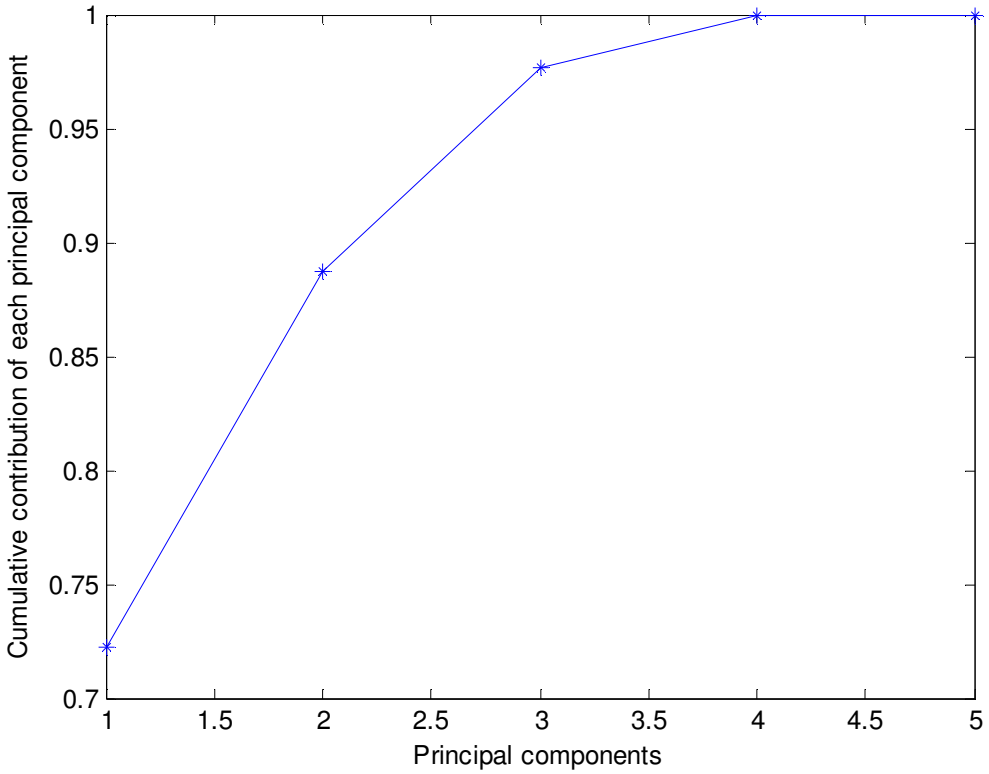

Figure 4.16: Scree plot showing the cumulative variance contributed by the principal components.

From the V vectors, it can be seen that the largest x-variable correlated to U_{ms} appears to be H_0/d_p (from v_3). Notice that the correlation between U_{ms}/U_t (v_{31}) and H_0/d_p is positive meaning that the larger the H_0/d_p is, the larger U_{ms}/U_t will be; which is supported by the underlying physics; the bigger the static height, the bigger the superficial gas velocity (U) has to be to effect in spouting. The analysis of v_1 is neglected since U_{ms}/U_t has a small weight here, however it should be mentioned that v_1 corresponds to the largest variance on X matrix and since it is highly weighted by Ar, it means that the large variance on Ar does not seem to affect too much the values of U_{ms}/U_t, e.g. uncorrelated, which also appears to be physically reasonable, since Ar represents the buoyant force due to the gas and since the density of the gas is so much smaller than that of the particles(e.g. 6000 vs. 1.18 kg/m^3), the buoyant force is practically negligible. From the last V vector, v_5, which has a correspondingly very small singular value compared to the first singular value, it is seen that U_{ms}/U_t, d_p/D_c and H_0/d_p are correlated, even though v_5 contributes relative nothing to the variance. In other words, v_5 is in the null space of the matrix X, implying that linear combination of the original five x variables as indicated by the components of v_5 gives '0' as shown below.

$$0.38x_1 - 0.74x_2 - 0.03x_3 + 0.03x_4 - 0.55x_5 \approx 0 \qquad 4.3$$

or

$$0.38x_1 - 0.74x_2 - 0.55x_5 \approx 0 \qquad 4.4$$

where

$$x_1 \approx 2x_2 + 1.4x_5 \qquad 4.5$$

Suggesting that $x_1(U_{ms}/U_t)$, $x_2(d_p/D_c)$ and x_5 (H_0/d_p) are all positively correlated. It is also seen that the higher H_0 is with respect to d_p, the bigger U_{ms} would be and the higher d_p with respect D_c the bigger U_{ms} would be. So, in addition to H_0/d_p, d_p/D_c also appears to be important.

Finally, a weaker correlation exists between U_{ms}/U_t and all the four dimensionless variables by the comparable weighting of all five variables in the v_4 principal component vector. The relative signs indicate that U_{ms}/U_t, (d_p/D_c) are positive correlated; whereas some experimental values of U_{ms}/U_t, Ar, ρ_s/ρ_g and d_p/D_c are negatively correlated. The correlation is rather weak, since the variance captured by the third PC is only 2%, implying that any correlation pattern displayed by this PC is ambiguous.

In short summary, the variables H_0/d_p and d_p/D_c appear to be the most correlated with U_{ms}/U_t; whereas Ar appears to have very little influence over U_{ms}/U_t, and the effect of ρ_s/ρ_g is somewhat present but rather weak.

4.2.2 *Regression model developed for U_{ms} with respect to the same four dimensionless variables*

A regression model was then developed using the PCR approach for $Y=U_{ms}/U_t$ with respect to the same four dimensionless variables used for PCA, using results from the 30 reference experiments:

$$X = \left[\frac{d_p}{D_c}, Ar, \frac{\rho_s}{\rho_g}, \frac{H_0}{d_p} \right] \text{ and } Y = \frac{U_{ms}}{U_t} \qquad 4.6$$

Data used for PCR is listed in Table 3.2. From the 53 experiments of phase A, the same 30 experiments values used for PCA and the measured corresponding minimum spouting velocities were used to develop the reference regression model, and 23 additional experiments from phase A, were used to validate the reference PCR model. The purpose of the PCR was to determine a quantitative relationship between U_{ms} and the dimensionless variables that can be used for modeling and prediction.

The X data was preprocessed according to procedures described in Section 3, resulting in a normalized and mean centered data matrix. The resulting preprocessed X data was subjected to SVD and results are listed in **Table 4.6**.

Table 4.6: V vectors and S values

V =

0.15	-0.34	0.16	-0.91
0.88	-0.25	-0.37	0.18
-0.43	-0.80	-0.39	0.16
-0.16	0.42	-0.83	-0.33

S =

9.11	0	0	0
0	4.42	0	0
0	0	2.16	0
0	0	0	1.00

The variance contributed by each principal component is as follows.

d3 =

0.77
0.18
0.04
0.01

Cumulative variance vector is shown below in Figure 4.17, as a scree plot.

d4 =

0.77
0.95
0.99
1.00

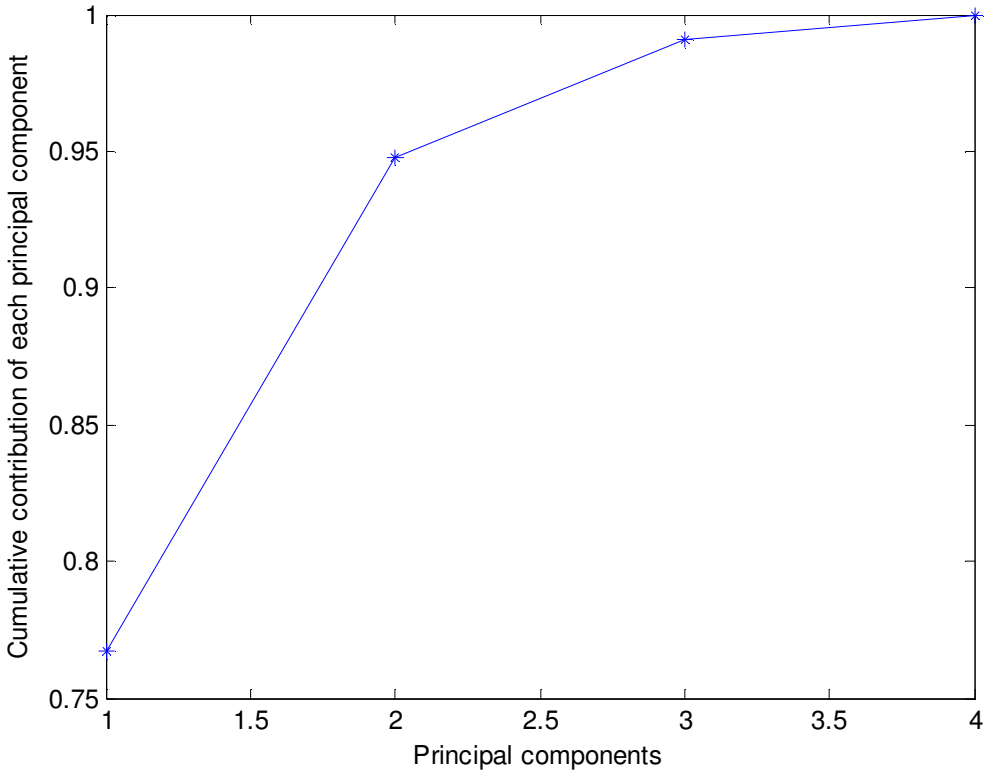

Figure 4.17: Scree plot showing the cumulative variance contributed by the principal components.

From the scree plot it is seen that three principal components would capture almost all the variance embedded in the X data matrix, and that the fourth dimension contributes practically no variation. Even though the fourth principal component was found to contribute practically nothing to the overall data variance, it was not deleted from the PCR process because it was found that the resulting regression was rather poor with it being deleted. This suggests that even though the data along the fourth principal component (PC) direction did not vary much among the design data values, this part of the data appears to be correlated to the output variable Y enough to warrant against its deletion. Therefore, four PC's are kept for modeling by PCR.

Each column of the V matrix from the SVD of X is a principal component, and shows the makeup of that PC from the original variables. Each principal component vector is a linear combination of the four original *x*-variables. As can be seen in the loadings plot of the V vectors (see Figure 4.18), the first column is heavily weighted by x_2 (Ar) alone; the second column is heavily weighted by x_3 (ρ_s/ρ_g) alone, the third column is weighted by x_4 (H_0/d_p) alone and the fourth column is weighted by x_1 (d_p/D_c), showing almost a decoupled and rearranged distribution pattern for the four independent variables.

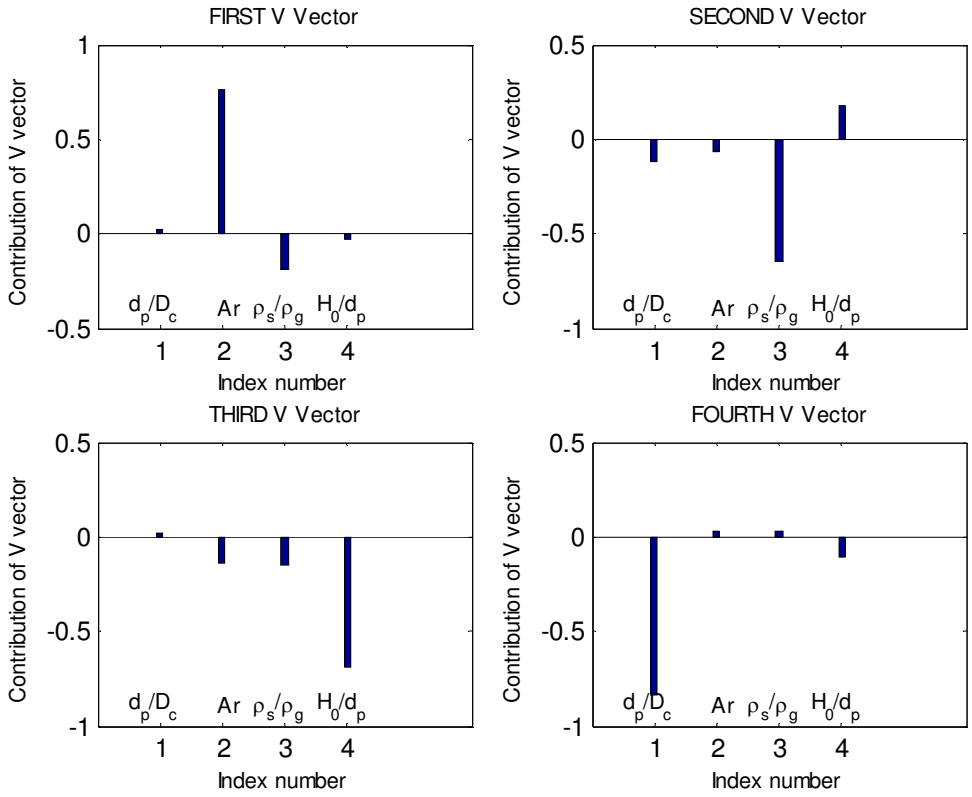

Figure 4.18: Relative make up of each principal component.

The four regression coefficients in the 'V' frame are:

β_v =

0.16
-0.01
-0.84
-2.02

So the regression model can be expressed by the following equation.

$$y = 0.16v_1 - 0.01v_2 - 0.84v_3 - 2.02v_4 \qquad 4.7$$

where the 'v' variables are the PC vectors.

It can be seen that βv_4 and βv_3 being 2.02 and 0.84 in magnitude are much higher than the first two coefficients. The vectors v_4 and v_3 are much heavily weighted by d_p/D_c and H_0/d_p respectively, suggesting that when transformed back to the original frame of reference, the

regression coefficients associated with d_p/D_c and H_0/d_p would be greater than those for the other two dimensionless variables. This is indeed so. This correlation pattern for U_{ms}/U_t was also observed from the PCA study where d_p/D_c and H_0/d_p were found to be very strongly correlated with U_{ms}. The regression coefficients of 0.16 and -0.01 associated with v1 and v2 respectively, are small compared among all four. v_1 is heavily weighted by x_2 (Ar) and v_2 is heavily weighted by x_3 (ρ_s/ρ_g) suggesting that Ar and ρ_s/ρ_g are the least correlated to U_{ms}/U_t; supporting observations made from previous PCA.

The regression coefficients, when expressed in the original variables are shown below.

β =

1.74	d_p/D_c
0.09	Ar
-0.06	ρ_s/ρ_g
1.33	H_0/d_p

Regression coefficients, expressed in the original variables are harder to interpret because the four dimensionless variables are not all truly independent of each other, as can be observed from the SVD analysis, thus confounding the relationship between U_{ms}/U_t and the four variables. The 'β' coefficients, as expressed in the original variables, appear to suggest that d_p/D_c and H_0/d_p are the more influential factors in determining U_{ms}/U_t .

The comparison between the original U_{ms}/U_t values to their corresponding fitted values (on the regression line) by the PCR model is shown in Figure 4.19. Note that the regression is rather good, indicated by a R^2 value of 0.94. In addition, the residual distribution shown in Figure 4.20 appears acceptable too, in that the residuals appear to be evenly distributed with constant variance.

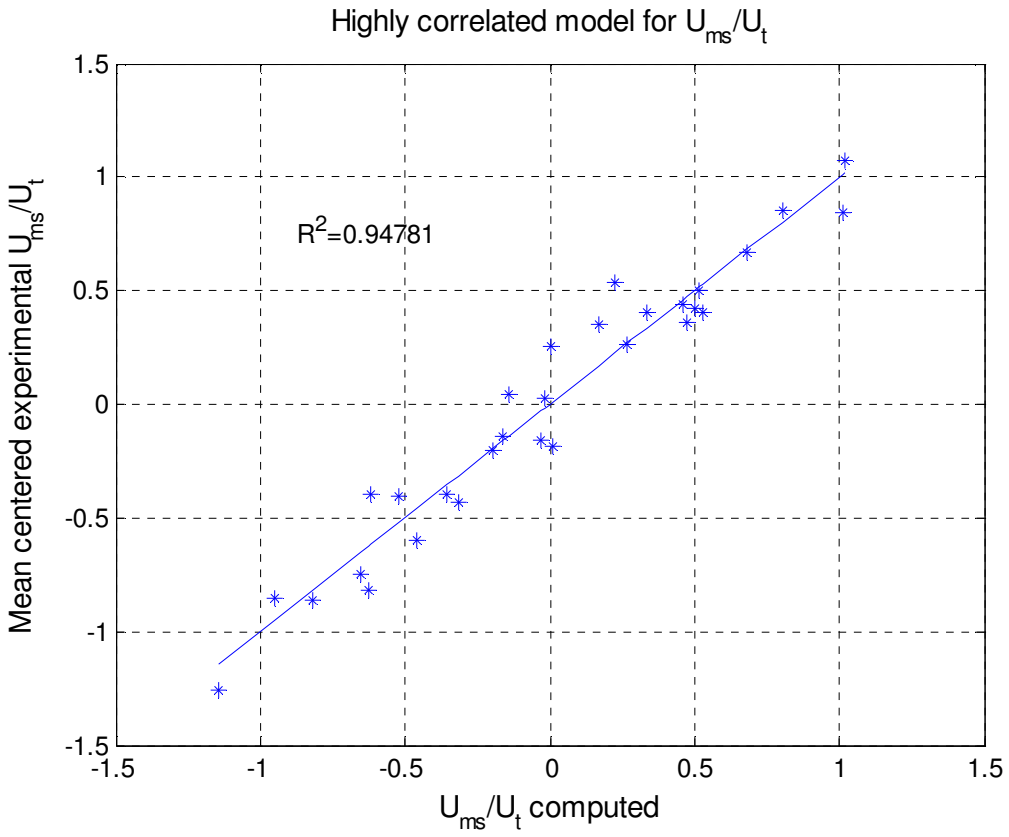

Figure 4.19: Measured versus predicted U_{ms}/U_t values for 30 reference data points using the regression model, showing the relatively little scattering between the measured and the predicted U_{ms} values.

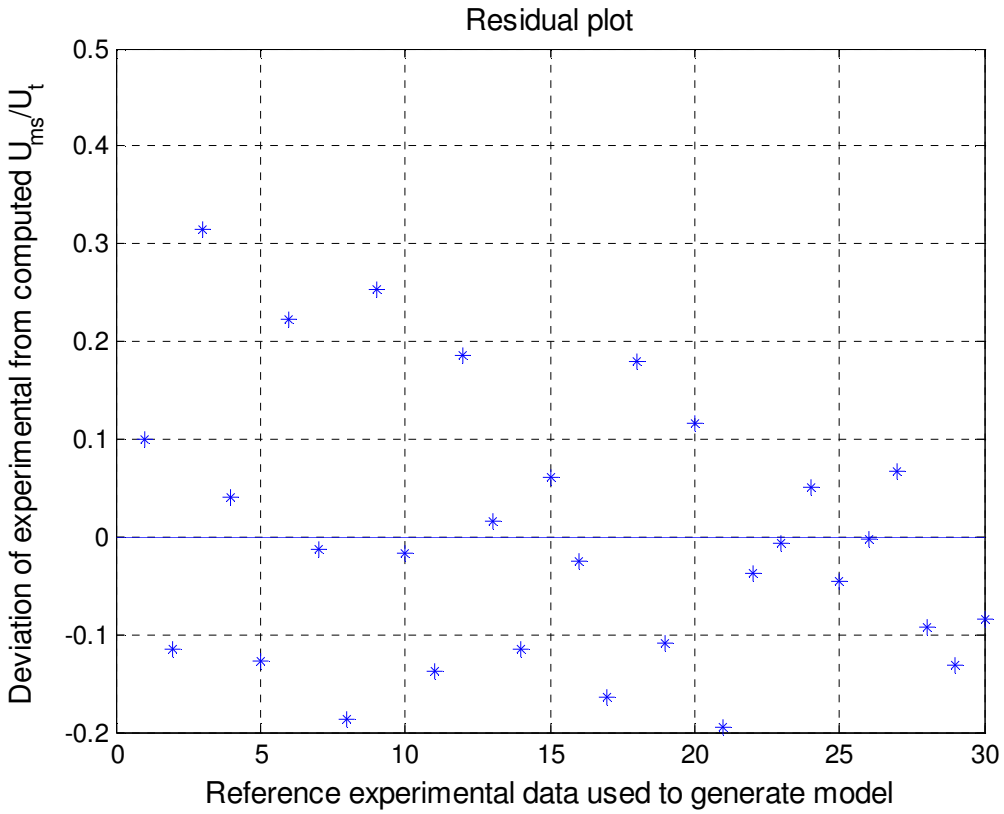

Figure 4.20: Fitting residuals from modeling PCR, using 30 experimental points against index number of sample points, showing the even distribution around 0 (suggesting that the noise contained in the data is not biased).

A validation process was done next using the developed regression model for U_{ms}/U_t to fit results from a separate set of 23 experiments extracted from the 53 experiments done in phase A. Figure 4.21 is a plot showing the scattering of the original 23 U_{ms}/U_t values compared to their corresponding fitted values (on the regression line) by the PCR model developed from the 30 reference experiments. R^2 value is of 0.96, also fairly good, and the residual distribution is shown in Figure 4.22 which appears comparable in magnitude to that for the reference data. Since the division of the original 53 experiments into the 30 reference and 23 validation sets was made at random, positive results increase one's confidence in seeing that model developed from the reference data predicts very closely the 23 validation set of U_{ms} values.

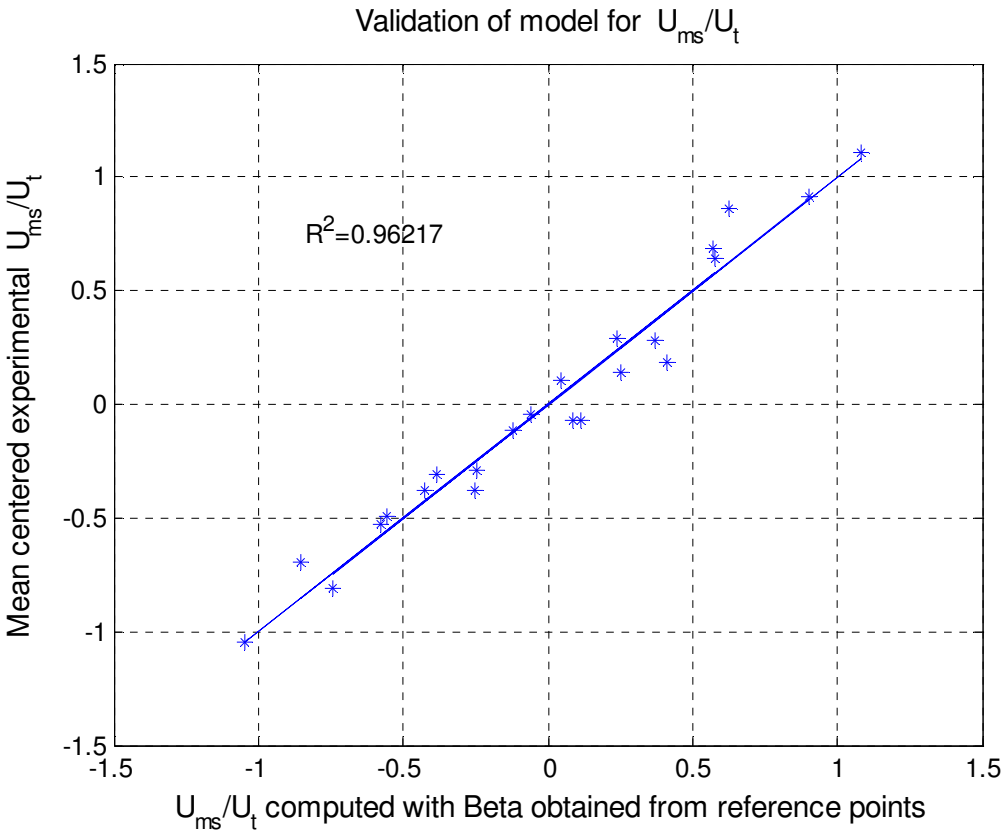

Figure 4.21: Measured versus predicted U_{ms}/U_t values for 23 validation data points, showing the relatively little scattering between the measured and the predicted U_{ms}/U_t values.

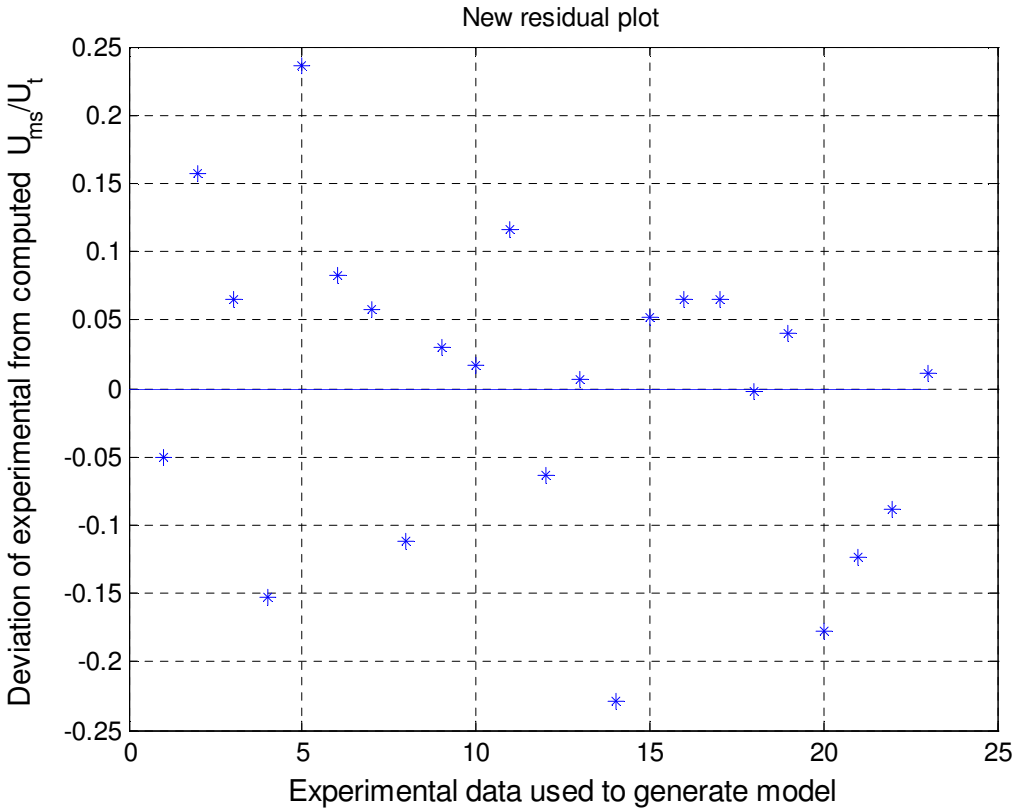

Figure 4.22: Fitting residuals from modeling PCR, using 23 validation sets against index number of sample points, showing the even distribution around 0 (suggesting that the noise contained in the data is indeed Gaussian, and not biased).

Since the validation data is highly predictable by the regression model obtained from the reference data, it is reasonable to claim that the variables that determine better the minimum spouting velocity are $\frac{d_p}{D_c}, \frac{H_0}{d_p}$, while $\frac{\rho_s}{\rho_g}$ and Ar have minor effect on U_{ms}.

The next section presents modeling results of an extended regression model for U_{ms}, incorporating results from an additional set of experiments performed in phase B which incorporate a third variation on column diameter (150 mm) and third particle size (2000 μm). For reference, the reader is referred to Table 3.2 showing the design values used for phase A and B.

4.2.3 *Extended regression model for U_{ms} with respect to the same four dimensionless variables incorporating additional experimental results.*

An expanded regression model for U_{ms} was developed using PCR with respect to the same four dimensionless variables reported in the previous section. Additional to the 53 sets of experimental results used in Phase A, results of experiments performed in Phase B (see Table 3.2) are incorporated to include the biggest diameter bed (150 mm) and the biggest particle diameter (2000 μm) considered in this investigation. For this new model, U_{ms} is scaled by the terminal velocity (U_t). The terminal velocity of a particle depends on the same set of parameters used in this investigation, except for static bed height and column diameter [1].

$$U_t = \sqrt{\frac{4d_p(\rho_s - \rho_g)g}{3\rho_g C_D}} \tag{4.8}$$

where 'g' denotes the gravitational force constant, and CD denotes the drag coefficient computed by Haider and Levenspiel[1] which is expressed as follows:

$$C_D = \frac{24}{\mathrm{Re}_{pt}}\left[1 + \left(8.1716e^{-4.0655\phi_s}\right)\mathrm{Re}_{pt}^{0.0964+0.5565\phi_s}\right] + \frac{73.69\left(e^{-5.0748\phi_s}\right)\mathrm{Re}_{pt}}{\mathrm{Re}_{pt} + 5.378e^{6.2122\phi_s}} \tag{4.9}$$

where Re_{pt} and ϕ_s denotes the particle Reynolds number at U_t and particle sphericity respectively.

This section presents the analysis of correlating U_{ms}/U_t to the four significant dimensionless variables (X) used in the previous sections to obtain an expanded regression model.

$$X = \left[\frac{d_p}{D_c}, Ar, \frac{\rho_s}{\rho_g}, \frac{H_0}{d_p}\right] \tag{4.10}$$

Results of a total of 75 experiments performed in Phases A and B were used for developing and validating the regression model; results of 40 randomly chosen experiments were used to generate a PCR model and results from 35 were used for validation. The purpose of this expanded model is to widen the range of operating conditions in predicting U_{ms}/U_t. Both, the reference and validating data sets contain experiments performed in Phase B.

A new data matrix 'X' of dimension of 40x4 was normalized and mean centered according to procedures described in Section 3. Then the resultant matrix was subjected to a SVD and results are listed below:

Table 4.7: V vectors and S values

V =

-0.29	0.38	-0.17	-0.86
-0.90	-0.15	0.38	0.16
0.15	0.78	0.59	0.18
0.30	-0.48	0.69	-0.45

S =

12.59	0	0	0
0	6.64	0	0
0	0	2.66	0
0	0	0	1.25

The following vector presents the variance contributed by each principal component which is obtained from singular values squared divided by the sum of squares of the singular values.

d3 =

0.75
0.21
0.03
0.01

Cumulative variance vector is shown below and is shown as a scree plot in Figure 4.23.

d4 =

0.75
0.96
0.99
1.00

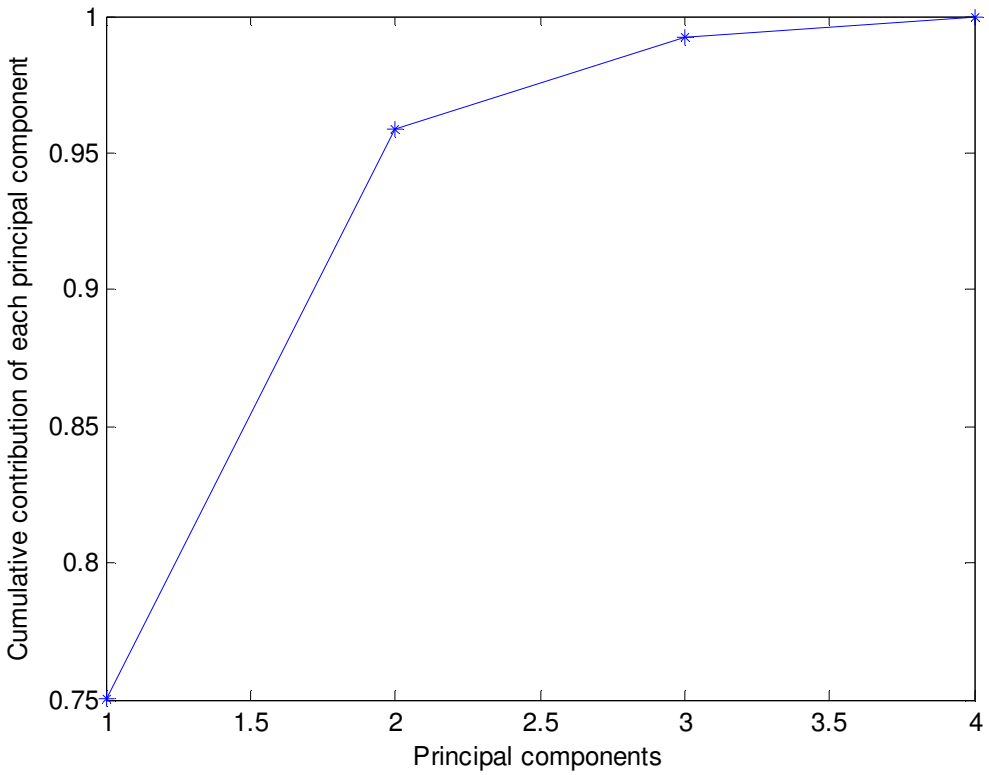

Figure 4.23: Scree plot showing the cumulative variance contributed by the principal components for the reference data set.

Similar to previous PCR model, from the scree plot it is seen that three principal components account for almost all the variance embedded in the X data matrix. Even though the variance contributed by the last principal component is practically zero, it was kept in the PCR process since when deleted the regression becomes poor, suggesting that the fourth principal component is correlated to the output variable Y.

The relative make up of each principal component is displayed in Figure 4.24. The first column is heavily weighted by x_2 (Ar), the second column is heavily weighted by x_3 (ρ_s/ρ_g), the third column is weighted by a combination of the variables x_3 and x_4 (ρ_s/ρ_g , H_0/d_p) and the fourth column is heavily weighted by x_1 (d_p/D_c).

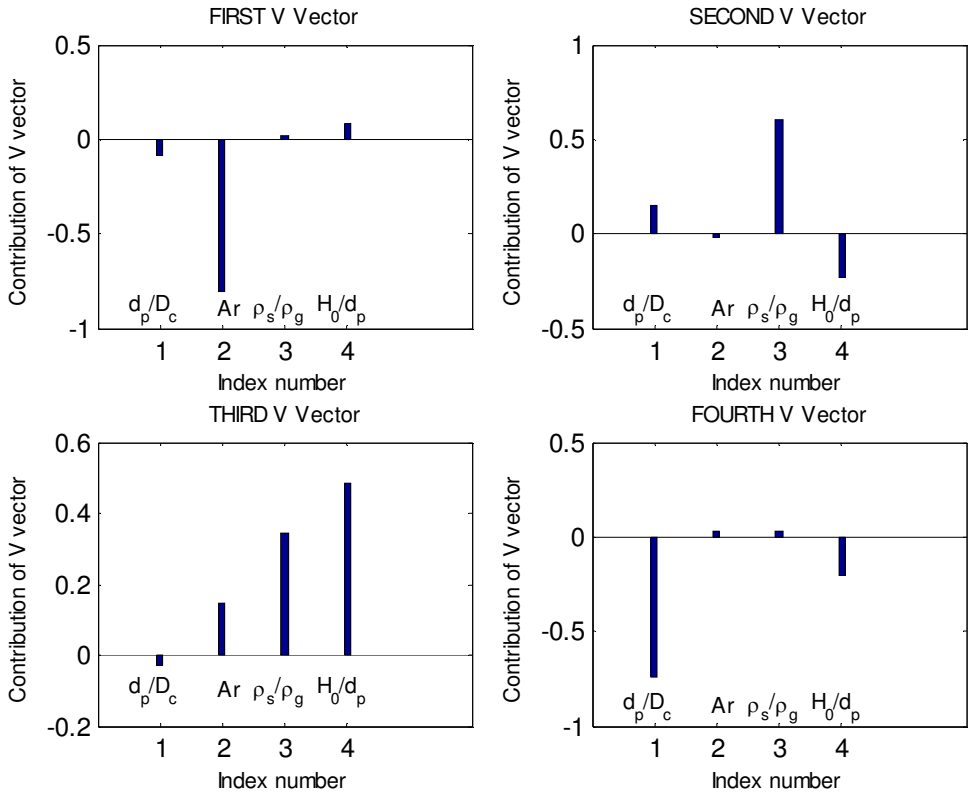

Figure 4.24: Relative make up of each principal component.

After PCR is carried out, the four regression coefficients in the 'V' frame are:

β_v =

-0.14
-0.06
0.70
-1.92

The regression model can be expressed by the following equation:

$$y = -0.14v_1 - 0.06v_2 + 0.70v_3 - 1.92v_4 \qquad 4.11$$

From analyzing the regression coefficients in the 'V' frame, it is seen that the βv_4 and βv_3 are the largest in magnitude and they are heavily weighted by d_p/D_c and, ρ_s/ρ_g and H_0/d_p, respectively, suggesting that coefficients for d_p/D_c and H_0/d_p will probably be bigger than the other two dimensionless variables, which is indeed so, as will be shown later. The factor ρ_s/ρ_g appearing as a heavy weight in v_3, with an associated βv_3 of 0.7 is countermined by its weight in v_4 although relative small; however it has an associated βv_4 of -1.92, a relatively large negative number.

Therefore the regression coefficient for ρ_s/ρ_g when cast in the original frame of reference appears small, again showing the confounding effect.

The regression coefficients, when expressed in the original variables are shown below.

β =

1.55	d_p/D_c
0.10	Ar
-0.01	ρ_s/ρ_g
1.33	H_0/d_p

Recall that β for Phase A is:

$\beta_{Phase\ A}$=

1.74	d_p/D_c
0.09	Ar
-0.06	ρ_s/ρ_g
1.33	H_0/d_p

The magnitudes of the first and fourth 'β' coefficients, as expressed in the original variables, are comparable to those obtained from the PCR model for results of experiments performed in Phase A. However the coefficient for ρ_s/ρ_g is much smaller than that for Phase A. The reason for this shift may be the confounding effect when the original variables have correlation among them. It is noted that unlike that for Phase A, the 3rd PC, v_3 in Phase B is weighted more heavily by x_3 and x_4, meaning that among the X data matrix, the x_3 and x_4 values are correlated. Thus, with the relatively larger coefficient of 1.33 associated with $x_4(d_p/D_c)$, the effect of x_3 is masked by x_4, leading to an apparent small regression coefficient for x_3. It is also noted that x_2(Ar) which appears heavily in v_1 has the smallest coefficient (0.1) reflecting its minor importance.

The R^2 value of 0.93 of this extended regression model indicates that the model is acceptable. Figure 4.25 shows the fairly good correlation between the fitted and experimental values of U_{ms}. The residual distribution is shown in Figure 4.26 and appears to be also acceptable since residuals are evenly distributed except for two outlier points.

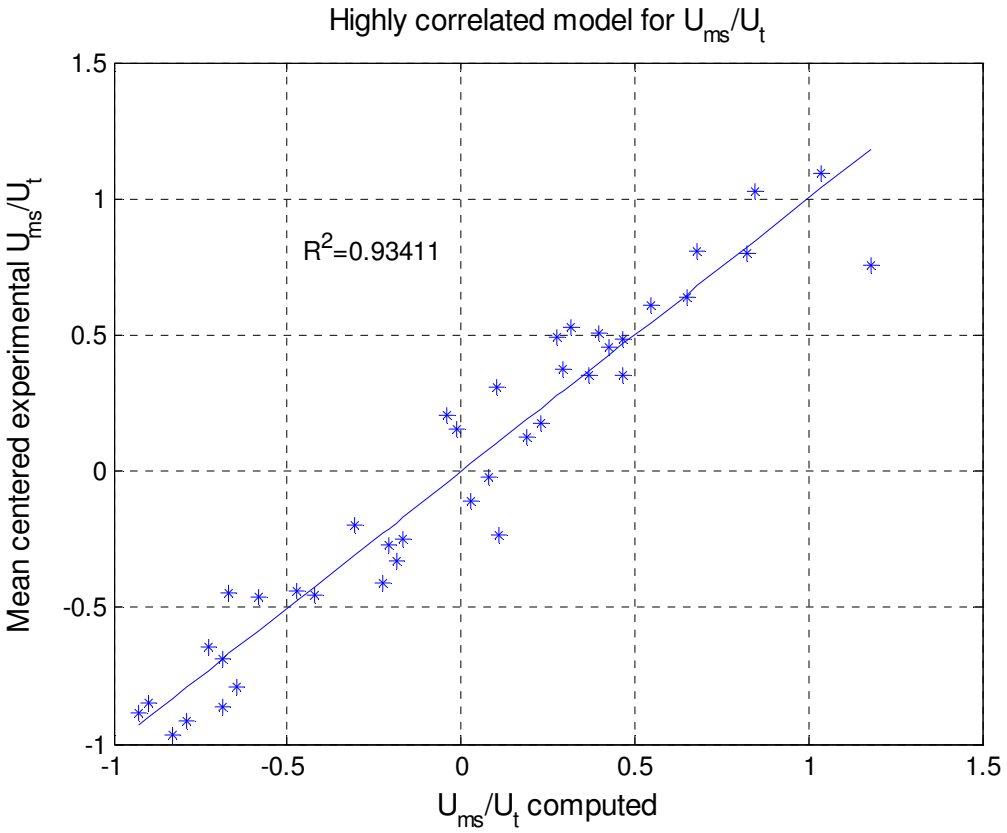

Figure 4.25: Measured versus predicted U_{ms}/U_t values for the 40 reference data points, showing the relatively little scattering between the measured and the predicted U_{ms}/U_t.

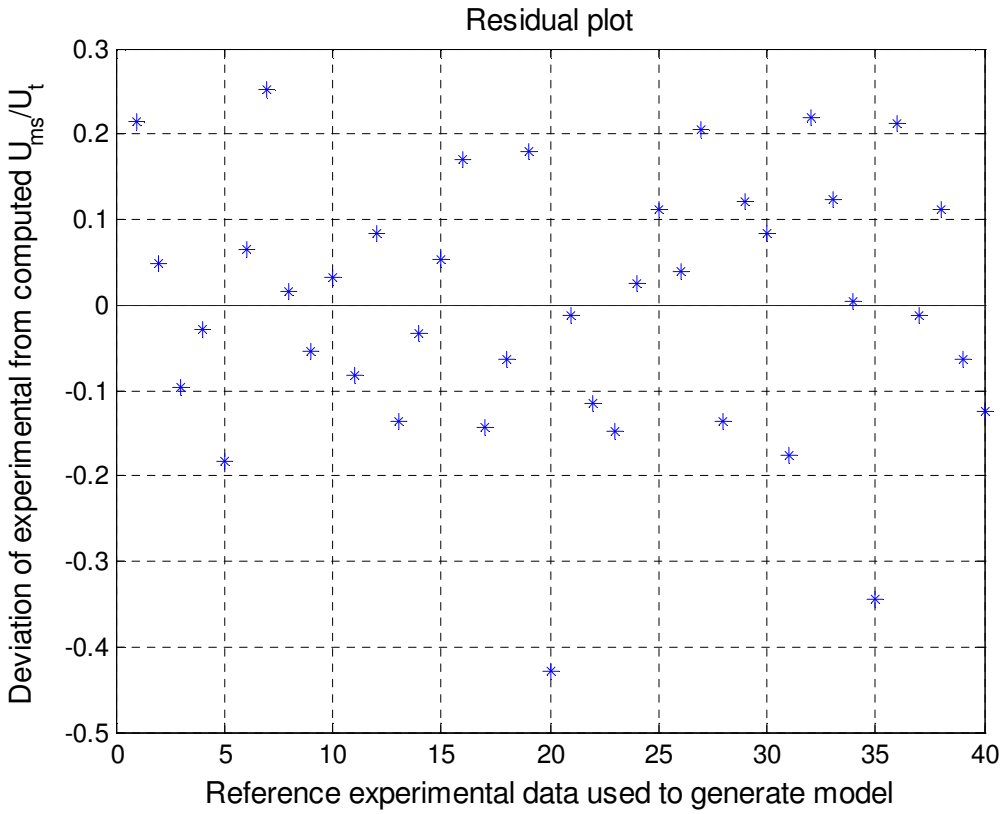

Figure 4.26: Fitting residuals from the PCR using the 40 reference sets of experimental data.

A validation process was carried out next using the developed regression model and results from a separate set of 35 experiments. Figure 4.27 shows the fairly good prediction by the regression model and the experimental U_{ms} values with R^2 equal to 92%. The residual distribution is shown in Figure 4.28 and appears comparable in magnitude to that for the reference data. Again, fairly good results obtained from the random division of the 75 total experiments into 40 reference sets to develop the model and 35 sets for validation, increases prediction confidence of this extended model

In summary, the highly correlated results with the developed extended model, obtained from the reference data, supports that $\frac{d_p}{D_c}, \frac{H_0}{d_p}$ are the more influential variables to determine U_{ms}, with Ar playing a minor role in determining U_{ms}, similar to those results obtained previously using a smaller data set from Phase A. $\frac{\rho_s}{\rho_g}$ appears to have some effect but its effect is masked by H_0/d_p, because they are shown to be correlated in the experimental set of data, as evidenced in v_3.

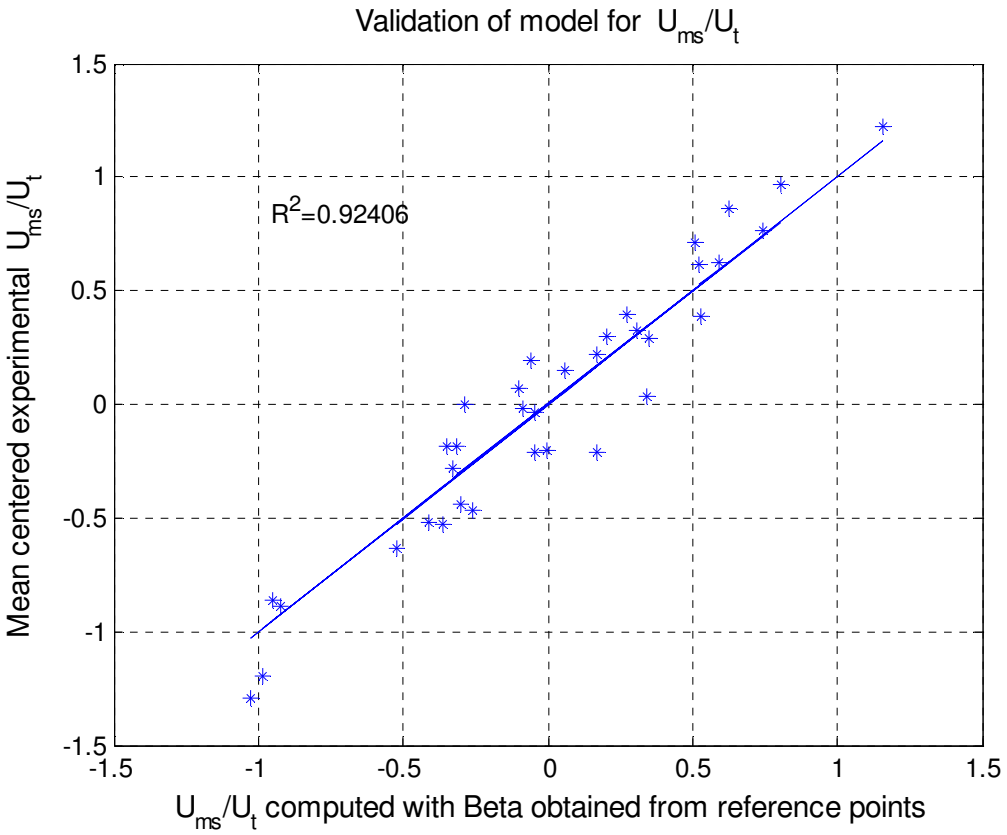

Figure 4.27: Measured versus predicted U_{ms} values from the regression model for the 35 validation sets.

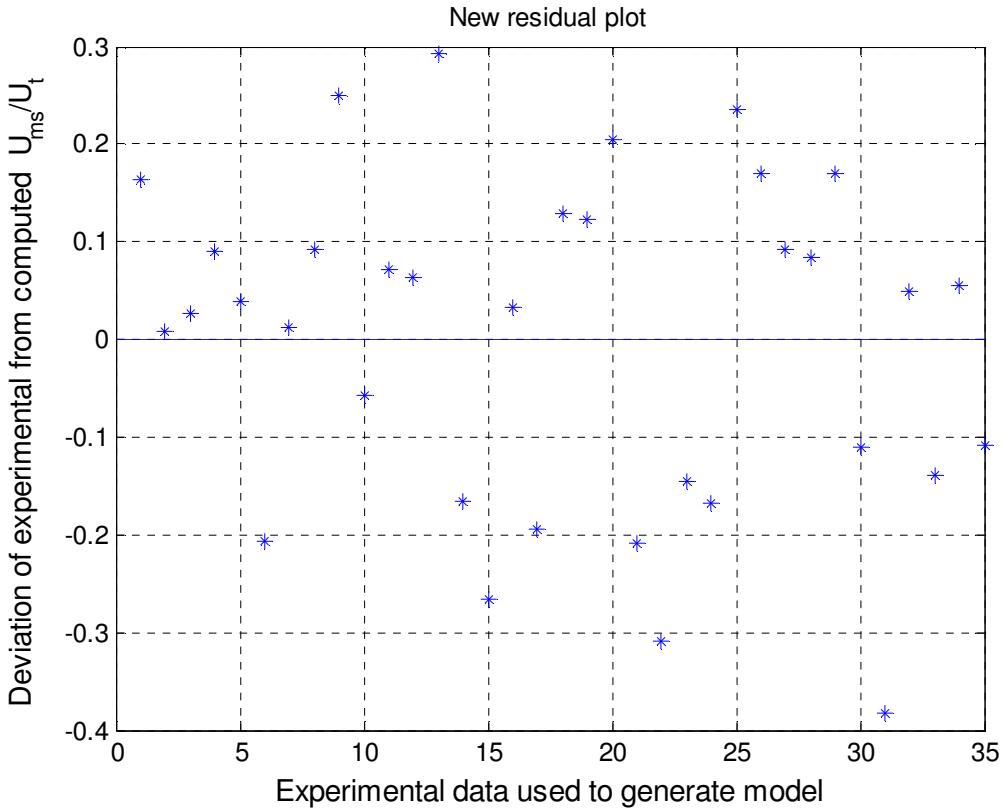

Figure 4.28: Fitting residuals from the PCR for the 35 validation sets.

Now that correlation equation has been developed for minimum spouting velocity, U_{ms}, for shallow bed, attention turns to modeling overall pressure drop across the bed, as well as for fountain height at superficial gas velocities beyond U_{ms}.

Since four different patterns of pressure drop behavior were identified beyond U_{ms}, and since three different spouting regimes were identified based on the variability of fountain heights (see Section 5.1), the following Sections present modeling results for bed pressure drop at minimum spouting condition and fountain height using selected data from the 75 experiments carried out in this investigation.

4.3. Developing regression model for ΔP_{ms}

Two regression models were developed using PCR for $Y=\Delta P_{ms}/(\rho_s H_0 g)$. The first model was developed with respect to five dimensionless variables of $\left\{\frac{d_p}{D_c}, \frac{\rho_s}{\rho_g}, \frac{H_0}{d_p}, \frac{U_{ms}^2}{g d_p}\right\}$ as suggested from published literature work on scaling factors [33] and to Ar. The second model was developed with respect to the most commonly used dimensionless variables in the reported literature on pressure drop correlations $\left(\mathrm{Re}_{ms}, \frac{H_0}{d_p}\right)$ (Table 1.3). Both models presented a good relationship between the original $\Delta P_{ms}/(\rho_s H_0 g)$ values and their corresponding fitted values; having R^2 values around 0.85. Regression model developed for ΔP_{ms} with respect to the five dimensionless variables will be presented first.

4.3.1 *Regression model developed for ΔP_{ms} with respect to five dimensionless variables*

The first regression model was developed using PCR for $Y=\Delta P_{ms}/(\rho_s H_0 g)$ with respect to the following five dimensionless variables $\left(\frac{d_p}{D_c}, Ar, \frac{\rho_s}{\rho_g}, \frac{H_0}{d_p}, \frac{U_{ms}^2}{g d_p}\right)$, where the last variable is Fr_{ms}, the Froude number at the minimum spouting velocity.

Results from experiments listed in Table 4.3 were randomly divided into two sets; 27 were used to develop the regression model for pressure drop at minimum spouting condition, and the rest were used to validate the developed model.

For the first model, the raw X data matrix with a dimension of 27×5, was normalized and mean centered. The resulting preprocessed X data was subjected to SVD and results are listed in **Table 4.8**.

Table 4.8: V vectors and S values

V =

-0.2484	0.0944	-0.3810	0.4849	0.7410
-0.7991	-0.4000	0.0079	-0.4422	0.0765
0.1287	0.5276	-0.4464	-0.6842	0.1942
0.1878	0.0307	0.7351	-0.2501	0.6007
-0.4979	0.7429	0.3393	0.1965	-0.2157

S =

8.6748	0	0	0	0
0	7.4749	0	0	0
0	0	4.0459	0	0
0	0	0	1.4824	0
0	0	0	0	0.3494

The variance contributed by each principal component is as follows.

d3 =

0.5023
0.3730
0.1093
0.0147
0.0008

Cumulative variance vector is shown below and it is shown as scree plot in Figure 4.29.

d4 =

0.5023
0.8753
0.9845
0.9992
1.0000

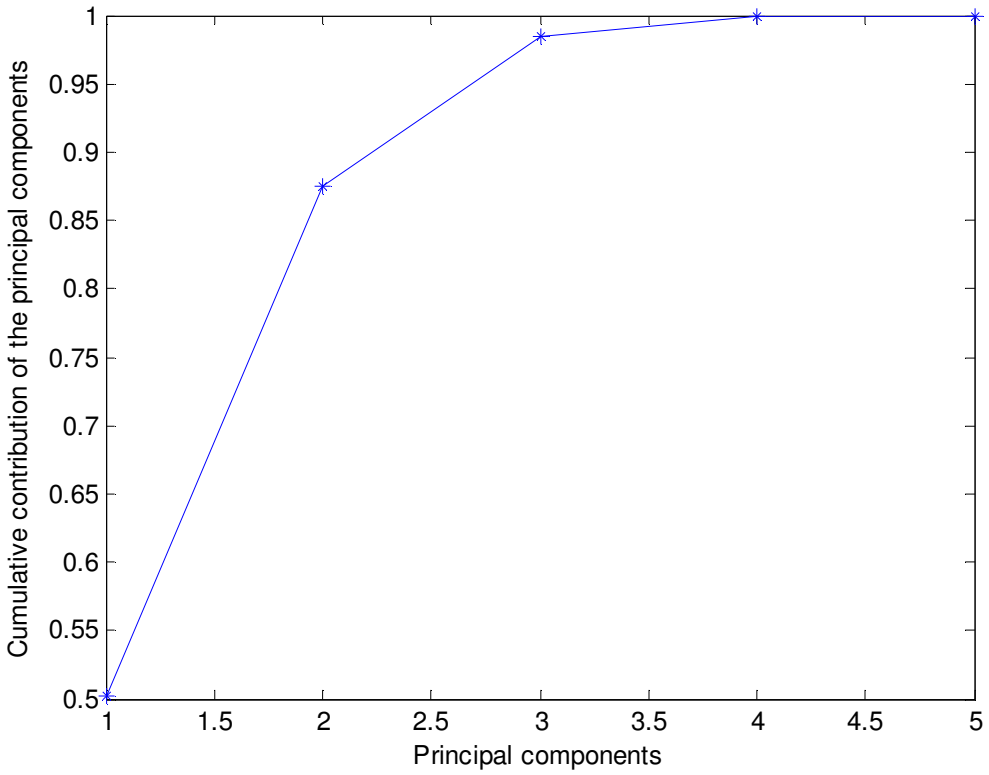

Figure 4.29: Scree plot showing the cumulative variance contributed by the principal components for pressure drop modeling.

From the scree plot it is seen that three principal components account for almost all the variance embedded in the X data matrix. Therefore, the PCR was developed using only the first three principal components. Including additional PC in the modeling did not improve the correlation.

From the relative make up of each principal component displayed in Figure 4.30, it can be seen that the first PC is heavily weighted by x_2 (Ar), the second PC is heavily weighted by x_5 (Fr_{ms}), the third PC is weighted by x_4 (H_0/d_p), the fourth PC is weighted by x_3 (ρ_s/ρ_g) and the fifth PC is weighted by x_1 (d_p/D_c), showing almost a decoupled distribution for the five original variables. Based on the variance contributed by each principal component, it is seen that Ar, Fr and H_0/d_p include the overall variance captured by the X data matrix.

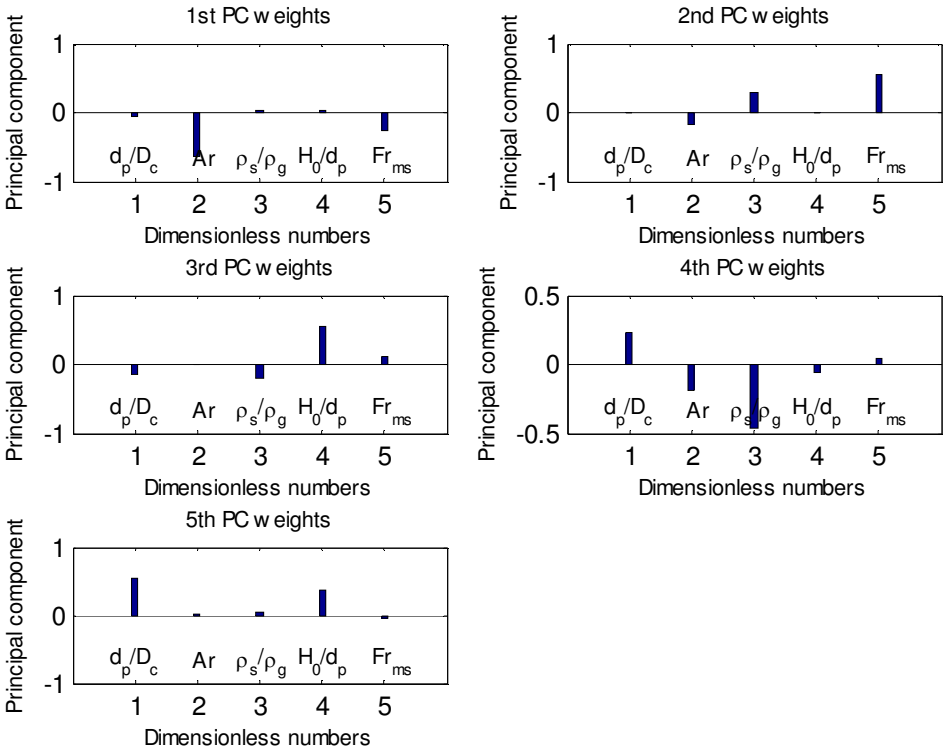

Figure 4.30: Relative make up of each principal component.

The three regression coefficients in the "V" frame are:

β_v =
0.1160
0.0186
-0.0737

So the regression model can be expressed by the following equation:

$$y = 0.116v_1 + 0.018v_2 - 0.073v_3 \qquad 4.12$$

From the scree plot, it can be seen that v_1, v_2 and v_3 are much heavily weighted by Ar, Fr_{ms} (i.e. U_{ms}^2/gd_p) and H_0/d_p respectively, suggesting that these variables are the most influential in defining $\Delta P_{ms}/(\rho_s H_0 g)$. Notice that when the regression coefficients in the 'v' frame are transformed back to the original frame of reference, the regression coefficient associated with Ar remains the highest of all variables.

As was mentioned in the last section, regression coefficients in the original variables are harder to interpret since the experimental vector values of the original variables are not independent of each other. Also, notice that the factor ρ_s/ρ_g appearing in v_2 has a weight of 0.53 with a βv_2 of 0.0186, and appearing in v_1 with a small weight of 0.13 but has the largest associated βv_1 of 0.11, and with a weight of 0.45 in v_3 associated with β_{v3} value of 0.07 contributes to the overall importance of ρ_s/ρ_g, resulting in a non-trivial regression coefficient of 0.06 for ρ_s/ρ_g when it is cast in the original frame of reference, showing a confounding effect among Fr_{ms}, Ar , H_0/d_p and ρ_s/ρ_g. Therefore, it appears that Ar, H_0/d_p and Fr_{ms} are the more influential variables in defining $\Delta P_{ms}/(\rho_s H_0 g)$ with d_p/D_c exerting very little influence over ΔP_{ms}.

The regression coefficients, when expressed in the original variables are shown below.

β =

0.0010	d_p/D_c
-0.1007	Ar
0.0577	ρ_s/ρ_g
-0.0318	H_0/d_p
-0.0689	Fr_{ms}

Figure 4.31 shows the relationship between the original $\Delta P_{ms}/(\rho_s H_0 g)$ values and their corresponding fitted values by the PCR model. Although R^2 value of 0.85 is not as good as the R^2 values for the developed U_{ms}, when the model was validated using the validation data, an R^2 value of 0.81 was obtained (see Figure 4.33). In addition, the residual distribution for the reference data used to develop the regression model (see Figure 4.32) appear to be acceptable, since residuals appear to be evenly distributed and comparable in magnitude. However, plot for validation data (Figure 4.33) appear to show some curvature with the validation data in the middle range of $\Delta P/(\rho_s H_0 g)$ values. This phenomenon may warrant further investigation for the future. Also, the residuals for the validation data appear to be evenly distributed and comparable in magnitude (see Figure 4.34).

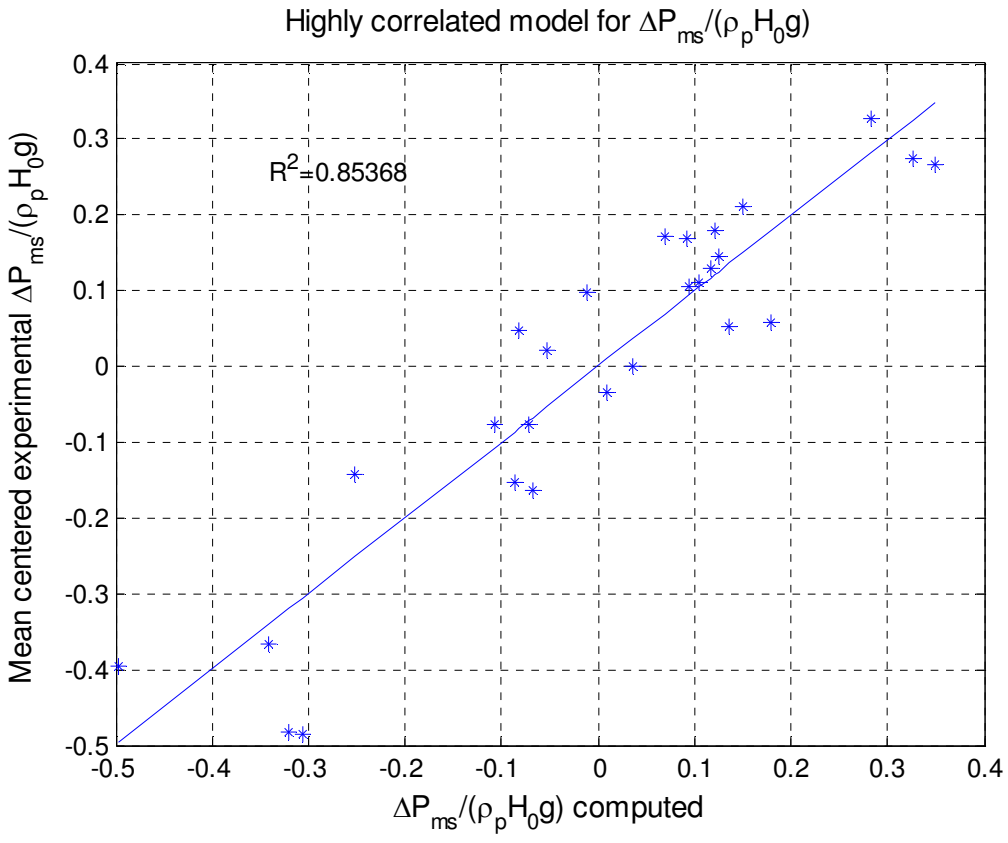

Figure 4.31: Measured versus predicted $\Delta P_{ms}/(\rho_s H_0 g)$ values from the regression model showing the relatively little scattering between the measured and the predicted $\Delta P_{ms}/(\rho_s H_0 g)$ values using 27 sets of experimental data.

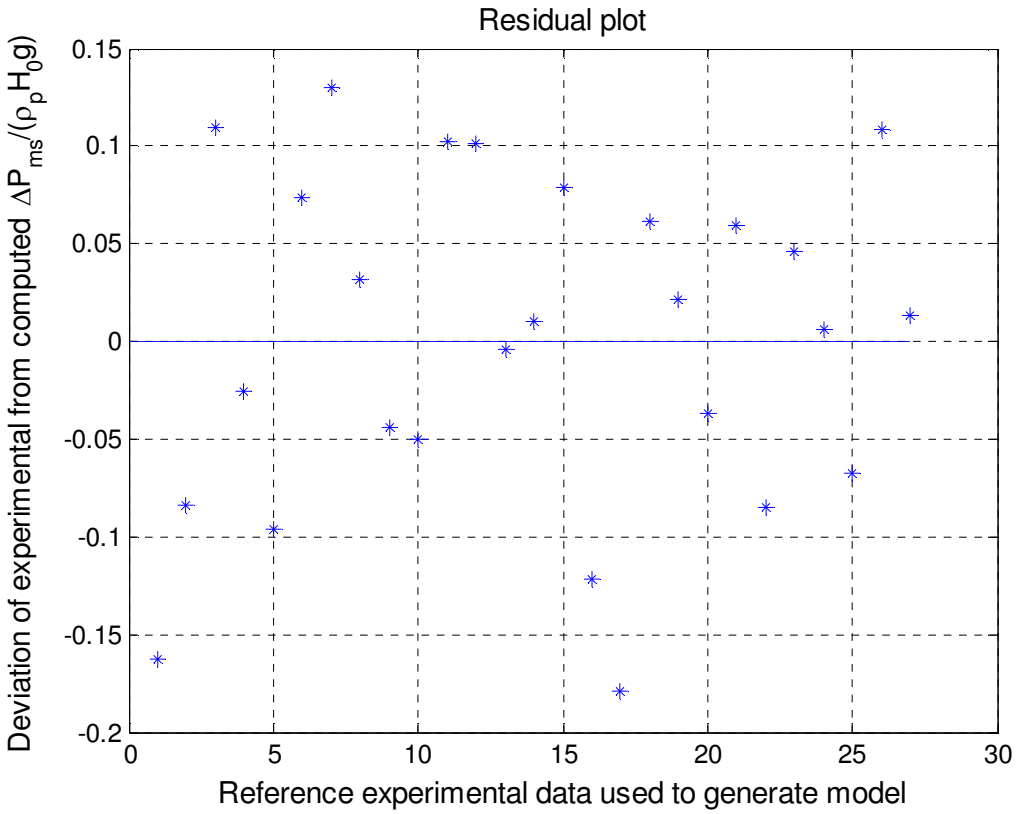

Figure 4.32: Fitting residuals from the PCR using the 27 reference sets of experimental data.

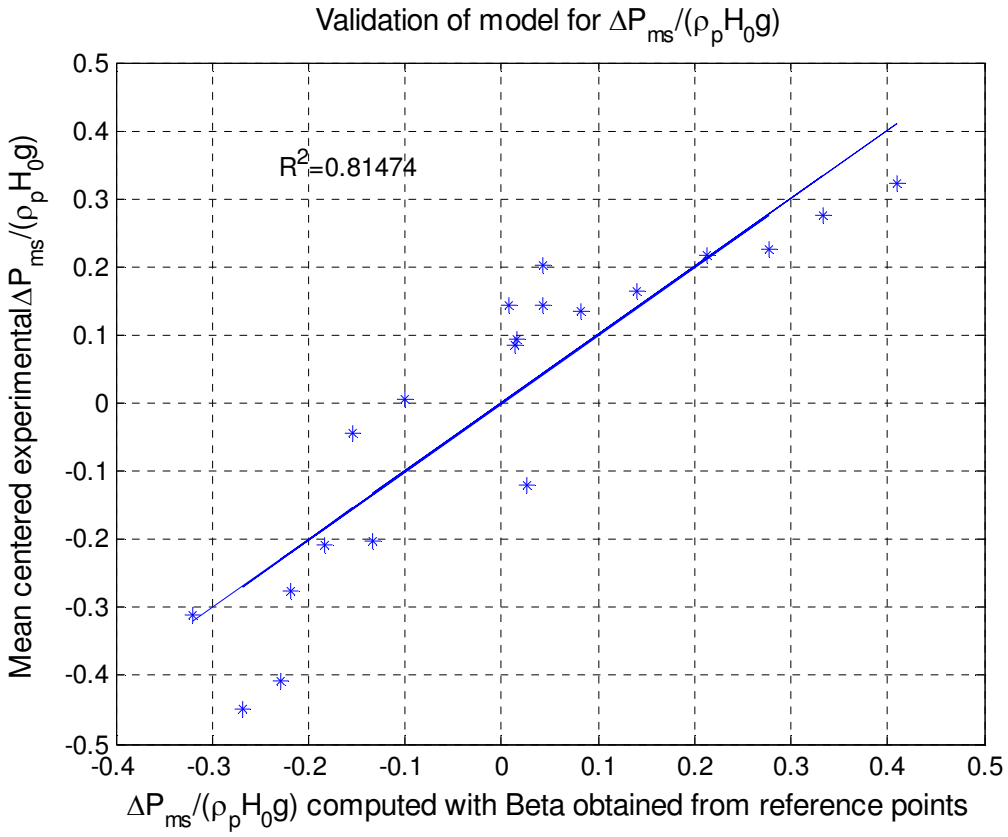

Figure 4.33: Measured versus predicted $\Delta P_{ms}/(\rho_s H_0 g)$ values from the regression model for the 20 validation sets.

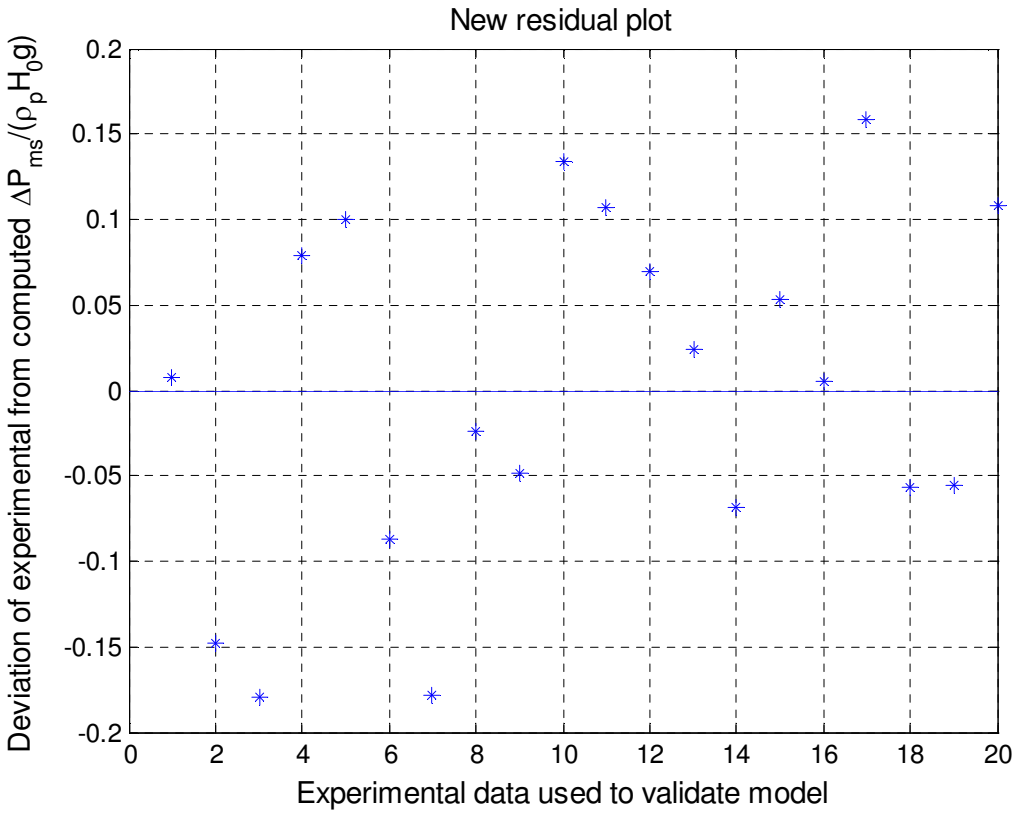

Figure 4.34: Fitting residuals from the PCR for the 20 validation sets.

In summary, modeling results suggest that Ar, Fr_{ms} and H_0/d_p are relevant in determining $\Delta P_{ms}/(\rho_s H_0 g)$. Note that d_p/D_c and ρ_s/ρ_g by themselves appear to have very minor, if any, effect in determining $\Delta P_{ms}/(\rho_s H_0 g)$. However they still exert their influence through the Ar variable since it is expanded as:

$$Ar = \frac{d_p^3 \rho_g \left(\rho_s - \rho_g\right) g}{\mu^2} \qquad 4.13$$

The next section presents modeling results of bed pressure drop with respect to the most two common variables used in reported literature correlations of bed pressure drop (see Table 1.3) which are Re_{ms} and H_0/d_p, where Re_{ms} is defined as follows:

$$\mathrm{Re}_{ms} = \frac{d_p \rho_g U_{ms}}{\mu} \qquad 4.14$$

4.3.2 *Reduced regression model developed for ΔP_{ms} with respect to two dimensionless variables*

This regression model was developed using PCR for $Y=\Delta P_{ms}/(\rho_s H_0 g)$ with respect to just two dimensionless variables $\left\{\mathrm{Re}_{ms}, \frac{H_0}{d_p}\right\}$. Results from the same set of experiments considered in developing the previous model were used to develop this new model. The resulting preprocessed X, now of dimension of 27×2 was subjected to SVD and results are listed in **Table 4.9**.

Table 4.9: V vectors and S values

V =

-0.9838 0.1792
0.1792 0.9838

S =

6.5133 0
0 3.2734

The variance contributed by each principal component is as follows:

d3 =
0.7984
0.2016

Cumulative variance vector is shown below.

d4 =
0.7984
1.0000

From the relative make up of each principal component, it can be seen that the first column is heavily weighted by x_1 (Re_{ms}) and the second column is heavily weighted by x_2 (H_0/d_p), showing a decoupled distribution of values between variables.

The regression coefficients in the "v" frame are:

β_v =
0.1623
-0.0361

So the regression model can be expressed by the following equation.

$$y = 0.16v_1 - 0.036v_2 \qquad 4.15$$

It can be seen that β_{v1} is much higher than the second coefficient and since v_1 is heavily weighted by Re_{ms}, it is suggested that Re_{ms} is the more influential variable in defining $\Delta P_{ms}/(\rho_s H_0 g)$. Notice that Re_{ms} is defined as

$$\mathrm{Re}_{ms} = \frac{\rho_g d_p U_{ms}}{\mu_g} \qquad 4.16$$

where U_{ms} was found to be previously a function of $\left\{\frac{d_p}{D_c}, Ar, \frac{\rho_s}{\rho_g}, \frac{H_0}{d_p}\right\}$; a model that has been derived in Section 5.2.

The regression coefficients, when expressed in the original variables are shown below.

β =
-0.1661 Re_{ms}
-0.0064 H_0/d_p

Even though regression coefficient for H_0/d_p is relatively small (-0.0064), it is to be interpreted with caution, because the dimensionless ΔP_{ms} term has H_0 in the denominator as in $\Delta P_{ms}/(\rho_s H_0 g)$. The net effect of H_0 on ΔP_{ms} can be seen more clearly by multiplying both sides of the model by H_0, to give a ($H_0^{0.993}$) dependence for ΔP_{ms}.

Figure 4.35 and Figure 4.37 show the relationship between the original $\Delta P_{ms}/(\rho_s H_0 g)$ values and their corresponding fitted values by the regression model for the reference and the validation data sets respectively. The R^2 values, 0.86 and 0.82 of the PCR model for the reference and validation data are comparable to those obtained in previous section, R^2=0.85 and R^2=0.81, respectively; indicating that both regression models developed in this section are acceptably good. Note the similarity in the fitting pattern for both the reference and the validation data from the previous section when five dimensionless variables were used as the regression variables (compare Figure 4.36 to Figure 4.32; Figure 4.37 to Figure 4.33). The similarity between the fit by the two models suggest that the variables of U_{ms}, H_0/d_p, along with ρ_s/ρ_g correlate with the pressure drop in a similar manner, reinforcing the tentative conclusion that Ar, U_{ms} and H_0/d_p are influential in determining the bed pressure drop at minimum spouting condition drawn from the first modeling

effort. In addition the residual distributions for the reference data and validation data appear to be evenly distributed and comparable in magnitude too, as can be seen in Figure 4.36 and Figure 4.38.

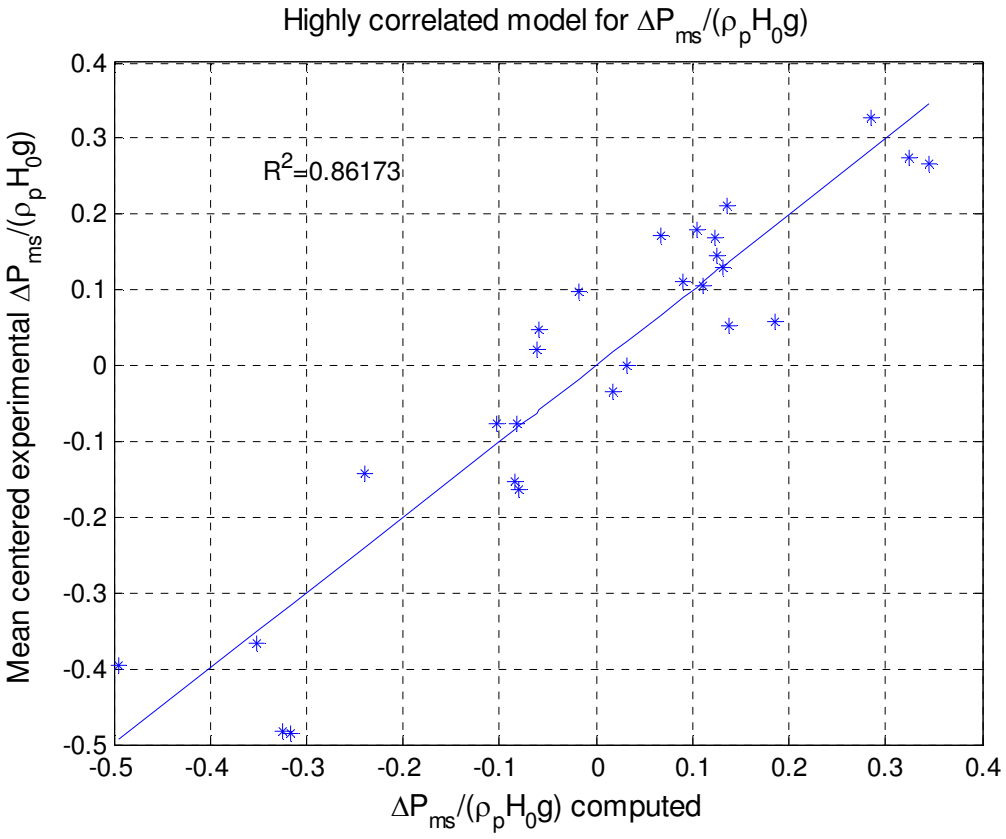

Figure 4.35: Measured versus predicted $\Delta P_{ms}/(\rho_s H_0 g)$ values from the regression model showing the relatively little scattering between the measured and the predicted $\Delta P/(\rho_s H_0 g)$ values using 27 sets of experimental data.

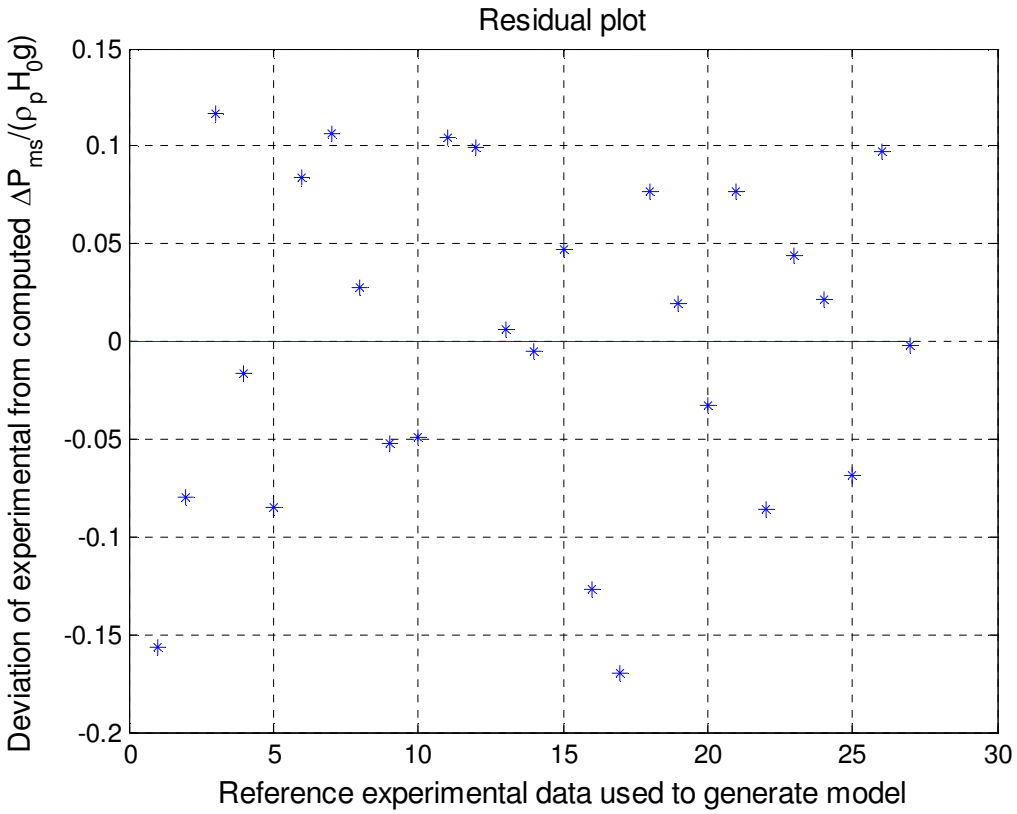

Figure 4.36: Fitting residuals from the PCR using the 27 reference sets of experimental data.

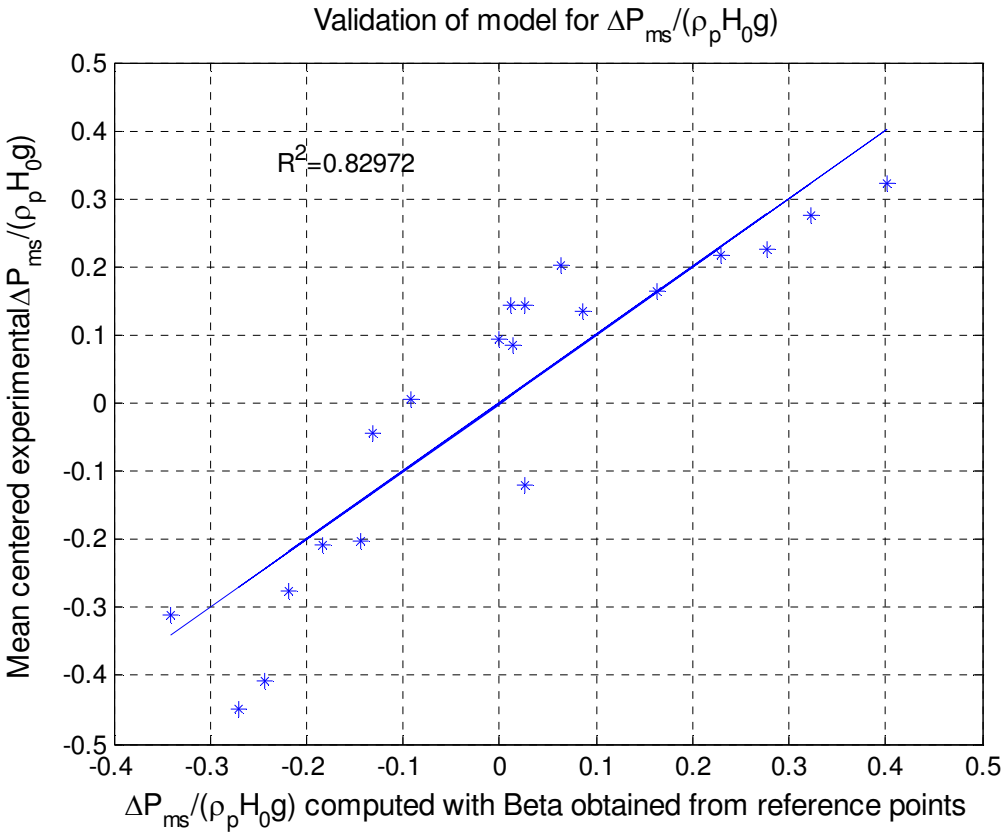

Figure 4.37: Measured versus predicted $\Delta P_{ms}/(\rho_s H_0 g)$ values from the regression model for the 20 validation sets.

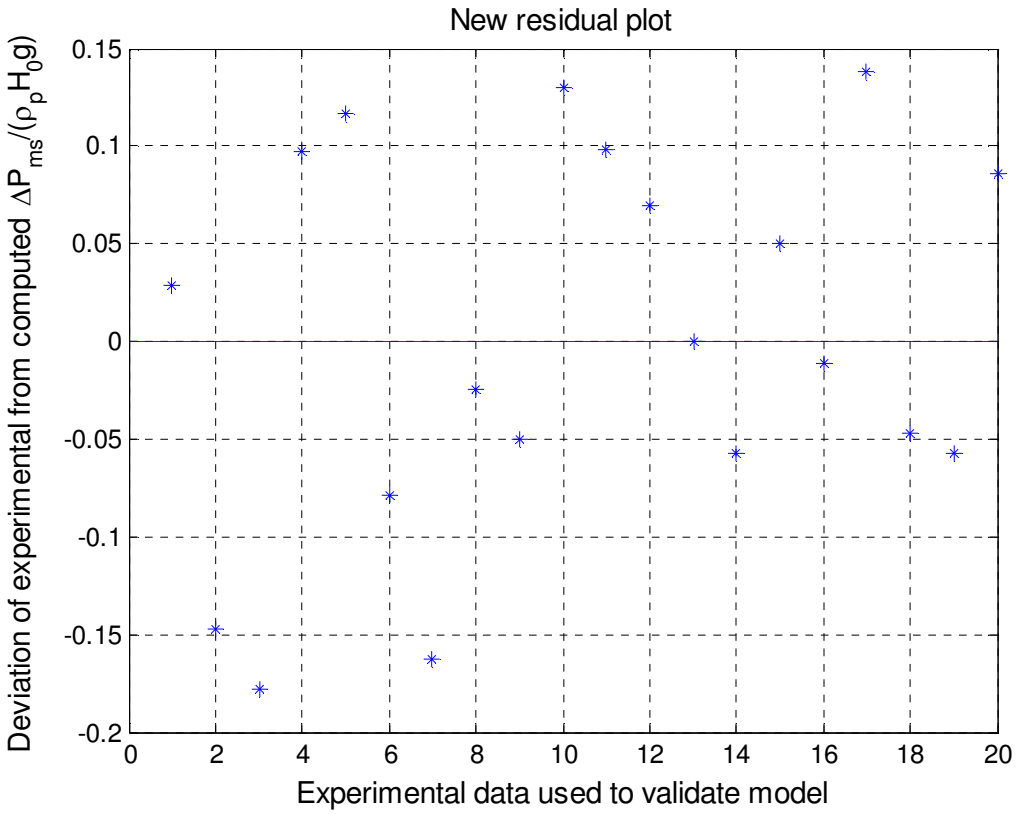

Figure 4.38: Fitting residuals from the PCR for the 20 validation sets.

In summary, modeling using two different sets of predictor variables suggests that U_{ms}, H_0/d_p and ρ_s/ρ_g, through Ar, are the variables that determine $\Delta P_{ms}/(\rho_s H_0 g)$.

The next section presents modeling results for fountain height using selected data from the 75 experiments carried out in this investigation (see Section 5.1). Since the fountain height was found to be directly proportional to the superficial gas velocity (U), two spouting velocities beyond U_{ms} were chosen to be included in the data set used for regression. The two values chosen were 1.2 and 1.8 U/U_{ms}.

4.4. Developing regression model for H_f using four dimensionless variables

Since fountain height was observed in the experiments performed in this investigation to vary linearly with gas flow (refer to appendix A), fountain height values were first fitted by a linear model of the form of y=mx+b, where 'y' represented the fountain height at different values of U/U_{ms} <2 and x is the U/U_{ms} value. The dimensionless variable 'Y' is determined by the values of H_f scaled by maximum value of H_f of the set of experiments in question.

Frequently, experimental observations showed a small but nonzero fountain height at the determined minimum spouting velocity (see Figure 2.5). This phenomenon was considered an artifact, since theoretically, the fountain height should be very small or zero at the minimum spouting condition. As a result, to correct for experimental uncertainty and possible U_{ms} measurements errors, the fountain height at U_{ms} was subtracted from all subsequent fountain height values at values of $U/U_{ms} \geq 1$. Then the corrected fountain height values for the chosen experiments were then used in the fountain height regression study.

A regression model was developed using PCR for fountain height with respect to four chosen dimensionless variables 'X' shown below, similar to those used in reported literature for fountain height correlations (Table 1.4).

$$X = \left[\frac{d_p}{D_c}, Ar, \frac{H_0}{d_p}, U \Big/ U_{ms} \right] \qquad 4.17$$

Results of a total of the 64 experiments listed in Table 4.4 were used to develop and validate the regression model. These experiments were randomly divided into two sets; the first set of 33 experiments was used to generate the PCR model, and the second set consists the rest of the experiments (31 sets) was used for validation. Both sets included values of H_f at 1.2 and 1.8 U/U_{ms}; resulting in 66 data points to develop the regression model and 62 data points for validation.

The following table presents the results from applying a SVD factorization on the normalized and mean centered 66×4 data matrix 'X'. Pretreatment of data is described in Section 3.2.1.

Table 4.10: V vectors and S values

V =

-0.2793	0.4836	0.8295	0
-0.9200	-0.3820	-0.0871	-0.0000
0.2748	-0.7875	0.5517	-0.0000
-0.0000	-0.0000	0.0000	1.0000

S =

15.1738	0	0	0
0	4.9701	0	0
0	0	1.6907	0
0	0	0	1.6470

The variance contributed by each principal component is as follows:

d3 =
0.8838
0.0948
0.0110
0.0104

Cumulative variance vector is shown below and it is shown as scree plot in Figure 4.39.

d4 =
0.8838
0.9786
0.9896
1.0000

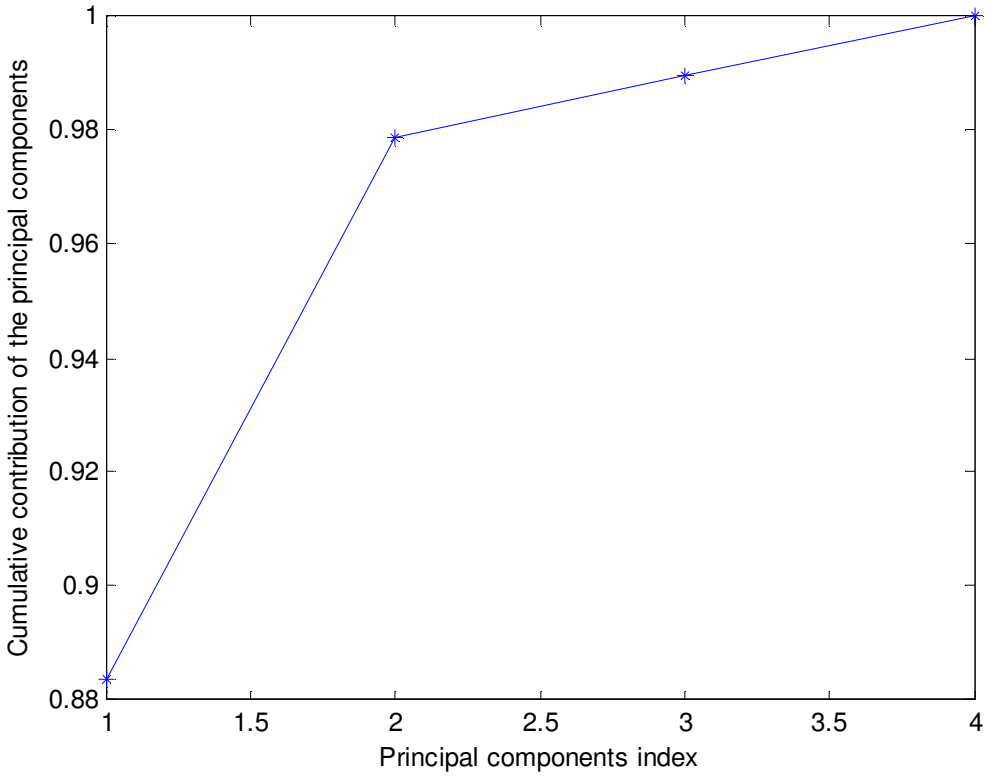

Figure 4.39: Scree plot showing the cumulative variance contributed by the principal components.

As can be seen in Figure 4.40, the weightings of the four principal components are almost decoupled, in that they are weighted respectively by Ar, H_0/d_p, d_p/D_c and U/U_{ms}. Note that the last principal component is entirely weighted by U/U_{ms} alone, and its presence in the first three components is practically zero. Since the fountain height is linearly dependent on U/U_{ms} when everything else is held constant, all four principal components (of the full data set content) must be retained for modeling, i.e. the fourth PC must be retained also.

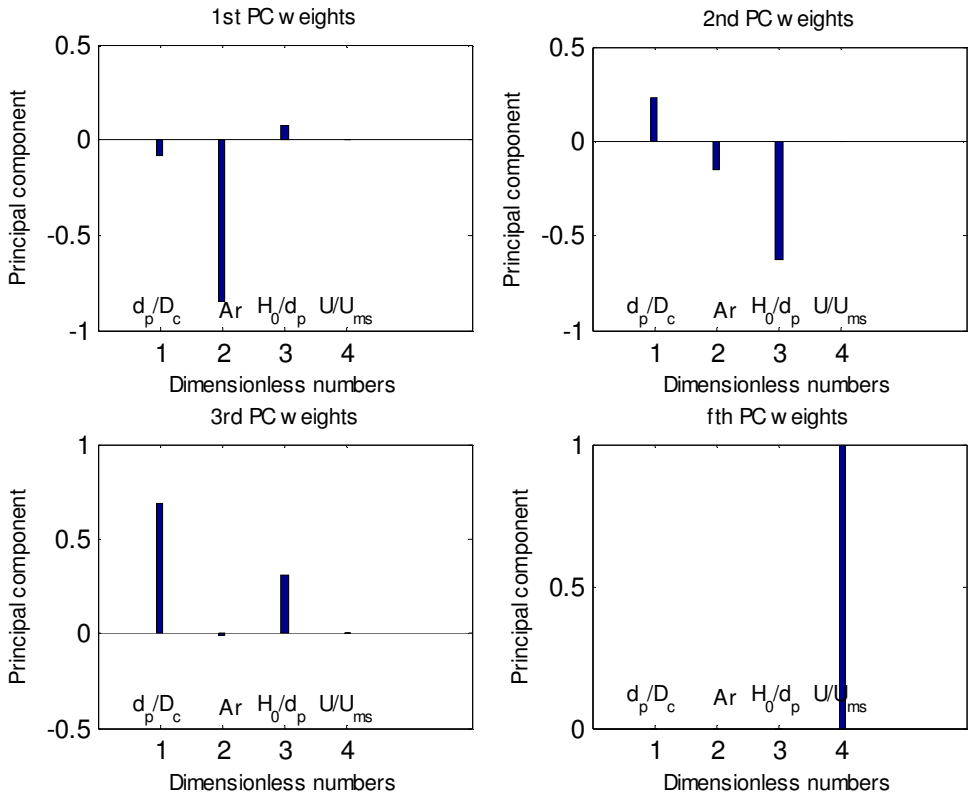

Figure 4.40: Relative make up of each principal component.

The four regression coefficients in the "v" frame are:

β_v =
-0.0640
-0.6160
1.1589
3.4190

So the regression model can be expressed by the following equation.

$$y = -0.06v_1 - 0.62v_2 + 1.16v_3 + 3.42v_4 \qquad 4.18$$

It can be seen that the coefficients βv_4, βv_3 and βv_2 are much higher than the first coefficient. Since v_4, v_3 and v_2 are much heavily weighted by U/U_{ms}, d_p/D_c and H_0/d_p respectively suggesting that these variables are the more influential in determining fountain height. Ar appears to have very little influence on H_f.

The regression coefficients, when expressed in the original variables are shown below.

β =

0.6813	d_p/D_c
0.1933	Ar
1.1068	H_0/d_p
3.4190	U/U_{ms}

Note that regression coefficient for U/U_{ms} is the same in both frames of reference, because the fourth principal component is equivalent to U/U_{ms}. The 'β' coefficients, as expressed in the original variables suggest that U/U_{ms} (3.41) is the most influential factor in determining H_f followed by H_0/d_p (1.10) and d_p/D_c (0.68), and that Ar (0.19) is the least influential.

The comparison between the original H_f values to their corresponding fitted values (on the regression line) by the PCR model is shown in Figure 4.41 with an R^2 value of 0.87. The residual distribution shown in Figure 4.42 appears acceptable.

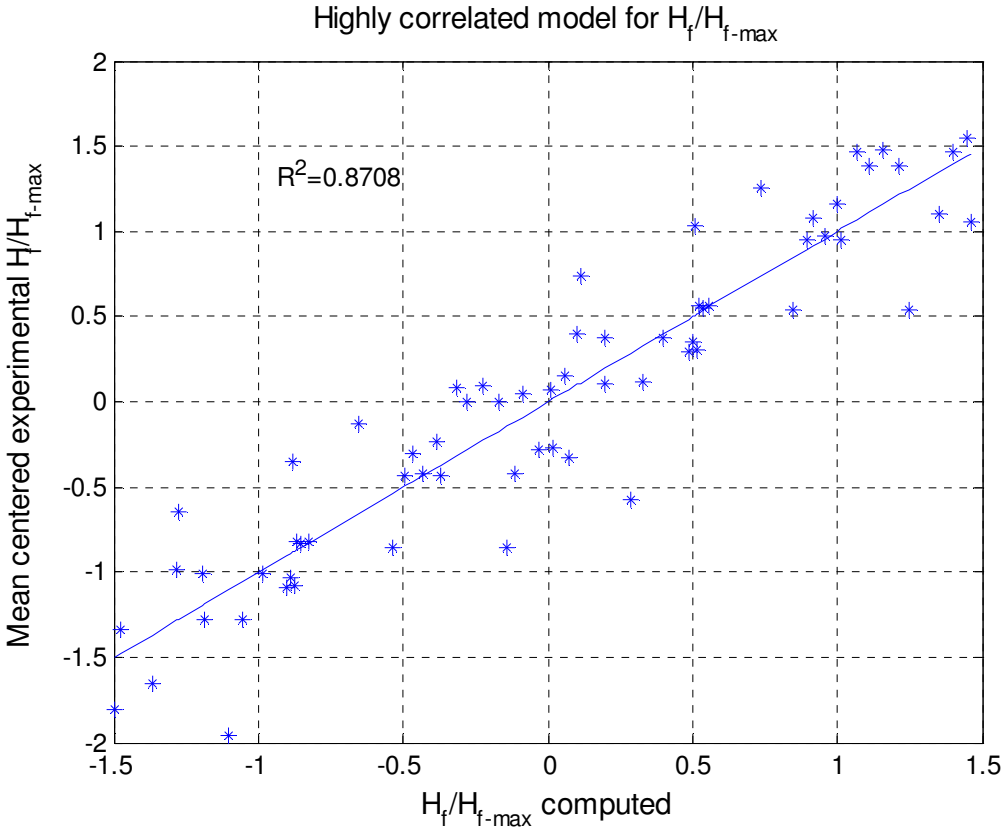

Figure 4.41: Measured versus predicted H_f/H_{f_max} values from the regression model showing the scattering between the measured and the predicted H_f/H_{f_max} values using 66 data points.

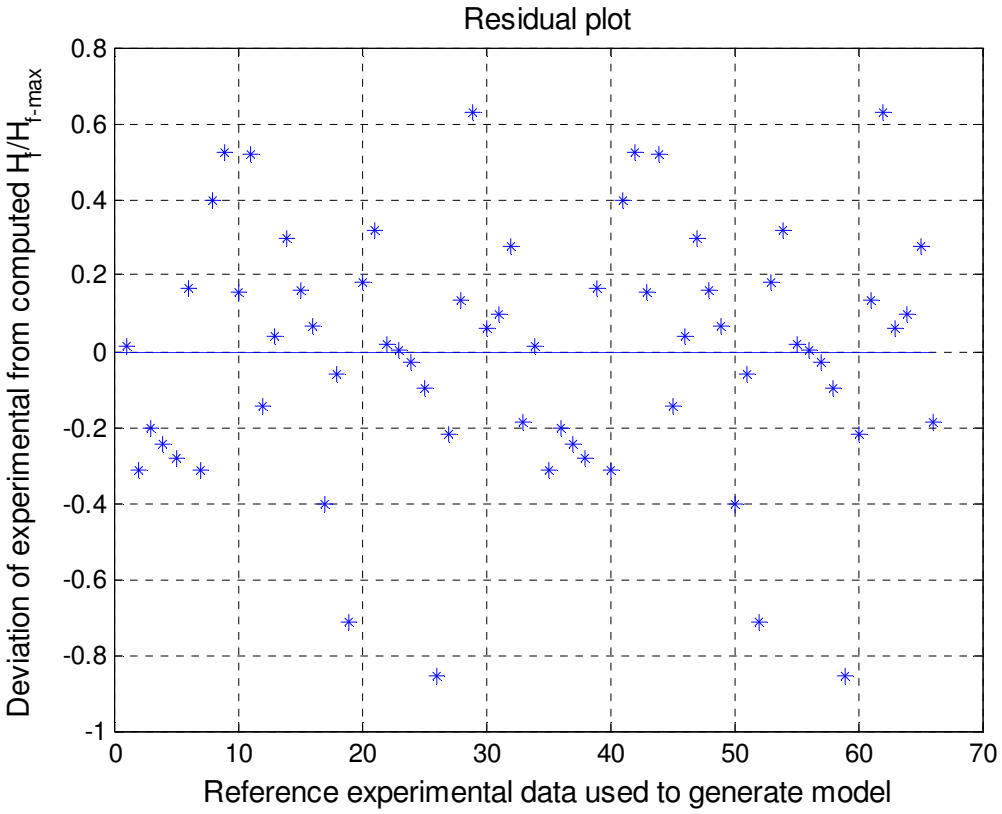

Figure 4.42: Fitting residuals from the PCR model using the 66 reference data points.

In addition, H_f fitting of validation values result in an R^2 value of 0.88 comparable to the R^2 obtained from the reference regression model. Figure 4.43 shows the scattering between the measured and the predicted values of H_f for validation data. The residual plot (Figure 4.44) appears to be acceptable also since residuals appear to be evenly distributed and comparable in magnitude.

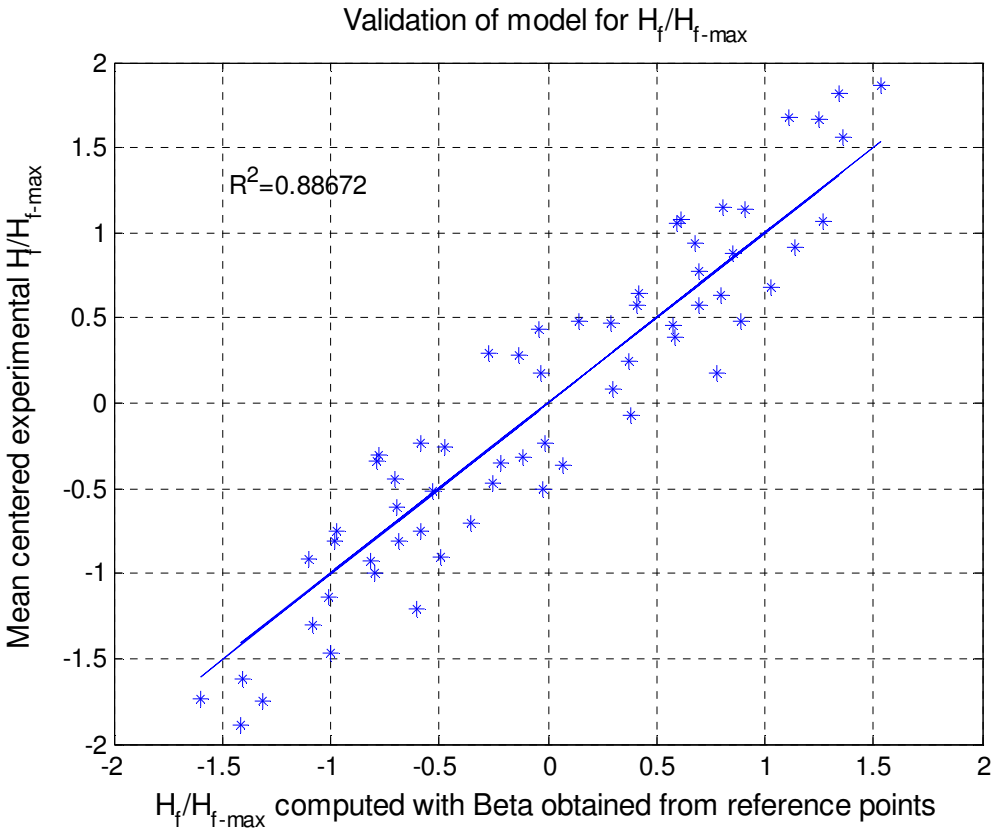

Figure 4.43: Measured versus predicted H_f/H_{f_max} values from the regression model for the 62 validation data points.

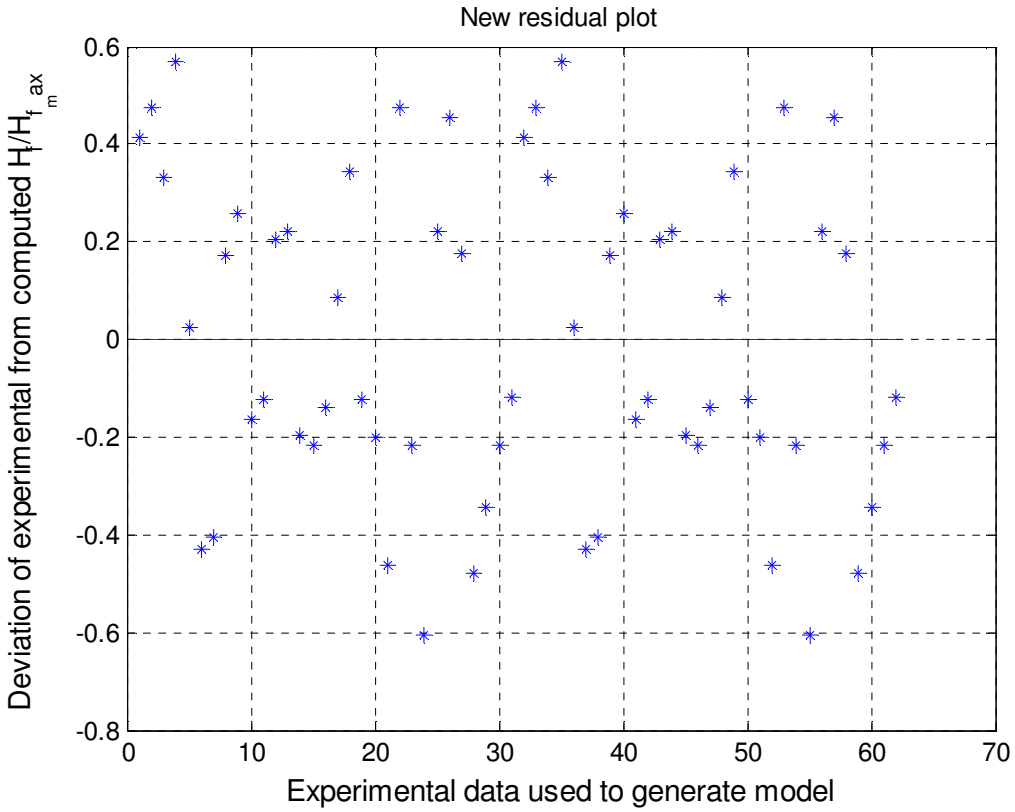

Figure 4.44: Fitting residuals from the PCR for the 62 validation data points.

In summary, modeling results suggest U/U_{ms}, H_0/d_p, and to some extent, d_p/D_c, are the variables that determine fountain height. Archimedes number seems to have the weakest effect in determining H_f. Note that the H_{f_max} used to normalize the H_f variable has a value of '0.1193m'. This number will be rolled into the calculation of the intercept, β_0.

The next section presents the final correlations equations obtained for U_{ms}, ΔP_{ms} and H_f expressed in the form of the original nonlinear equation:

$$\tilde{y} = \tilde{\beta}_0 \tilde{x}_1^{\beta_1} \tilde{x}_2^{\beta_2} .... \tilde{x}_k^{\beta_k} \qquad 4.19$$

where $\tilde{y}$ represents the corresponding dimensionless variable for minimum spouting velocity, pressure drop and fountain height, and $\{\tilde{x}_i\}_{i=1}^{k}$ represents the set of dimensionless variables used to develop each regression model (see Sections 4.2-4.4). $\{\beta_i\}_{i=1}^{k}$ represents the set of regression coefficients expressed in the original frame of reference, and $\tilde{\beta}_0$ represents a constant, the

intercept in the linearized version of Equation 3.1. $\tilde{\beta}_0$ is computed as described in Section 3.2.3. Notice that, since data was normalized and mean centered as described in Section 3.2.1, the procedure to obtain $\tilde{\beta}_0$ has incorporated into it all the maximum and mean column values of the x and y used for normalization (see Section 3.2.3).

4.5. Final hydrodynamic correlations models for shallow spouted bed for dense particles

This section presents the final models obtained for U_{ms}, ΔP_{ms} and H_f and a discussion of the general trends between the operating conditions and the measured response variable.
Comparisons with the most relevant correlations available in the literature are presented which illustrates the advances made by this research in the ability to predict the behavior of shallow spouted beds with dense particles.

4.5.1 *Minimum spouting velocity (U_{ms})*

Two regression models were developed to correlate minimum spouting velocity with four significant dimensionless variables. Both models include data for all bed pressure drop profiles defined in Section 4.1.2 and all spouting regimes defined in Section 4.1.3. The first model corresponds to the exploratory PCR done using the results of experiments performed at ambient temperature and pressure in Phase A, which only includes the following variation of parameters; column diameter (50 and 80 mm bed), static bed height (H_0/D_c=0.42, 0.67 and 1), particle diameter (500 and 1000 µm), gas density (0.17 and 1.18 kg/m^3) and particle density (3880, 6000 and 7600 kg/m^3). The second model encompasses a bigger range of variation by adding a 150 mm diameter bed and 2000 µm diameter particles. It is recommended that the second model be used for prediction since it is developed using a wider variation of column size and particle size.

The first exploratory correlation model is expressed as follows

$$\frac{U_{ms}}{U_t} = 0.1476\left(\frac{d_p}{D_c}\right)^{1.74}(Ar)^{0.09}\left(\frac{\rho_s}{\rho_g}\right)^{-0.06}\left(\frac{H_0}{d_p}\right)^{1.33} \qquad 4.20$$

where the terminal velocity is given by

$$U_t = \sqrt{\frac{4d_p(\rho_s - \rho_g)g}{3\rho_g C_D}} \qquad 4.21$$

The R^2 value for this model is 94% and the most important dimensionless factors that define minimum spouting velocity are d_p/D_c, H_0/d_p and ρ_s/ρ_g. Ar was found to have very little influence in U_{ms}, even though it was found to be most varying in the set of experiments in both Phases.

A second and final correlation for U_{ms} was developed using PCR with respect to the same four dimensionless variables but using results of the experiments performed in Phase B which include the biggest diameter bed (150 mm) and the biggest particle diameter (2000 μm). This expanded model is expressed by the following equation:

$$\frac{U_{ms}}{U_t} = 0.0352\left(\frac{d_p}{D_c}\right)^{1.55}(Ar)^{0.1}\left(\frac{\rho_s}{\rho_g}\right)^{-0.01}\left(\frac{H_0}{d_p}\right)^{1.33} \qquad 4.22$$

The R^2 value for this model is 93%. The most influential scaling factors that define minimum spouting velocity are found to be d_p/D_c and H_0/d_p. The effect of ρ_s/ρ_g is masked by H_0/d_p (Refer to Section 4.2.3).

Both models establish the following trends, U_{ms} is strongly positively correlated to H_0 and d_p, and negatively correlated with D_c. These trends are supported by what physically is reasonable in the behavior of shallow spouted bed.

Experimentally, minimum spouting velocity for a fixed, shallow spouted bed operating with dense particles was found to increase with increasing static bed height (H_0), particle diameter (d_p) and particle density (ρ_s), and also with decreasing fluidizing gas density(ρ_g) and column diameter (D_c) (Refer to appendix A). These observations seem to be generally consistent with the results of Mathur and Gishler [41], a pioneer of the spouted bed technique, which are presented in the following equation.

$$U_{ms} = (d_p / D_c)(D_i/D_c)^{1/3}\sqrt{2gH(\rho_s - \rho_g)/\rho_g} \qquad 4.23$$

Three correlations were selected for comparison to the final model for minimum spouting velocity (Equation 4.22) because of the similitude in some operating conditions considered in this investigation.

The parameter variations under which these minimum spouting velocity correlations were developed are summarized in **Table 4.11**. The parameter variations in the experiments for the Lima correlation are included for easy comparison. As noted throughout this work the correlations of Mathur and Gishler [41] and Olazar were developed for deeper beds with denser particles. A comparison of the experimental U_{ms} values with the predicted values by the Lima (Equation 4.22), Zhou [32], Mathur and Gishler[41] and Olazar et. al [46] correlations is illustrated in Figure 4.45.

Table 4.11: Parameters variations in U_{ms} correlations

Correlation	Lima	Zhou	Olazar et al.	Mathur and Gishler
Equation number	4.22	4.24	4.25	4.23
D_c [mm]	50, 80, 150	50	360	76 - 300
H_0/D_c	0.42 - 1.0	0.5 - 1	1 - 1.7	$\geq$ 1.3
d_p [mm]	500, 1000, 2000	300 - 650	1000 - 2500	500 - 3100
ρ_s [kg/m^3]	3800, 6000, 7600	6000	240 - 3520	1100 - 2670
D_i [mm]	D_i/D_c=0.08	4	3 - 6	1.6-54
γ °	60	45, 60, 75	28 - 45	85
gas	Helium,Air	Air	Air	Air, Water
ρ_g [kg/m^3]	0.17,1.18	1.18	1.18	1.18, 1000
μ_g [kg/m s]	$1.98x10^{-5}$, $1.87x10^{-5}$	$1.98x10^{-5}$	$1.98x10^{-5}$	$1.98x10^{-5}$, $8.9x10^{-4}$

The Mathur and Gishler correlation (Equation 4.23) is valid for deep beds ($H_0/D_c \geq 1.3$) with the following ranges in the operating conditions: ρ_s=1100 - 2670 kg/m^3, γ=85° (cone angle), d_p=500-3100 µm and D_c=76-300 mm bed using air as the fluidizing gas. This equation must be extrapolated for the prediction of U_{ms} beds under the operating conditions considered in this investigation since the bed is shallow spouted , the densities are ρ_s>3880 kg/m^3 and cone angle of γ=60°.

The Zhou correlation (Equation 4.24) was developed with just YSZ particles covering these ranges: H_0/D_c=0.5-1, γ=45-75°, D_i=4 mm, d_p=300-650 µm for a 50 mm bed using air as fluidizing gas.

$$\mathrm{Re}_{ms} = 0.0015\, Ar^{0.86} \left(\frac{H_0}{D_c}\right)^{1.59} \tan\left(\frac{\gamma}{2}\right)^{0.87} \qquad 4.24$$

Even though Zhou's correlation is valid for shallow beds, it must extrapolated for the prediction of shallow spouted beds experiments using d_p>650 µm, lower gas density than air, particle density other than 6000 kg/m^3, and larger column diameters than 50 mm. In contrast to that of Zhou, the experiments performed in this investigation include a larger range of parameters: H_0/D_c=0.42-1, d_p=500-2000 µm, ρ_s=3880-7600 kg/m^3, ρ_g=0.17-1.18 kg/m^3 and D_c=50-150 mm for a 60° inclusive cone angle.

The Olazar et al. correlation (Equation 4.25) is utlizied data that encompassed these ranges: D_i=30-60 mm, H_o=360-610 mm, γ=28-45°, d_p=1-25 mm, ρ_s=240-3520 kg/m^3 for a 360 mm bed

$$\left(\mathrm{Re}_i\right)_{ms} = 0.126 Ar^{0.5}\left(1+2\tan(\gamma/2)\,H_0/D_i\right)^{1.68}\left(\tan(\gamma/2)\right)^{0.57} \qquad 4.25$$

This correlation is valid for moderately deep beds (H_0/D_c=1-2) which limits the prediction of shallow spouted beds at H_0/D_c<1. Also it requires extrapolation for the predictions for all the particle densities used in this investigation.

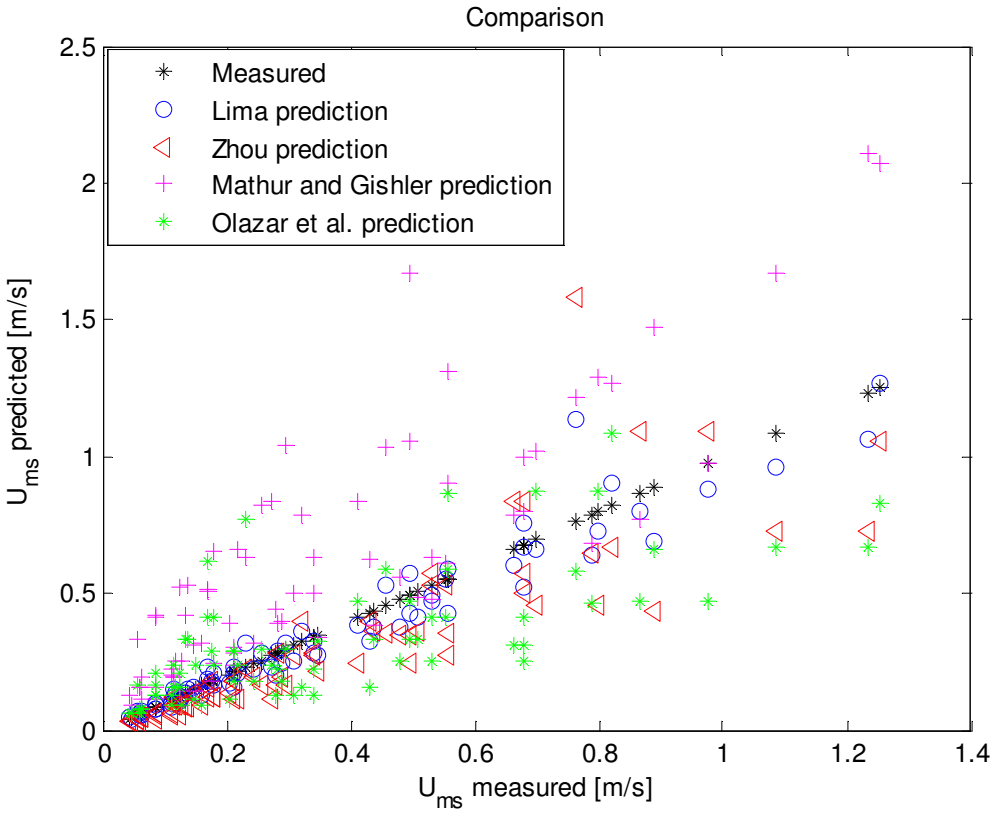

Figure 4.45: U_{ms} measured vs. predicted by different correlations.

The values predicted with the Zhou correlation up to 0.2 show good fit with experimental data, those values correspond mostly to the experiments spouting using 500µm diameter particles, which is in the range of validation (350-650 µm) of the Zhou correlation. His correlation performs better than the other literature correlations, likely because it required the least extrapolation.

Olazar et al. correlation (Equation 4.25) correlation shows the right trend but is very scattered.

There is small scattering between Equation 4.22 (Lima prediction) and the measured values of U_{ms}, confirming the high correlation value for the model for the experiments performed in this investigation. The values predicted with the Zhou correlation up to 0.2 m/s show good fit with experimental U_{ms} data, those values correspond mainly to the experiments spouting 500µm, a diameter which is in the range of validation (350-650 µm) of the Zhou correlation. The Olazar correlation shows the right trend but is very scattered. The Mathur and Gishler correlation overestimates the U_{ms} values and is even more scattered. The Lima correlation provides superior prediction for U_{ms} values.

4.5.2 *Bed pressure drop at U_{ms} (ΔP_{ms})*

Two different regression models were developed to correlate bed pressure drop at minimum spouting condition. The first model was developed with respect to five dimensionless variables $\left\{\frac{d_p}{D_c}, Ar, \frac{\rho_s}{\rho_g}, \frac{H_0}{d_p}, \frac{U_{ms}^2}{g d_p}\right\}$ and the second model with respect to two variables $\left\{\mathrm{Re}_{ms}, \frac{H_0}{d_p}\right\}$; which are indirectly the most common variables used to correlate bed pressure drop in the literature, H_0/D_c and Re_{ms} (see Table 2.3). Both regression models include data from most of the cases where pressure drop was positive at U_{ms}; including constant, decreasing and bisectionally decreasing pressure drop behaviors listed in Table 4.1. Those cases include the following variation of parameters: column diameter (50, 80 and 150 mm), static bed height (H_0/D_c=0.42, 0.67 and 1), particle diameter (500 and 1000 µm), gas density (0.17 and 1.18 kg/m^3) and particle density (3880, 6000 and 7600 kg/m^3). The cases with 2000 µm particles were excluded because the pressure at U_{ms} was negative. These cases correspond to the fourth classification listed in Table 4.1.

The first correlation model is expressed as follows

$$\frac{\Delta P_{ms}}{\rho_s H_0 g} = 0.8831\left(\frac{d_p}{D_c}\right)^{0.001}(Ar)^{-0.1}\left(\frac{\rho_s}{\rho_g}\right)^{0.057}\left(\frac{H_0}{d_p}\right)^{-0.032}\left(\frac{U_{ms}^2}{g d_p}\right)^{-0.069} \qquad 4.26$$

The R^2 value is 85% and the most important dimensionless variables that define bed pressure drop at U_{ms} are found to be Ar, Fr_{ms} and H_0/d_p.

The second correlation for ΔP_{ms} is expressed as follows:

$$\frac{\Delta P_{ms}}{\rho_s H_0 g} = 0.5374\left(\mathrm{Re}_{ms}\right)^{-0.166}\left(\frac{H_0}{d_p}\right)^{-0.0064} \qquad 4.27$$

where $\mathrm{Re}_{ms} = \dfrac{\rho_g d_p U_{ms}}{\mu_g}$

The R^2 value is 86% and the more important factor that define bed pressure drop at minimum spouting velocity is found to be Re_{ms}. However, since Re_{ms} is a function of the variables of d_p, ρ_g and μ (gas viscosity), the latter terms have indirect influence on ΔP_{ms}, and is masked.

Recall that most of the published correlations for bed pressure drop in literature (see Table 1.3) are expressed in terms of H_0/D_c and Re_{ms} and regression model displayed in Equation 4.27 is similar to those published In comparing the two models notice that in Equation 4.27, the exponent of U_{ms} is ~ -0.14 (2×-0.064), comparable to that in Equation 4.26 which is -0.17.

The similarity between the fit by the two models (see Figure 4.31 and Figure 4.35) suggest that the variables of U_{ms}, H_0/d_p, along with ρ_s/ρ_g correlate well with the bed pressure drop at minimum spouting condition in a similar manner, reinforcing the tentative conclusion that Ar, U_{ms} and H_0/d_p are influential in determining the bed pressure drop at minimum spouting condition drawn from the first modeling effort (see Section 4.3).

After multiplying both sides of Equation 4.27 by H_0, it is seen that bed pressure drop at minimum spouting condition is positively correlated to H_0 and ρ_s, and μ (through Re_{ms} term), and inversely correlated to U_{ms}, ρ_g and d_p (through Re_{ms} term).

Experimentally, bed pressure drop increases with increasing static bed height and particle density and with decreasing particle diameter and fluidizing gas density (Refer to appendix A), consistent with the trend displayed by Equations 4.26 and 4.27. In addition, R^2 values of both models are comparable in magnitude indicating that bed pressure drop at minimum spouting condition can be estimated using either of these two models, however when scaling, the first model is the one that can give us direct information of pressure drop sensitivity to changing parameter values since the second model is defined in terms of Re_{ms}, a change in its value cannot be differentiated as to which parameter it contains is the one that has changed. .

A comparison of the experimental bed ΔP_{ms} values and predicted values by the Lima correlation of Equation 4.26, to that predicted by Zhou [32], Mukhlenov and Gorshtein [36] and Olazar et al. [46] is illustrated in Figure 4.46. These equations were selected because of the similitude in some operating conditions considered in this investigation.

The parameter variations under which these bed pressure drop at minimum spouting velocity correlations were developed are summarized in Table 4.12. The parameter variations in the experiments for the Lima correlation are included for easy comparison.

Table 4.12: Parameters variations in ΔP_{ms} correlations

Correlation	Lima	Zhou	Olazar et al.	Mukhlenov and Gorshtein
Equation number	4.26	4.28	4.29	4.30
D_c [mm]	50, 80, 150	50	360	50
H_0/D_c	0.42 - 1.0	0.5 - 1	1 - 1.7	0.6-3
d_p [mm]	500, 1000	300 - 650	1000 - 2500	500 - 2500
ρ_s [kg/m^3]	3800, 6000, 7600	6000	240 - 3520	1000 - 2360
D_i [mm]	D_i/D_c=0.08	4	30 - 60	10, 13
γ °	60	45, 60, 75	28 - 45	12, 60
gas	Helium,Air	Air	Air	
ρ_g [kg/m^3]	0.17,1.18	1.18	1.18	
μ_g [kg/m s]	1.98x10^{-5}, 1.87x10^{-5}	1.98x10^{-5}	1.98x10^{-5}	

The Zhou correlation (Equation 4.28) used the same data that was used for his U_{ms} correlation. Thus, it was developed with just YSZ particles at these ranges: H_0/D_c=0.5-1, γ=45-75°, D_i=4 mm, d_p=300-650 µm for a 50 mm bed using air as fluidizing gas.

$$\frac{\Delta P_s}{\rho_s H_0 g} = 1.05\left[\tan(\frac{\gamma}{2})\right]^{0.057} \mathrm{Re}_{ms}^{-0.1}(\frac{H_0}{D_c})^{0.224} \qquad 4.28$$

Even though Zhou's correlation is valid for shallow beds, it must extrapolated for the prediction of shallow spouted beds experiments using d_p>650 µm, lower gas density than air, participle density other than 6000 kg/m^3, and larger column diameters than 50 mm. At a difference from that of Zhou, the experiments performed in this investigation include a larger range of parameters: H_0/D_c=0.42-1, d_p=500-2000 µm, ρ_s=3880-7600 kg/m^3, ρ_g=0.17-1.18 kg/m^3 and D_c=50-150 mm for a 60° inclusive cone angle.

The Olazar et al. correlation (Equation 4.29) is valid for these ranges: D_i=30-60 mm, H_0=360-610 mm, γ=28-45°, d_p=1-2.5 mm, ρ_s=240-3520 kg/m^3 for a 360 mm bed.

$$\left(-\Delta P_s / H_c \rho_b g\right)_{cone} = 1.2\left[\tan(\gamma/2)\right]^{-0.11}\left(\mathrm{Re}_i\right)_{ms}^{-0.06}\left(H_c / D_i\right)^{0.08} \qquad 4.29$$

The Olazar et al correlation is for moderately deep beds (H_0/D_c=1-2) which requires extrapolation for the prediction of shallow spouted beds (H_0/D_c<1). In addition, it was developed with lower density particles than in the present work. The bed was considerably larger but the D_i/D_c ratio was 0.08 – 0.16 which compares to the present laboratory ratio of 0.08. The cone was steeper compared to the 60° angle utilized in this work.

The model of Mukhlenov and Gorshtein (Equation 4.30) is valid for these ranges: D_i=10.3-12.9 mm, H_0=30-150 mm, γ=12-60°, d_p=500-2500 μm, ρ_s=1000-2360 kg/m^3 for a 50 mm bed

$$-\Delta P_s / H_0 \rho_b g = 7.68\left[\tan(\gamma/2)\right]^{0.2} \left(\mathrm{Re}_i\right)_{ms}^{-0.2} \left(H_0 / D_i\right)^{-0.33} \qquad 4.30$$

This correlation was developed with just a 50 mm bed and with lower density particles than in the present work. The H_0/D_c ratio was 0.6-3 which overlaps with the 0.42-1 range of the present lab results. The D_i/D_c ratio was 0.2-0.26 which is 2 to 3 times that of the present work. Notice that particle diameters used to develop this correlation are similar to those used in this investigation (500-2000 μm), which may suggest that this equation should fit the results presented in this investigation better than the Olazar et al. equation, however this is not the case (see Figure 4.46).

Values predicted from these literature model equations at the set of experimental values used in this investigation tend to overestimate by about a factor of 2 the values of bed pressure drop at minimum spouting velocity, as shown in Figure 4.46. It is anticipated that Zhou's correlation would be accurate at the lower U_{ms} values as with the correlation for U_{ms} shown in Figure 4.45 due to the close match in experimental parameters at low U_{ms} conditions. This expected comparison was not borne out in Figure 4.46. In fact the Zhou correlation tracked the other two literature correlations and both significantly (typically by a factor of 2) overestimate the ΔP_{ms} values and have significant scatter. The Zhou correlation does exhibit less overestimation.

No specific reason has been identified to explain the 'two results' displayed in the comparison among the correlations: the trend given by all three literature correlations and very accurate results of the new correlation.

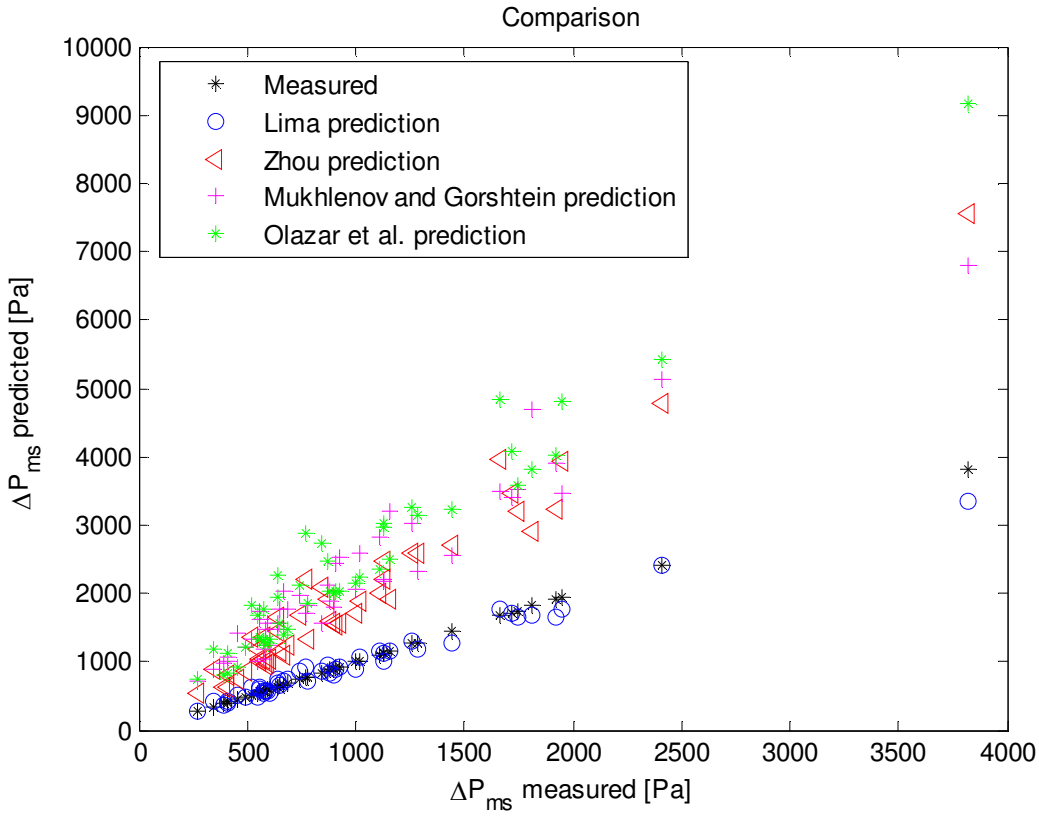

Figure 4.46: ΔP_{ms} measured vs. predicted by different correlations.

The relatively high regression coefficient for the model reported in this research for bed pressure drop is illustrated by the excellent prediction by Equation 4.26 (Lima correlation) for the measured values of for the measured values of ΔP_{ms} at U_{ms}. No scatter in this result is an indication of excellent laboratory work.

4.5.3 *Fountain Height (H_f)*

Measuring the fountain height employed sophisticated analysis. As discussed in Section x.y, a fountain height above the aluminum cone is obtained from the analysis of a 30 frame digital composite image. This is the average height above the cone if the bed is spouting in the erratic regime. Since the settled bed height, H_0, is at most 0.87 the height of the cone ($H_o/D_c \leq 1$ with an inclusive cone angle of 60º), the distance from the bed surface to the top of the cone must be added to the height of the fountain above the cone. There is relatively little literature on fountain height prediction based on correlation of spouting bed data. Three correlations were identified in the literature search. Two of these models were selected for comparison with the new correlation presented in this section because of the similarity on the parameters they use to predict fountain height.

A regression model was developed to correlate fountain height with four dimensionless input variables. This model is valid for the regular spouting regime only as described in Section 4.1.3, which also include semi-regular spouting regime cases. Data used (see Table 4.4) include the following variation of parameters; column diameter (50 and 80 mm bed), static bed height (H_0/D_c=0.42, 0.67 and 1), particle diameter (500, 1000 and 2000 μm), gas density (0.17 and 1.18 kg/m^3) and particle density (3880, 6000 and 7600kg/m^3). The largest bed (150 mm) was not used since the spouting regime presented in this bed corresponds to the erratic regime. Irregular spouting regimes most likely are not described well by the developed model.

The correlation model is expressed as follows:

$$\frac{H_f}{H_{f\_\max}} = 0.002\left(\frac{d_p}{D_c}\right)^{0.68}(Ar)^{0.19}\left(\frac{H_0}{d_p}\right)^{1.1}\left(U/U_{ms}\right)^{3.42} \qquad 4.31$$

where H_{f_max}=0.1193 m.

H_{f_max} is defined as the largest H_f value measured from all spouting bed cases included in the reference and validation sets used in the PCR model development. H_{f_max} was introduced in the PCR modeling procedure to normalize the response variable $H_f/ H_{f\_max} \leq 1$ for all cases included in the analysis.

The R^2 for this model is 87%. The most important factors that define fountain height are found to be U/U_{ms}, H_0/d_p and to some extent d_p/D_c.

Multiplying both sides of Equation 4.31 by $H_{f\text{-}max}$ and substituting 0.1193m for $H_{f\text{-}max}$ gives Equation 4.32 for H_f with units of meters.

$$H_f = 0.00024\left(\frac{d_p}{D_c}\right)^{0.68}(Ar)^{0.19}\left(\frac{H_0}{d_p}\right)^{1.1}\left(U/U_{ms}\right)^{3.42} \qquad 4.32$$

Fountain height is positively correlated to more than the cubes of U/U_{ms}, and inversely correlated to D_c. The effect of H_0, ρ_s and d_p are masked by U_{ms}, since the latter is already a function of these terms among others.

Experimentally, fountain height increases with increasing gas flow rate, gas density, particle diameter, column diameter and static bed height and decreasing particle density (refer to Appendix A). These trends agree with physical intuition and they are consistent with trends displayed by the new Lima correlation (Equation 4.32) and in agreement with findings of Zhou [32]. Changing the fluidization gas from air to helium can be considered as a surrogate to

changing the temperature of the fluidizing gas, in that, the density of the gas is changed. For the gases air and helium the viscosity is nearly the same at room temperature but the density change is about a factor of 7. However, as has been published by Lima Rojas [44], the effect of temperature on the fluidizing gases as studied by Wu *et al.* [40] agrees with the finding in this investigation; fountain height decreases as the temperature of the fluidizing gas increases, which is reflected in a reduction of the drag force because of the reduction in gas density.

A comparison of the experimental H_f values to that predicted by Equation 4.32, to that predicted by Zhou [32] and to that predicted by San Jose et al. [39] is illustrated in Figure 4.47.

The parameter variations under which fountain height correlations were developed are summarized in Table 4.13. The parameter variations in the experiments for the Lima correlation are included for easy comparison.

Table 4.13: Parameters variations in H_f correlations

Correlation	**Lima**	**Zhou**	**San Jose et al.**
Equation number	4.32	4.33	4.34
D_c [mm]	50, 80, 150	50	360
H_0/D_c	0.42 - 1.0	0.5 - 1	0.14-0.97
d_p [mm]	500, 1000, 2000	300 - 650	1000-3500
ρ_s [kg/m^3]	3800, 6000, 7600	6000	70-1030
D_i [mm]	D_i/D_c=0.08	4	30-50
γ °	60	45, 60, 75	28 - 45
Gas	Helium,Air	Air	Air
ρ_g [kg/m^3]	0.17,1.18	1.18	1.18
μ_g [kg/m s]	1.98x10^{-5}, 1.87x10^{-5}	1.98x10^{-5}	1.98x10^{-5}

The Zhou correlation (Equation 4.33) used the same data that was used for his U_{ms} correlation. Thus, it was developed with only YSZ particles at these ranges: H_0/D_c=0.5-1, γ=45-75°, D_i=4 mm, d_p=300-650 µm for a 50 mm bed using air as fluidizing gas.

$$\frac{H_f}{H_0} = 7.15\gamma^{0.64}\left(\frac{d_p}{D_c}\right)^{0.20}\left(\frac{H_0}{D_c}\right)^{0.34}\left(\frac{U}{U_{ms}}\right)^{1.03} \qquad 4.33$$

Even though Zhou's correlation is valid for shallow beds, it must extrapolated for the prediction of shallow spouted beds experiments using particles of d_p>650 µm, lower gas density than air, participle density other than 6000 kg/m^3, and larger column diameters than 50 mm Different from that of Zhou, the experiments performed in this investigation include a larger range of

parameters: H_0/D_c=0.42-1, d_p=500-2000 µm, ρ_s=3880-7600 kg/m^3, ρ_g=0.17-1.18 kg/m^3 and D_c=50-150 mm for a 60° inclusive cone angle.

The San Jose et al. correlation (Equation 4.34) is valid for these ranges: D_i=30-50 mm, H_0/D_c<1, γ=28-45°, d_p=1-3.5 mm, ρ_s=70-1030 kg/m^3 for a 360 mm bed.

$$H_f = 1.01x10^{-2}\gamma^{-0.14}\left(\frac{D_i}{D_{bc}}\right)^{-1.14}\left(\frac{d_p}{D_i}\right)^{-0.83}\left(\frac{H_0}{D_{bc}}\right)^{-0.52}\left(\frac{U}{U_{ms}}\right)^{4.8}\rho_s^{-0.12}\phi^{-1.45} \qquad 4.34$$

where D_{bc} denotes the bed bottom diameter and D_i denotes the inlet diameter, and they are the same for the beds used in this investigation.

San Jose et al correlation is valid for very shallow spouted beds (H_0/D_c<1). In addition, it was developed with lower density particles than in the present work. It uses larger particle diameter than 500µm. The bed was considerably larger but the D_i/D_c ratio was 0.08 which compares to the present laboratory ratio of 0.08. The cone was steeper compared to the 60° angle utilized in this work.

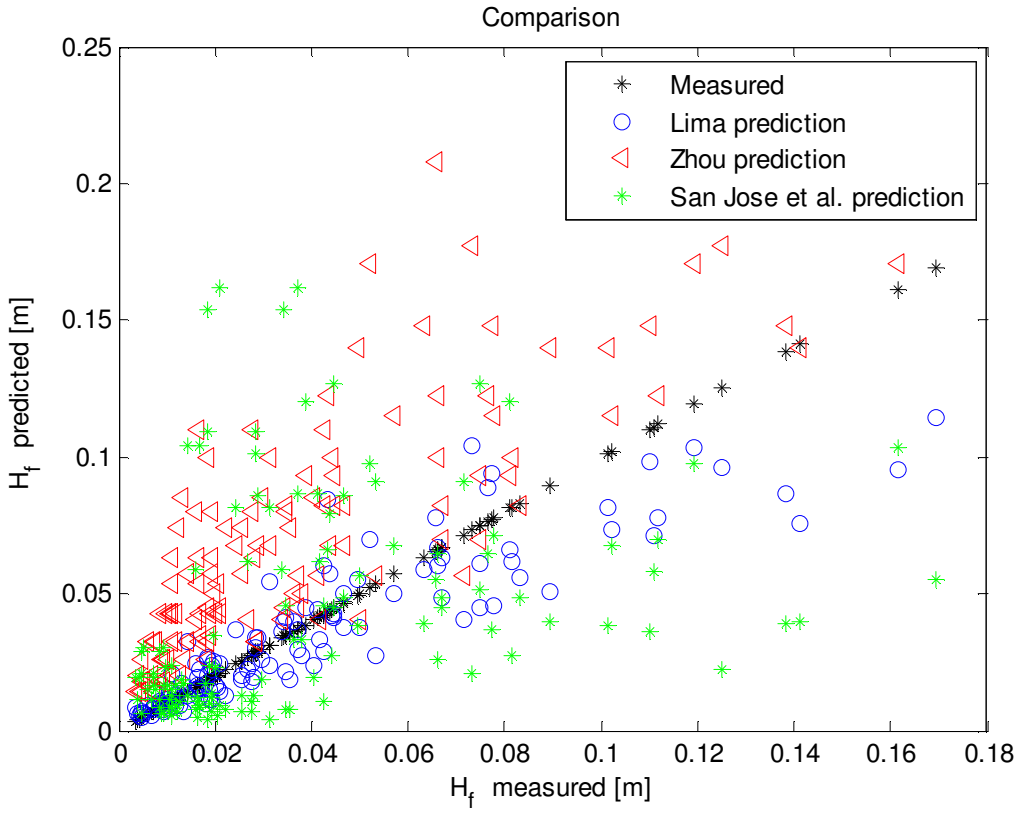

Figure 4.47: H_f measured vs. predicted by different correlations.

In contrast with the comparison of Lima correlations for U_{ms} and ΔP_{ms} (Equations 4.22 and 4.26) using different models, the scattering between Lima correlation for H_f (Equation 4.32) and the measured values of H_f is larger. However compared with the scattered data predicted by Zhou and San Jose et al. correlations, Equation 4.32 does very well and yields the best fit between measured and predicted data. The Lima correlation does very well in predicting H_f up to 0.02, rather well up to 0.07 but gives low predictions above 0.07 with considerable scatter. The Zhou correlation, in general, overestimates values of H_f. Also notice that the scattering of predicted values of H_f increases with increasing measured values; this suggests that a different model to fit higher H_f data might be necessary to improve the correlation for fountain height. This is left for future investigations. In addition, of the three literature correlations only Zhou's is in dimensionless form using H_f/H_0. The other two give equations for a dimensional H_f. It is suggested that alternate schemes be investigated to normalize H_f.

Prediction equations developed in this investigation should be by the user used with caution to make sure that the operating conditions are within the range in which the models are valid. In addition, all operating variables should be represented in MKS system: kg, m and sec.

Overall hydrodynamic trends displayed by the regression models developed here for minimum spouting velocity, bed pressure drop at U_{ms} and fountain height with respect to the design parameters of static height (H_0), particle diameter (d_p), column diameter (D_c), solid density (ρ_s), gas density (ρ_g) and minimum spouting velocity (U_{ms}) (for bed pressure drop at minimum spouting velocity (ΔP_{ms}) and fountain height (H_f)) are all consistent with 1) analysis results derived directly from experimental results reported here (see Appendix A) and 2) trends reported in open literature on deep and shallow spouted beds for lighter particles. Results on global hydrodynamic characterization reported in this dissertation are very encouraging in shedding light on the behavior of shallow spouted beds fluidizing heavy particles. Future research in this area is proposed and undoubtedly will advance further the understanding of the behavior of shallow spouted beds for high-density particles.

5. Conclusions

5.1. Conclusions

The main purposes of this investigation were to identify the most important dimensionless numbers that define the hydrodynamics of shallow spouted beds of dense particles and to develop dimensionless scaling correlations for minimum spouting velocity, bed pressure drop at minimum spouting velocity and fountain height. The approach to carry out the objectives included performing a set of initial screening experiments, at ambient temperature and pressure, to identify the experimental parameters having the greatest impact on the observed minimum-spouting velocity. Subsequently, more detailed experiments were implemented to further refine the empirical correlations. The experimental parameters explored included column (bed) diameter, packed bed height, particle diameter, particle density, gas density and gas flow rate.

In the experiments, four types of relationships (pattern) were observed between bed pressure drop and gas flow. These relationships were characterized by the variations of bed pressure drop at and above the minimum spouting velocity. These relationships were classified as constant, slightly decreasing, 'decreasing and negative', and bisectionally constant pressure drop. For the case of 'decreasing and negative' pressure drop, the pressure drop discontinuity at minimum spouting velocity was difficult to identify, and thus direct visual observations was required to determine minimum spouting velocity.

With regard to spouting modes three general patterns were observed: regular, erratic and bimodal. The erratic mode was subdivided further into fully erratic and semi-regular modes. These modes were most easily distinguished in terms of the dynamic behavior of the fountain. Regular spouting corresponds to stable fountains, with only very small oscillations in the observed height on short timescales. Erratic spouting regime was identified for very shallow beds in combination with the largest particles, where two spouting regimes (jet spouting and intermittency between jet and regular spouting) were observed while decreasing the gas flow rate from fully spouting condition down to the minimum spouting condition. Gaining further understanding of this spouting regime is left to future investigations.

A preliminary spouting regime map was generated to discriminate the different spouting regimes. The existence of these different regimes implies that bed scale-up should be done with caution since abrupt spouting regime transitions are possible. This preliminary regime map might be useful in identifying the likelihood of such transitions. The correspondence between pressure drop patterns and spouting regimes is still unclear. This is a ripe area for future investigations.

Overall hydrodynamic trends captured by the regression models developed for minimum spouting velocity, bed pressure drop at minimum spouting condition and fountain height with respect to the design parameters of static height (H_0), particle diameter (d_p), column diameter (D_c), solid density (ρ_s), gas density (ρ_g) and minimum spouting velocity (U_{ms}) (for bed pressure drop at minimum spouting velocity (ΔP_{ms}) and fountain height (H_f)) are all consistent with experimental results and trends reported in open literature on deep and shallow spouted beds for lighter particles.

Minimum spouting velocity for shallow spouted bed operating with dense particles was found to increase with increasing static bed height, particle diameter and particle density, and also with decreasing fluidizing gas density. It was found that d_p/D_c and H_0/d_p are the most important dimensionless groups that correlate with U_{ms}/U_t.

It was found that bed pressure drop at minimum spouting condition increases with increasing static bed height and particle density and with decreasing particle diameter and fluidizing gas density. Also, it was found that Ar, H_0/d_p and U^2_{ms}/gd_p are the most important dimensionless groups that correlate with pressure drop at minimum spouting condition. A predictive correlation was developed for all conditions under which the overall pressure drop was nonnegative.

Fountain bed height increases with increasing gas flow rate, gas density, particle diameter and static bed height, and with decreasing particle density. It was found that U/U_{ms} and H_0/d_p are the most important dimensionless groups that correlate with fountain height. A predictive correlation was developed for all conditions under which the spouting dynamics were in the regular and semi-regular regimes.

5.2. Future Work

Clearly there is a need to better understand the different spouting regimes and bed pressure drop patterns. It is suggested that the regime map developed might be useful as a starting point for future experiments.

Tentatively, spouting regimes could be characterized quantitatively using the coefficient of variation of the centroid of the fountain height or the pressure drop time series. The latter might be easier to implement. A spouting regime map might be better delimited using this method.

Further research on the hydrodynamic behavior in the 150 mm bed should be conducted. Since the spouting for 500 μm particles is very unstable, larger and/or lighter particles might fluidize in the regular spouting regime. The effect of the inlet diameter and smaller cone angle should also be analyzed in conjunction with the other parameters for this particular bed size.

Preliminary observations suggest that the bimodal spouting regime could be characterized better with dynamical tools such as high speed pressure drop and/or video imaging.

The variation of the bed pressure drop with flow needs to be studied more to explain the different patterns that were observed. These patterns are not reported in the literature. It is recommended that statistical analysis of the pressure drop time series and video images might reveal correlations between the spouting regimes and pressure drop trends.

The appearance of the jump in the pressure drop beyond $2U_{ms}$, as observed in the bisectionally constant pressure drop pattern, should be further studied to determine if it is correlated with a transition of spouting regime.

Since overall bed pressure drop was observed to go negative under certain combination of operating conditions, especially at high gas flow rates, it would be useful to explore these conditions using additional pressure measurements at different locations than the wall. This might help better resolve the details of the complex flow patterns that produce the negative bed pressure drops.

The presence of an apparent lack of fit for the current pressure drop correlation suggests that the underlying model can be improved.

The prediction error of the current fountain height correlation increases with fountain height, implying that a different reference point to measure fountain height might improve the correlation. Also it is suggested that alternate schemes be investigated to normalize H_f to avoid the arbitrary H_{f_max}.

References

1. D. Kunii and O. Levenspiel, *Fluidization Engineering*, 2nd ed. USA: Butterworth-Heinemann, 1991.

2. X. L. Zhao, Q. Yao and S. Q. Li, Effects of draft tubes on particle velocity profiles in spouted beds, *Chemical Engineering Technology*, Vol. **29**, No. 7, pp. 875–881, 2006.

3. X.-L. Zhao, Q. Yao and S.-Q. Li, Fluid and solids flow affecting the solids circulation rate in spouted beds with a draft tube, *Journal of Chemical Engineering of Japan*, Vol. **37**, pp. 1085–1091, 2004.

4. V. E. Kutsakova, Drying of liquid and pasty products in a modified spouted bed of inert particles, *Drying Technology*, Vol. **22**, No. 10, pp. 2343–2350, 2004.

5. P. A. Salam and S. C. Bhattacharya, A comparative study of charcoal gasification in two types of spouted bed reactors, *Energy*, Vol. **31**, pp. 228–243, 2006.

6. J. Villa and J. Guardiola, New methodology for scaling hydrodynamic data from a 2D-fluidized bed, *Chemical Engineering Science*, Vol. **60**, pp. 5151–5163, 2005.

7. J H. T. Bi, A discussion on minimum spout velocity and jet penetration length, *The Canadian Journal of Chemical Engineering*, Vol. **82**, pp. 4–10, 2004.

8. L. R. Glicksman, Scaling relationships for fluidized beds, *Chemical Engineering Science*, Vol. **39**, No. 9, pp. 1373–1379, 1984.

9. L. R. Glicksman, M. Hyre and K. Woloshun, Simplified scaling relationships for fluidized beds, *Powder Technology*, Vol. **77**, pp. 177–199, 1993.

10. L. R. Glicksman, M. R. Hyre and P. A. Farrel, Dynamic similarity in fluidization, *International Journal of Multiphase Flow*, Vol. **20**, Suppl., pp. 331–386, 1994.

11. L. R. Glicksman, Scaling relationships for fluidized beds, *Chemical Engineering Science*, Vol. **43**, No. 6, pp. 1419–1421, 1988.

12. M. Horio, H. Ishii, Y. Sawa and I. Muchi, A new similarity rule for fluidized bed scale up, *AIChE Journal*, Vol. **32**, No. 9, pp. 1466–1482, 1986.

13. Y. L. He, C. J. Lim and J. R. Grace, Scale-up studies of spouted beds, *Chemical Engineering Science*, Vol. **52**, No. 2, pp. 329–339, 1997.

14. J. Xu, Y. Ji, W. Wei, X. Bao and W. Du, Scaling relationships of gas-solid spouted beds, *Proceedings of the 12th International Conference on Fluidization*, Vol. **RP4**, Article 65, pp. 537–544, 2007.

15. M. J. V. Goldschmidt, J. A. M. Kuipers and W. P. M. van Swaaij, Hydrodynamic modeling of dense gas-fluidized beds using the kinetic theory of granular flow: Effect of coefficient of restitution on bed dynamics, *Chemical Engineering Science*, Vol. **56**, No. 2, pp. 571–578, 2001.

16. P. A. Shirvanian and J.M.Calo, Hydrodynamic scaling of a rectangular spouted vessel with a draft tube, *Chemical Engineering Journal*, Vol. **103**, No. 1-3, pp. 29-34, 2004.

17. M. J. San José, M. Olazar, R. Aguado and J. Bilbao, Influence of the conical section geometry on the hydrodynamics of shallow spouted beds, *Chemical Engineering Journal*, Vol. **62**, pp. 113–120, 1996.

18. L. P. Leu and M. C. Lo, Pressure fluctuations in spouted bed, *Journal of the Chinese Institute of Chemical Engineers*, Vol. **36**, No. 4, pp. 391–398, 2005.

19. M. J. San José, S. Alvarez, A. Ortiz de Salazar, M. Olazar and J. Bilbao, Influence of the particle diameter and density in the gas velocity in jet spouted beds, *Chemical Engineering and Processing*, Vol. **44**, Issue 2, pp. 153–157, 2005.

20. M. J. San José, S. Alvarez, A. Ortiz de Salazar, M. Olazar and J. Bilbao, Spout geometry in shallow spouted beds with solids of different density and different sphericity, *Industrial and Engineering Chemistry Research*, Vol. **44**, No. 22, pp. 8393–8400, 2005.

21. Z. Wang, H. T. Bi, C. Lim and P. Su, Determination of minimum spouting velocities in conical spouted beds, *Canadian Journal of Chemical Engineering*, Vol. **82**, pp. 11–19, 2004.

22. A. Delebarre, Revisiting the Wen and Yu equations for minimum fluidization velocity prediction, *Chemical Engineering Research and Design*, Vol. **82**, No. A5, pp. 587–590, 2004.

23. Z. Wang, P. Chen, H. Li, C. Wu and Y. Chen, Study on the hydrodynamics of a spouting-moving bed, *Industrial and Engineering Chemistry Research*, Vol. **40**, pp. 4983–4989, 2001.

24. M. Olazar, M. J. San José, M. A. Izquierdo, S. Alvarez and J. Bilbao, Local bed voidage in spouted beds, *Industrial and Engineering Chemistry Research*, Vol. **40**, pp. 427–433, 2001.

25. S. Aravinth and T. Murugesan, A general correlation for the minimum spouting velocity, *Bioprocess Engineering*, Vol. **16**, pp. 289–293, 1997.

26. H. T. Bi, A. Macchi, J. Chaouki and R. Legros, Minimum spouting velocity of conical spouted beds, *Canadian Journal of Chemical Engineering*, Vol. **75**, pp. 460–464, 1997.

27. M. Olazar, M. J. San José, A. T. Aguayo, J. M. Arandes and J. Bilbao, Pressure drop in conical spouted beds, *Chemical Engineering Journal*, Vol. **51**, pp. 53–60, 1993.

28. A. G. Fane and R. A. Mitchell, Minimum spouting velocity of scaled-up beds, *Canadian Journal of Chemical Engineering*, Vol. **62**, pp. 437–439, 1984.

29. H. Littman and M. H. Morgan, A general correlation for the minimum spouting velocity, *Canadian Journal of Chemical Engineering*, Vol. **61**, pp. 269–273, 1983.

30. M. Olazar, M. San José, M. Izquierdo, S. Alvare**z** and J. **B**ilbao, Fountain geometry in shallow spouted beds, *Industrial and Engineerin**g** Chemistry Research*, Vol. **43**, pp. 1163–1168, 2004.

31. P. A. Salam and S.C. Bhattacharya, A comparative hydrodynamic study of two types of spouted bed reactor designs, *Chemical Engineering Science*, Vol. **61**, pp. 1946–1957, 2006.

32. J. Zhou, Hydrodynamics and modeling of shallow spouted bed with high density particles, Ph.D. Dissertation, University of Tennessee Chemical Engineering Department, 2008.

33. J. Xua, X. Baoa, W. Weia, G. Shia, S. Shena, H. T. Bi, J. R. Grace and C. J. Lim, Statistical and frequency analysis of pressure fluctuations in spouted beds, *Powder Technology*, Vol. **140**, pp. 141–154, 2004.

34. M. Choi and A. Meisen, Hydrodynamics of shallow, conical spouted beds, *Canadian Journal of Chemical Engineering*, Vol. **70**, pp. 916-924, 1992.

35. D. C. Montgomery, Design and analysis of experiments, 6th ed., John Wiley & Sons, 2005. ISBN 0471-48735-X.

36. I. P. Mukhlenov and A. E. Gorshtein, Investigation of a spouting bed. *Zhurnal Khimicheskaya Promyhslennost*, Vol. **41**, pp. 443–446, 1965.

37. J. R. Grace and K. B. Mathur, Height and structure of the fountain above spouted beds, *Canadian Journal of Chemical Engineering*, Vol. **56**, No. 5, pp. 533–537, 1978.

38. J.-Y. Day, The fountain height and particle circulation rate in a spouted bed, *Chemical Engineering Science*, Vol. **45**, No. 9, pp. 2987–2990, 1990.

39. M. J. San José, M. Olazar, S. Alvarez, A. Morales and J. Bilbao, Spout and fountain geometry in conical spouted beds consisting of solids of varying density. *Industrial And Engineering Chemistry Research*, Vol. **44**, No. 1, pp. 193–200, 2005.

40. S. W. Wu, C. J. Lim and N. Epstein, Hydrodynamics of spouted beds at elevated temperatures, *Chemical Engineering Communications*, Vol. **62**, No. 1, pp. 251–268, 1987.

41. K.B. Mathur and P. E. Gishler, A technique for contacting gases with coarse solid particles. *AIChE Journal*, Vol. **1**, No. 2, pp. 157-164, 1955.

42. Z.G. Wang and H.T. Bi, Particle interlocking in conical spouted beds. *Chemical Engineering Science*, Vol. **60**, No. 19, pp. 5276–5283, 2005.

43. G. Strang, Linear algebra and its applications. 4th Edition, Thomson Brooks/Cole, 2006.

44. I.D. Lima Rojas, Preliminary results for the investigation of hydrodynamic scaling relationships in shallow spouted beds. *Separation Science and Technology*, Vol. **45**, pp. 1928-1934, 2010.

45. L. A. Madonnna and R.P. Lama, The derivation of an equation for predicting minimum spouting velocity. *AIChe Journal*, Vol. **4**, No. 4, pp. 497-497, 1958.

46. M. Olazar, M. J. San José, A. T. Aguayo, J. M. Arandes and J. Bilbao, Stable operation conditions for gas-solid contact regimes in conical spouted beds. *Ind. Eng. Chem. Res.*, Vol. **31**, No. 1, pp. 1784–1792, 1992.

APPENDIX A

EFFECT OF OPERATING CONDITIONS ON THE HYDRODYNAMICS OF SHALLOW SPOUTED BEDS

This section presents some example plots showing the effect of each operating condition on the minimum spouting velocity, bed pressure drop at minimum spouting velocity, and fountain height. Each operating condition corresponds to one of the parameters being varied in this investigation such as column diameter, particle size, particle density, gas density and column bed static height. A change of only a single parameter is made at a time while holding all other parameter values constant.

Error bars are added in the following plots for minimum spouting velocity, bed pressure drop and fountain height.

The error for the minimum spouting velocity values were computed using the propagation of error method of Kline and McClintock.

$$U = \frac{Q}{A}$$

where Q denotes the gas flow rate and A denotes the cross sectional area of the column.

$$U = QA^{-1}$$

$$w_U = \left[\left(\frac{\partial U}{\partial Q} w_Q \right)^2 + \left(\frac{\partial U}{\partial A} w_A \right)^2 \right]^{1/2}$$

$$w_U = \left[\left(A^{-1} w_Q \right)^2 + \left(-2QA^{-2} w_A \right)^2 \right]^{1/2}$$

where w denotes the error and here, w_Q=0.01 (slpm) and w_A=0.0001(m^2)

The error for bed pressure drop corresponds to 0.2% of average bed pressure drop value in Pascals listed in the specifications of the pressure sensor.

The error for fountain height (H_f) is the standard deviation of the difference between H_f measured and H_f predicted by the fitted line obtained from the H_f measured values as a function of U/U_{ms} values.

A1. Effect of operating conditions on U_{ms}

Effect of column diameter (D_c) on U_{ms}

U_{ms} decreases with column diameter, consistent with most literature correlations for deep beds, as confirmed in this study when the 50 mm bed is scaled to 80 mm; however, U_{ms} increases slightly from the 80 mm bed to 150 mm, which corresponds to a similar trend that has been observed for deep spouted beds. Fane *et al.* [28] found that at D_c<0.3 m, U_{ms} decreases with column diameter, but for 0.3<D_c<0.9 m, U_{ms} increases with column diameter. They suggest that for large beds, the gas flow "sees" a smaller-diameter region of bed (i.e., confined to a smaller zone within the bed), because the gas is unable to flow through the complete annulus area.

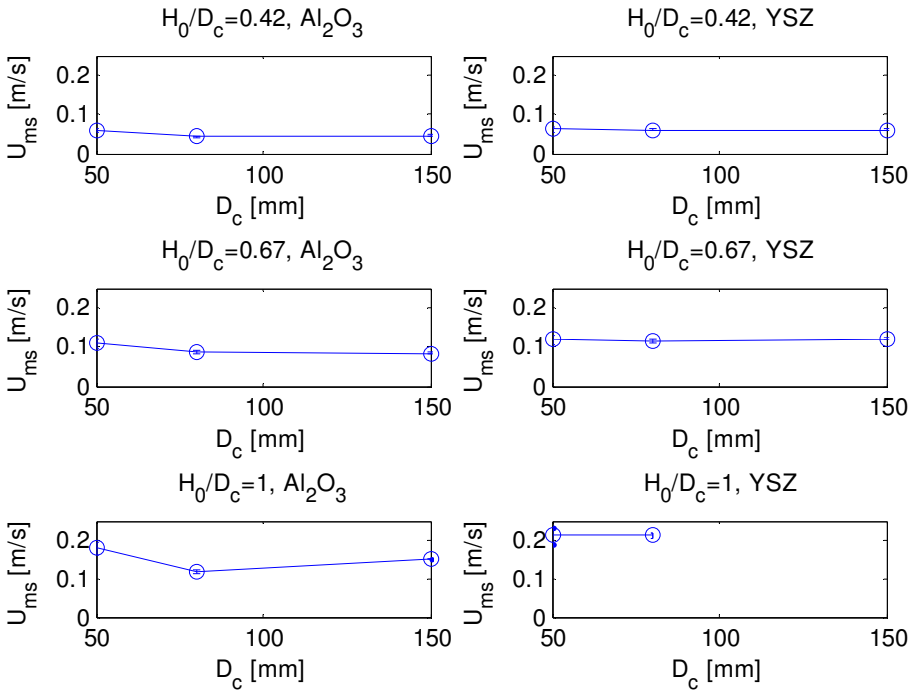

Figure A1.1: Effect of column diameter, static height and particle type on U_{ms} for 500 µm particles.

Effect of particle density (ρ_s) on U_{ms}

Figures A1.2 and A1.3 show that, U_{ms} increases with particle density going from 3800 to 6000 to 7600 kg/m^3. U_{ms} increases more drastically when going from 6000 to 7600 kg/m^3.

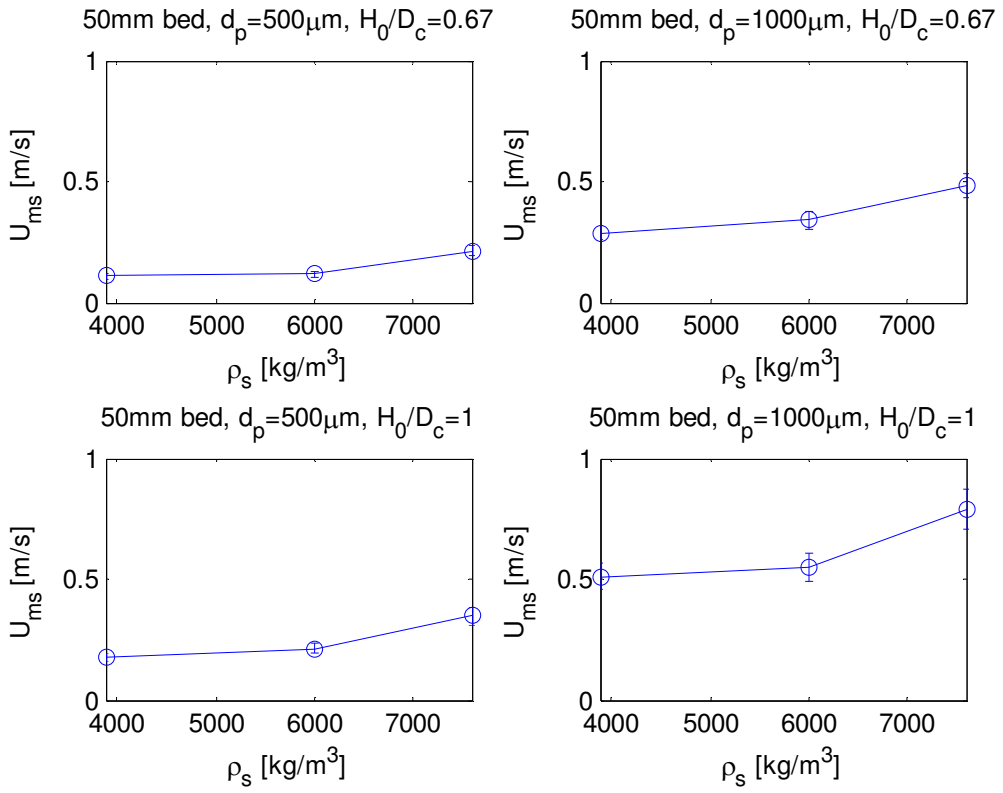

Figure A1.2: Effect of particle density on U_{ms} in the 50mm bed with air as fluidizing gas.

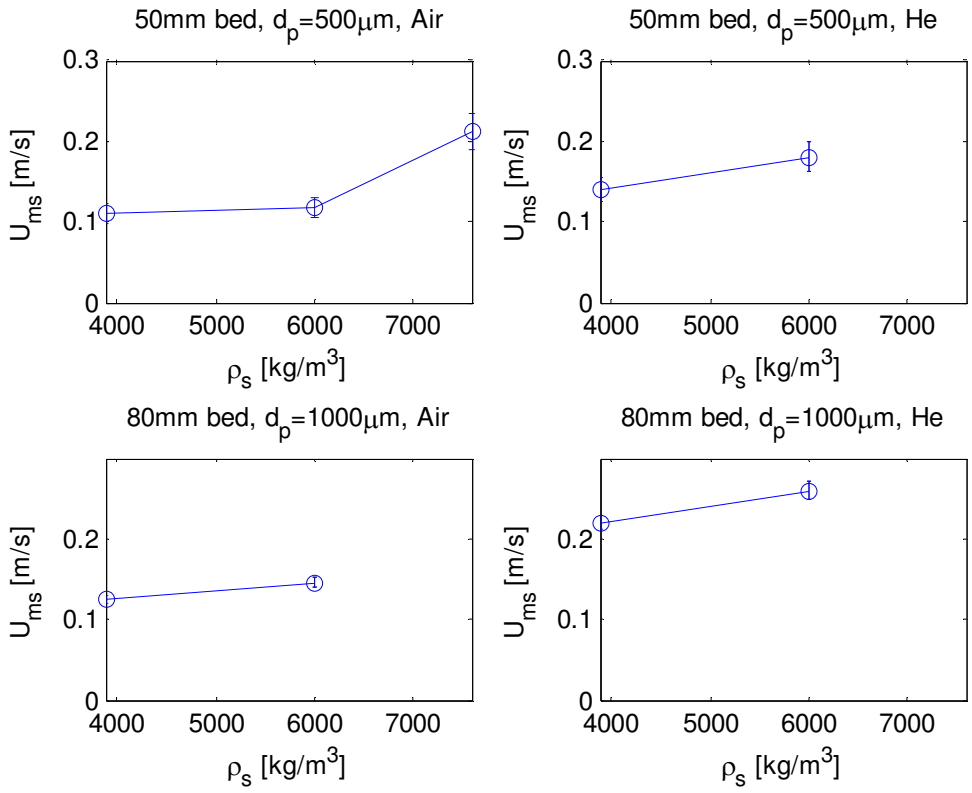

Figure A1.3: Effect of particle density on U_{ms} at H_0/D_c=0.67.

Effect of dimensionless static height (H_0/D_c) on U_{ms}

Minimum spouting velocity increases with dimensionless static bed height (see Figure A1.4) for three types of particles with different densities, as the particles start to pack toward the walls (i.e., the void fraction next to the cone walls decreases) and the drag force increases in order to elevate the particles through the spout.

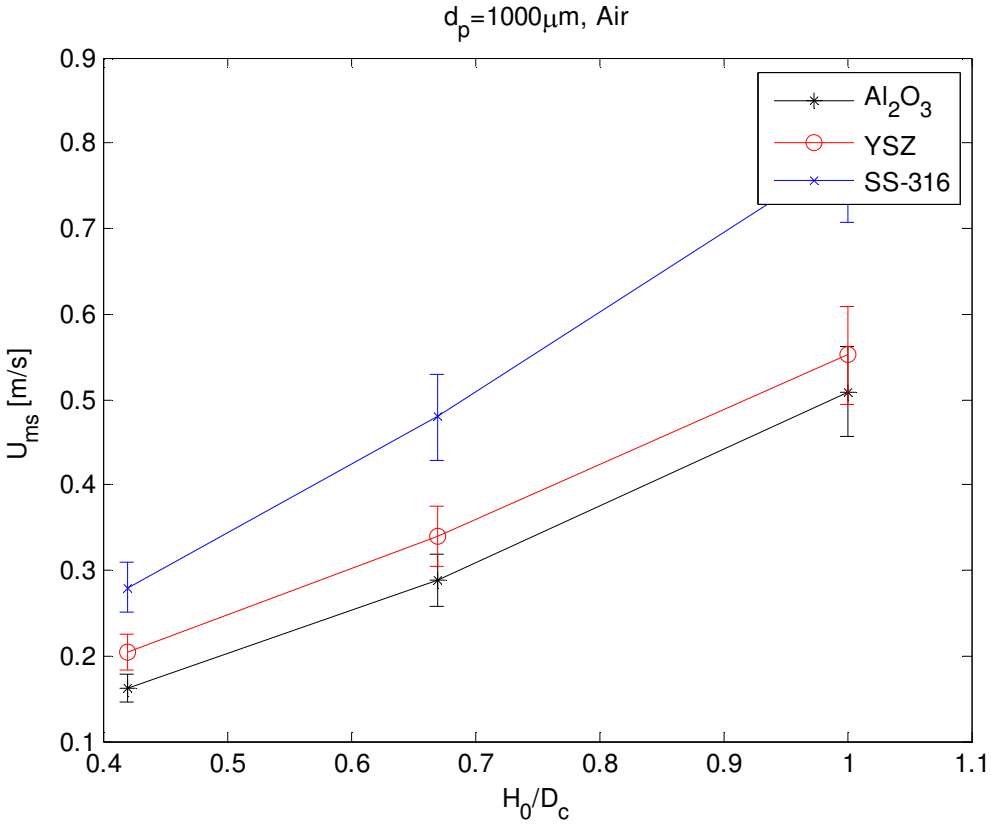

Figure A1.4: Effect of the H_0/D_c on U_{ms} for 1000 μm particles in the 50 mm bed.

Effect of gas density (ρ_g) on U_{ms}

Helium, less dense than air, was used to simulate the effect of the temperature on fluidization, as gas density decreases with increasing temperature. Figures A1.5 and A1.6 show the effect of gas density on the minimum spouting velocity for different cases. Minimum spouting velocity decreases when gas density increases due to the fact that a less-dense gas requires a larger velocity to achieve the same momentum force to suspend the particles.

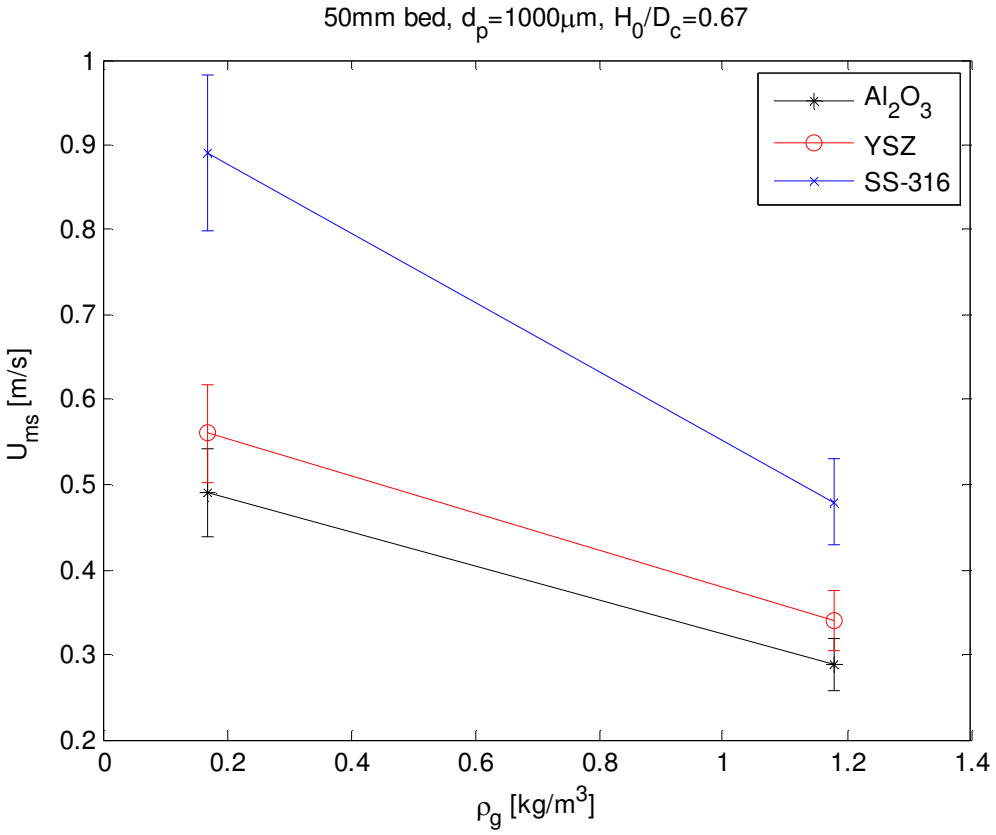

Figure A1.5: Effect of the fluidizing gas density on U_{ms} for 1000 μm particles of different density in the 50 mm bed.

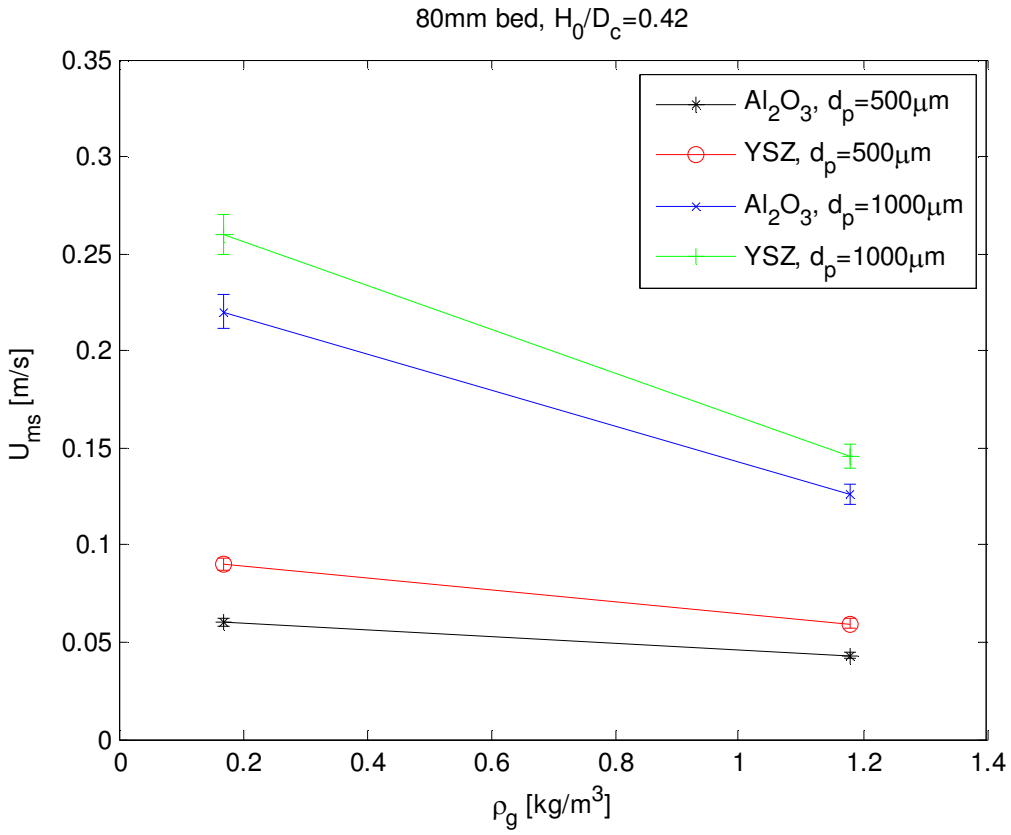

Figure A1.6: Effect of fluidizing gas density on U_{ms} for Al_2O_3 and YSZ particles of two different sizes in the 50mm bed.

Effect of particle diameter (d_p) on U_{ms}

U_{ms} increases with particle size, as can be seen in Figure A1.6. Drag force is proportional to the particle surface area per unit volume, then the larger the particle, the smaller the surface area per unit volume. Thus the drag force is reduced as particle size increases, leading to an increase in U_{ms}. In addition, the particle cross sectional area increases with particle size thus requiring the superficial gas velocity to increase too, to lift the particles.

A2. Effect of operating conditions on ΔP

Effect of column diameter (D_c) on ΔP

Bed pressure drop increases as the column diameter increases, as illustrated in Figure A2.1. This effect is due to the net quantity of particles in the bed, the more particles there is, the more difficult the gas can pass through the annulus area and fluidize the particles.

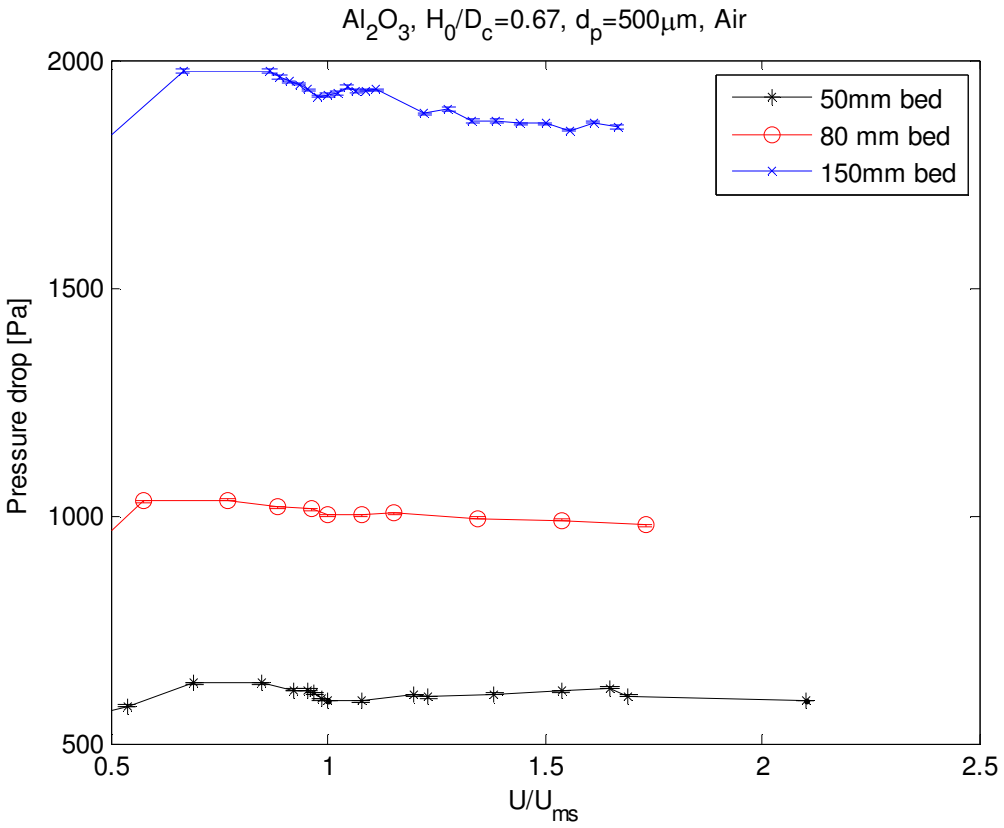

Figure A2.1: Effect of column diameter on bed pressure drop for 500 μm Al_2O_3 particles at H_0/D_c=0.67.

Effect of particle density (ρ_s) on ΔP

Figures A2.2 through A2.4 show the effect of the particle density on the bed pressure drop. Bed pressure drop increases with particle density.

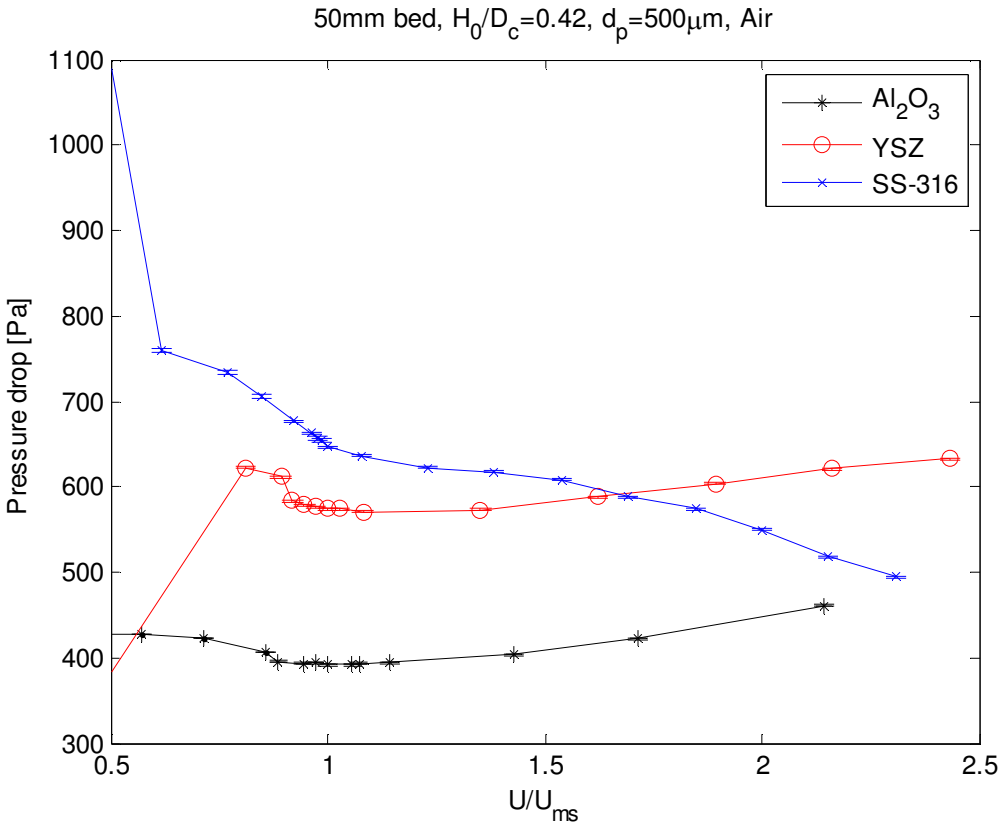

Figure A2.2: Effect of particle density on bed pressure drop for 500 μm particles at H_0/D_c=0.42 in the 50 mm bed.

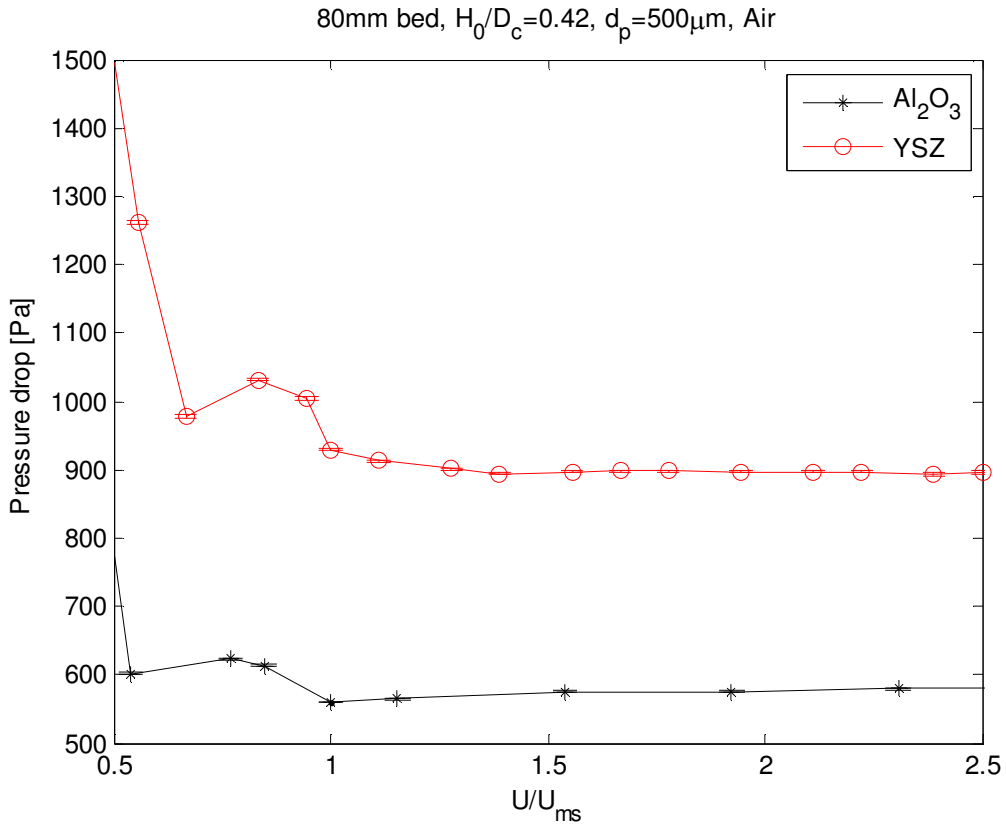

Figure A2.3: Effect of particle density on bed pressure drop for 500 μm particles at H_0/D_c=0.42 in the 80 mm bed.

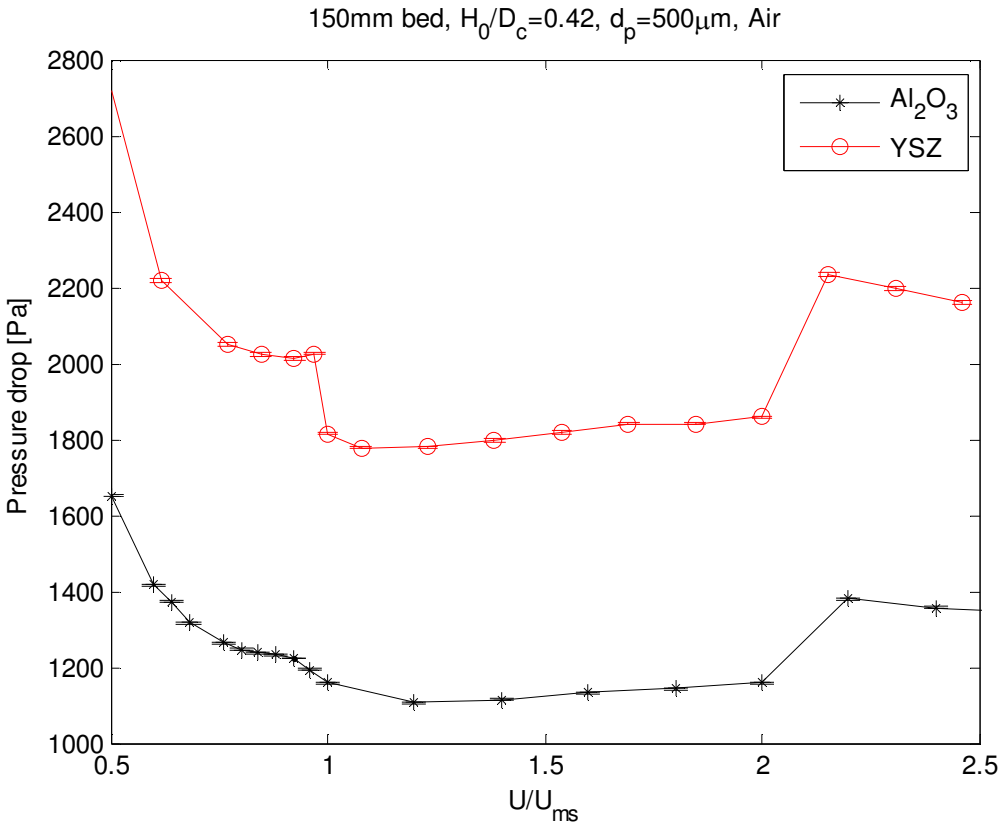

Figure A2.4: Effect of particle density on bed pressure drop for 500 μm particles at H_0/D_c=0.42 in the 150 mm bed.

Effect of gas density (ρ_g) on ΔP

Bed pressure drop increases with decreasing gas density since the lower the gas density the larger the velocity that is required to lift the particles. The difference between bed pressure drops at U_{ms} is smaller for 500 μm particles than for 2000 μm particles, as can be observed in Figures A2.5 and A2.6, respectively. This effect is due to the fact that for larger particles inertial forces become more important so that the mechanical stresses difficult more the lesser density gas flow through the particles.

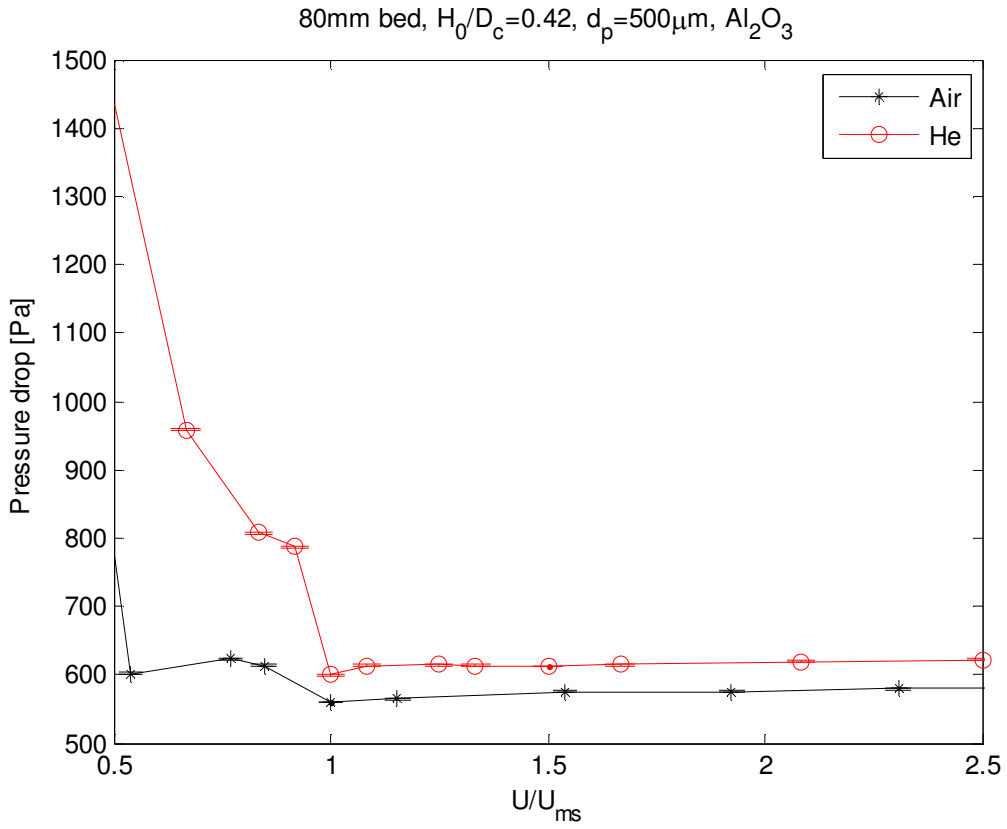

Figure A2.5: Effect of gas density on bed pressure drop for 500 μm Al_2O_3 particles at H_0/D_c=0.42 in the 80 mm bed.

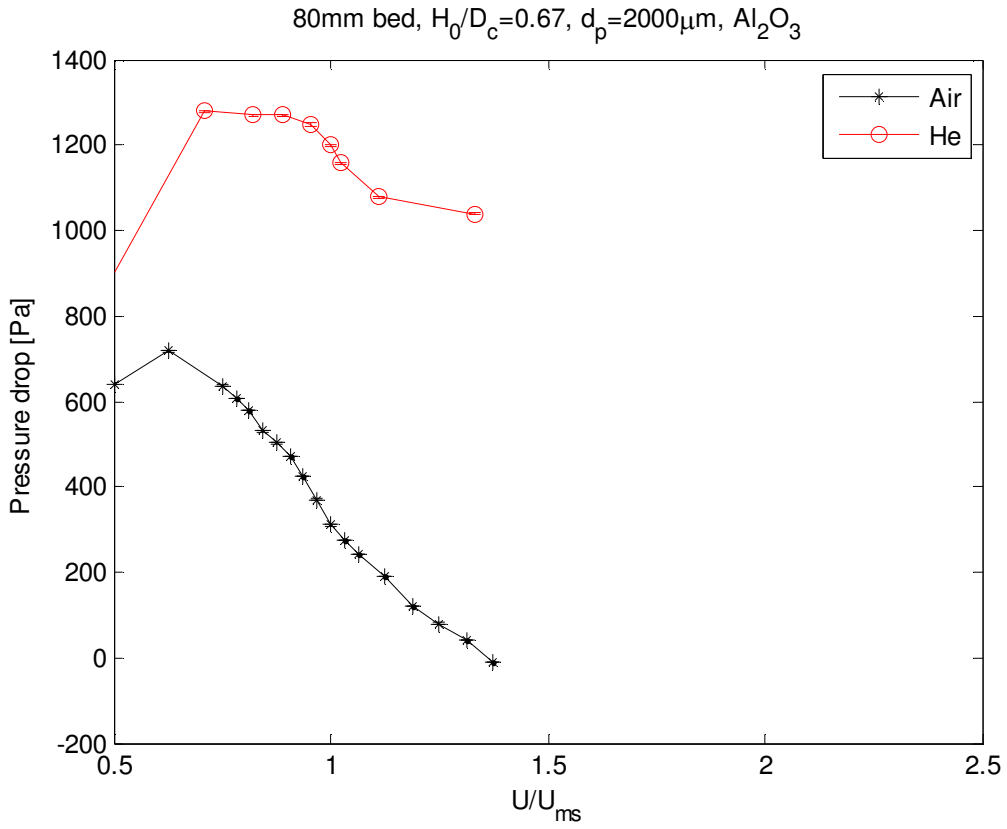

Figure A2.6: Effect of gas density on bed pressure drop for 2000 μm Al_2O_3 particles at H_0/D_c=0.67 in the 80mm bed.

Effect of dimensionless static height (H_0/D_c) on ΔP

Figure A2.7 shows the effect of dimensionless static height on the bed pressure drop. The observations indicate that the larger the static height, the larger the bed pressure drop. At higher static heights, total particle weight and wall drag interacting forces make pressure drop increase.

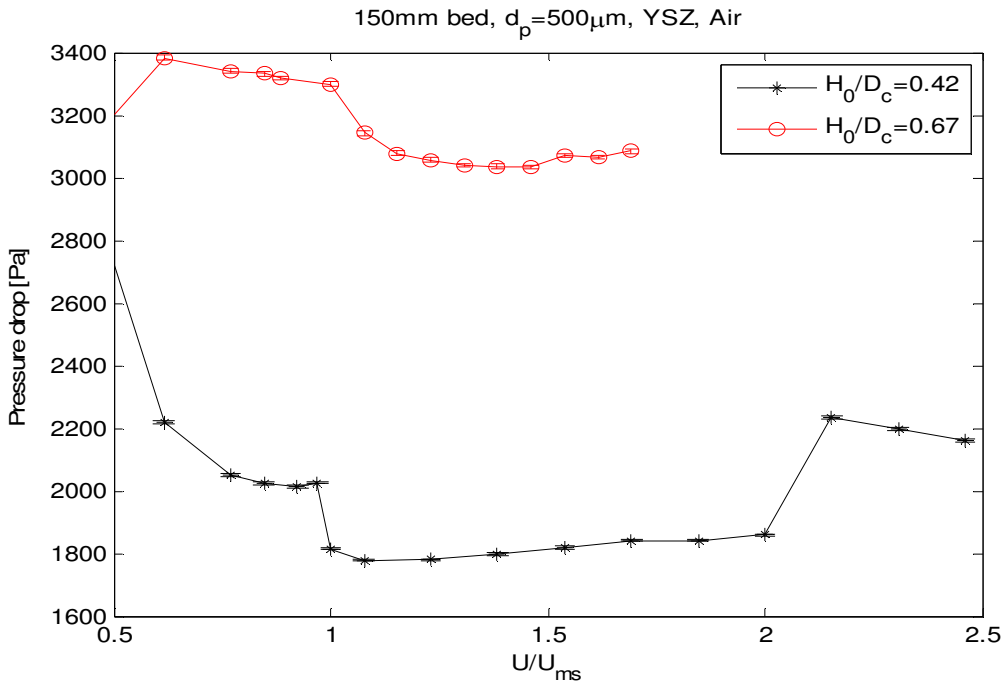

Figure A2.7: Effect of static height on bed pressure drop for 500 μm YSZ particles in the 150 mm bed.

Effect of particle diameter (d_p) on ΔP

Figures A2.8 and A2.9 show the effect of particle diameter on the bed pressure drop. In general, bed pressure drop increases with decreasing particle size. For 500 μm particles, the bed pressure drop after U_{ms} remains constant up to U/U_{ms}=2. For 1000 μm particles, the bed pressure drop decreases slowly with increasing flow. For 2000 μm particles, the bed pressure drop after U_{ms} decreases and sometimes becomes negative as the flow further increases.

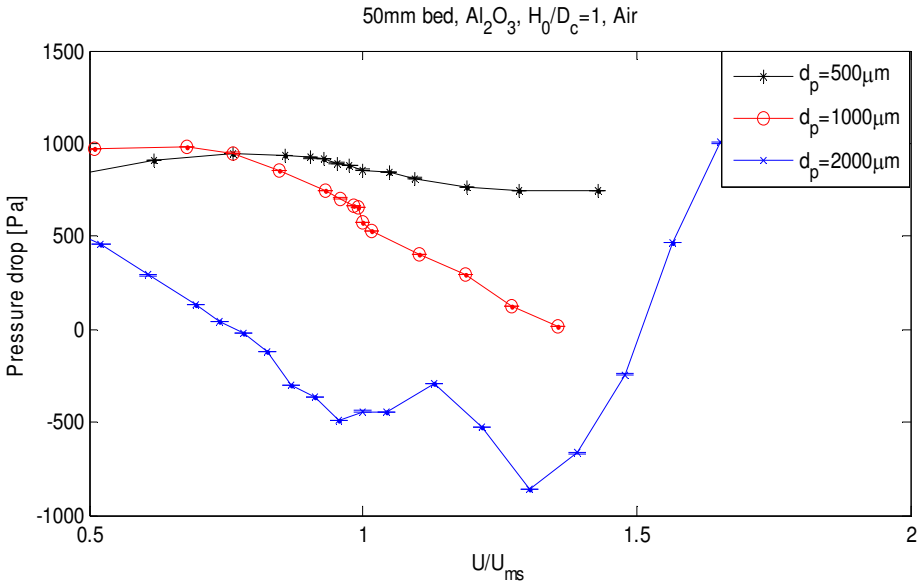

Figure A2.8: Effect of particle diameter on bed pressure drop for Al_2O_3 particles of three different diameters at H_0/D_c=1 in the 50 mm bed.

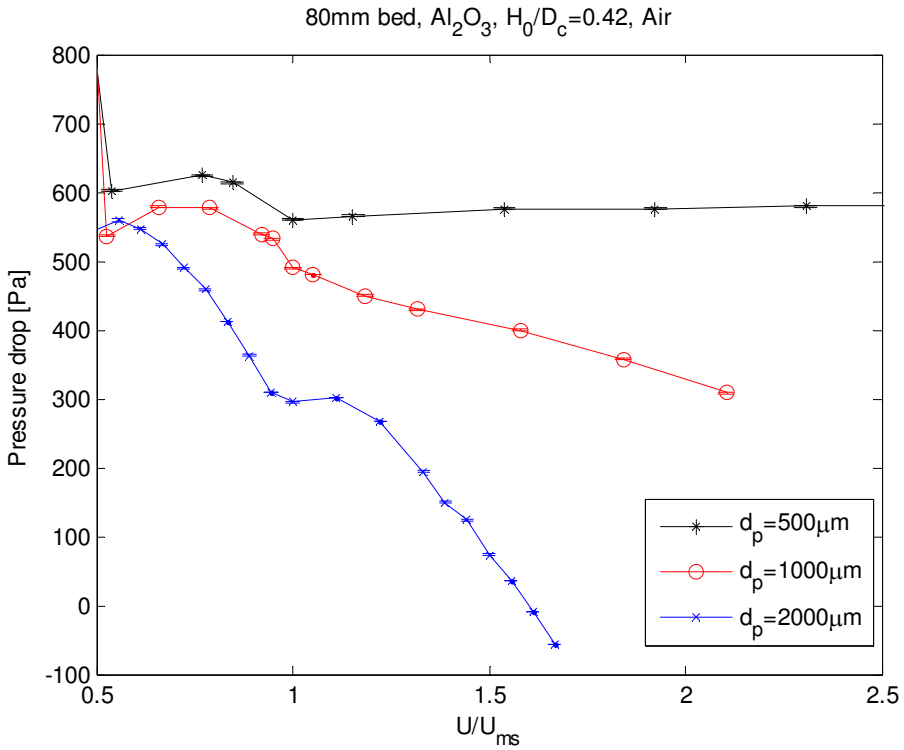

Figure A2.9: Effect of particle diameter on bed pressure drop for Al_2O_3 particles of three different diameters at H_0/D_c=0.42 in the 80 mm bed.

A3. Pressure drop behavior at different ports in the cone

Gauge pressure drop was measured at the ports shown in Figure 2.4. The observed pressure-drop behavior at these in-bed ports is similar to the pressure drop through the bed measured at Port 0, described in Section 4.1.1, which is either constant, decreasing or decreases and reaches negative values depending on the particle size, as flow increases. Generally, for the 500 µm particles, it was found that the higher the position of the port, the smaller the pressure drop (because of lower hydrostatic pressure) in complete agreement with Wang and Lim [42] and with Leu and Lo [18] for conical spouted beds. U_{ms} was defined at the point where the pressure increases abruptly while reducing the gas flow rate from a fully spouting condition to a nearly packed bed. In the observed pressure-drop record, pressure increases abruptly at U_{ms} in all ports as flow is further reduced. Therefore U_{ms} can be determined using the pressure values of any of the 5 in-bed ports.

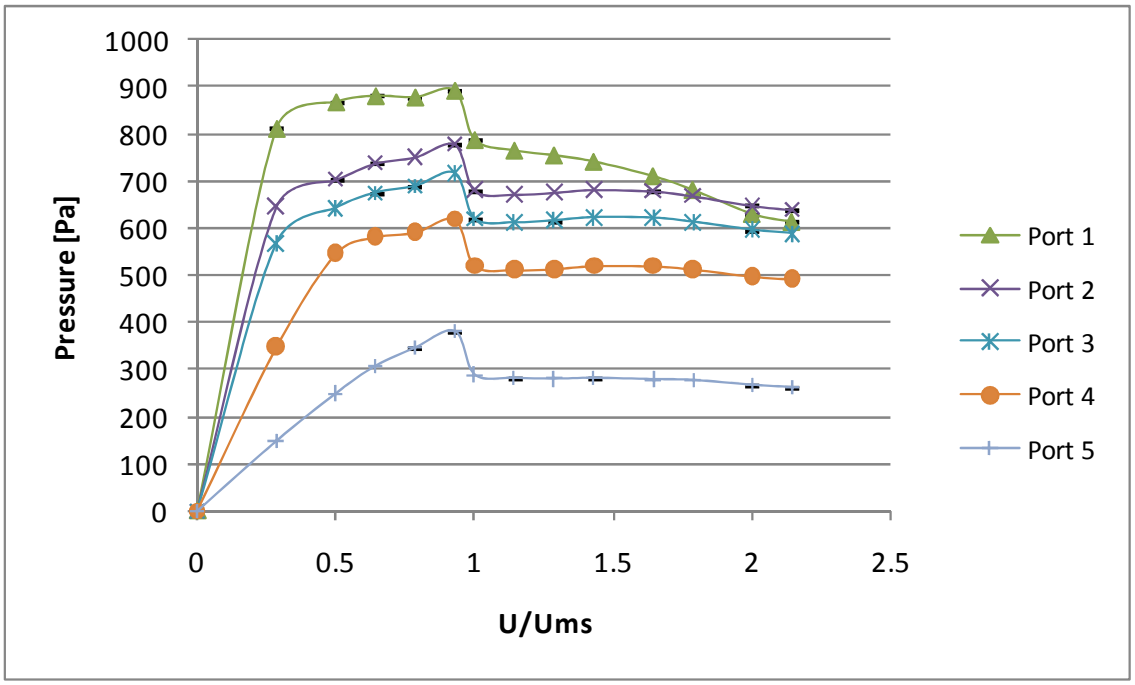

Figure A3.1: Pressure drop profiles measured in ports 1-5 in the 50 mm bed with 500 µm YSZ particles at H_0/D_c=0.67.

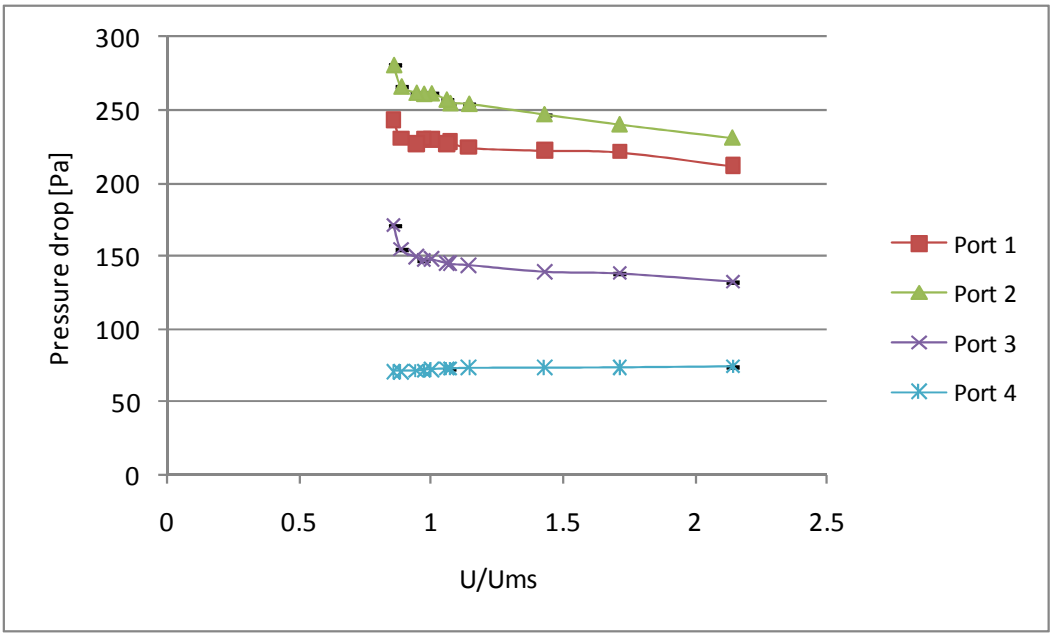

Figure A3.2: Pressure drop profiles measured in ports 1-4 in the 50 mm bed with 500 µm Al_2O_3 particles at H_0/D_c=0.42.

For 1000 µm particles, pressure slightly decreases beyond U/U_{ms}=1. While decreasing the gas flow rate from fully spouting condition to packed condition, it was observed that pressure drop increases linearly as the gas flow rate is decreased up to when U_{ms} is reached; at this point pressure drop increases nonlinearly up to a maximum value and finally decreases as the gas flow rate is further decreased (see Figure A3.3). It is noted that this trend is not clearly visible in Port 1 as in the others (because Port 1 is in the expansion area where the suction is maximum). Thus, the higher positioned port is a better port to define U_{ms}.

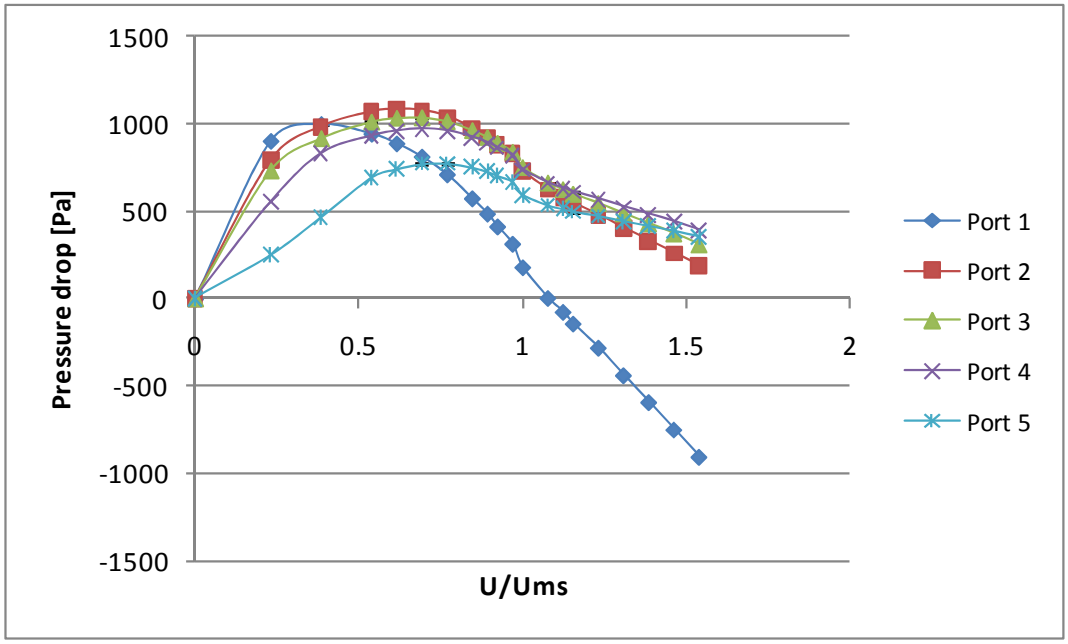

Figure A3.3: Pressure drop profiles measured in ports 1-5 in the 50 mm bed with 1000 µm YSZ particles at H_0/D_c=1.

For 2000 µm particles, suction effect was present in all ports. In Figure A3.4, the typical behavior for these particles is that the abrupt change in the pressure drop as U_{ms} is reached, as seen with 500 and 1000 µm particles, is not discernible. Thus, minimum spouting velocity could not be defined using any of those ports. For 2000 µm particles, U_{ms} was defined by visual observation of the fountain height. Notice that here the lower the position of the pressure port, the more negative values of pressure are reached. It is also remarkable that the suction effect is less drastic for the 80 mm bed (see Figure A3.5)

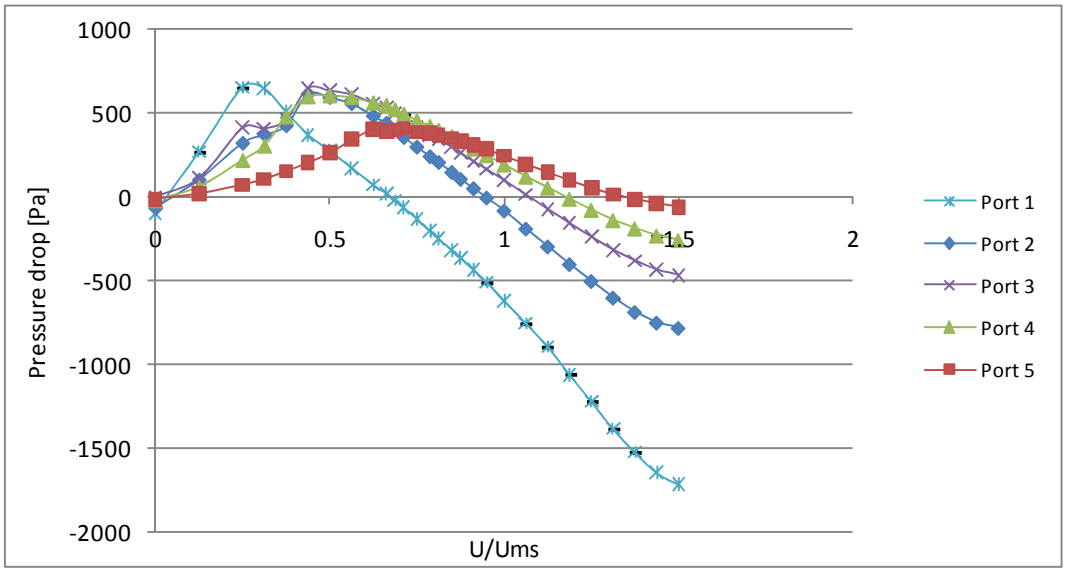

Figure A3.4: Pressure drop measured in ports 1-5 in the 50 mm bed with 2000 µm YSZ particles at H_0/D_c=0.67.

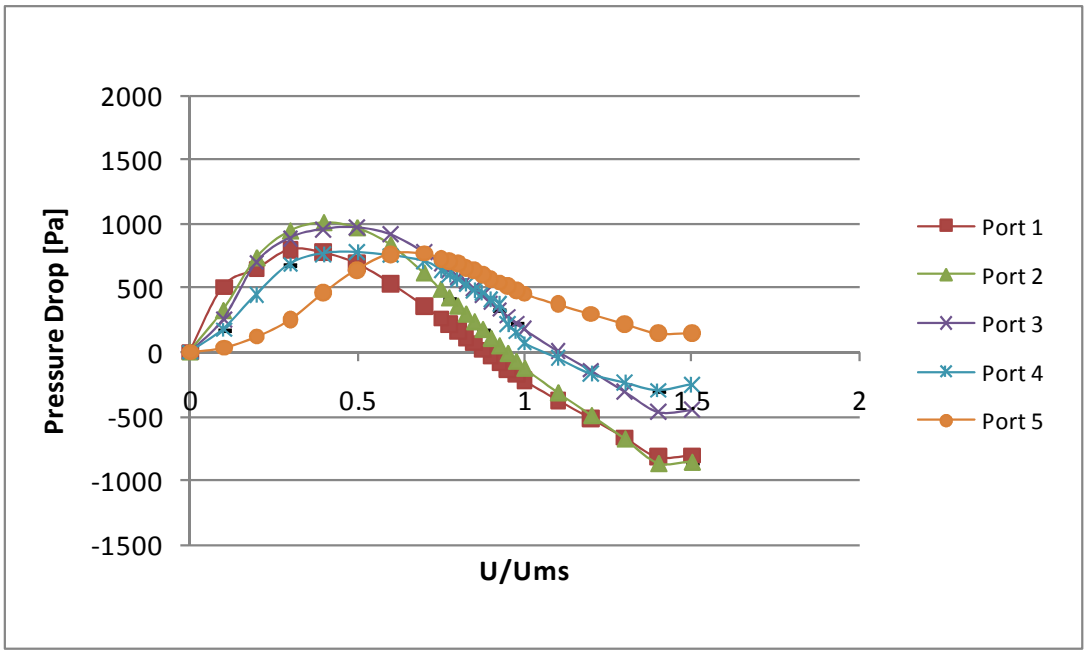

Figure A3.5: Pressure drop measured in ports 1-5 in the 80 mm bed with 2000 µm YSZ particles at H_0/D_c=0.67.

A4. Effect of operating conditions on fountain height

Effect of dimensionless static bed height (H_0/D_c) and particle density (ρ_s) on H_f

As seen in Figure A4.1, the larger the dimensionless static height and the smaller the particle density, the larger the fountain height. An interesting case is for the 500 μm particles, where the effect of particle density is apparently not significant (see Figure A4.2). This confirms the fact that for small particles, viscous forces in shallow beds are more important than for deep beds. However, for large particles, inertial forces become more important and therefore the mechanical stresses among particles make the effect of particle density more significant.

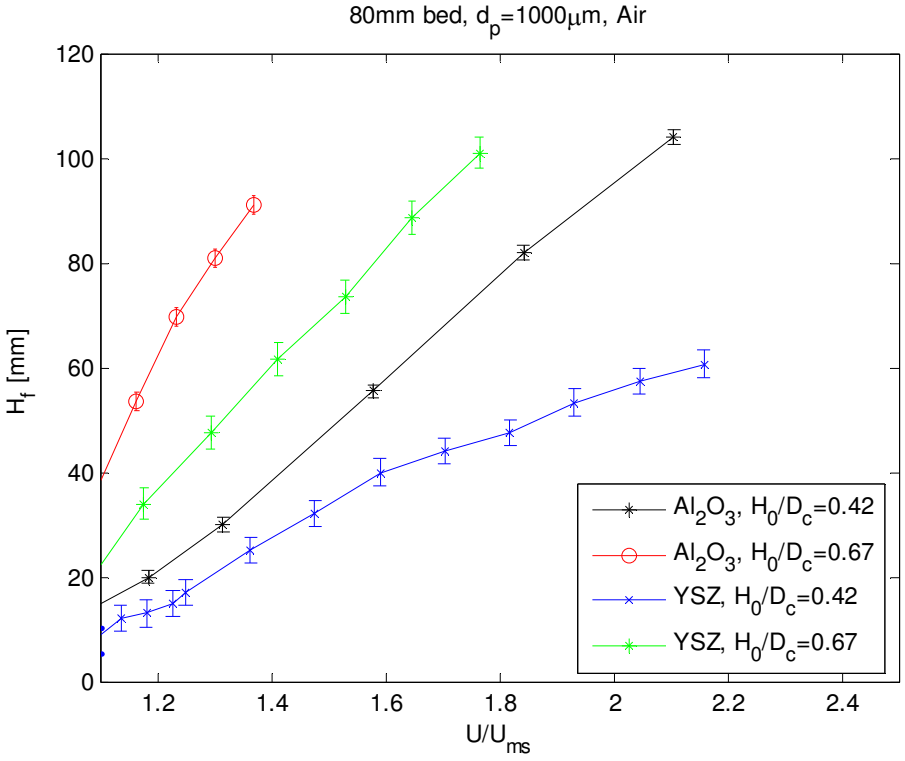

Figure A4.1: Effect of H_0/D_c and particle density on fountain height as a function of U/U_{ms} measured in the 80 mm bed at H_0/D_c=0.42 and 0.67 with 1000 μm YSZ and Al_2O_3 particles of different densities.

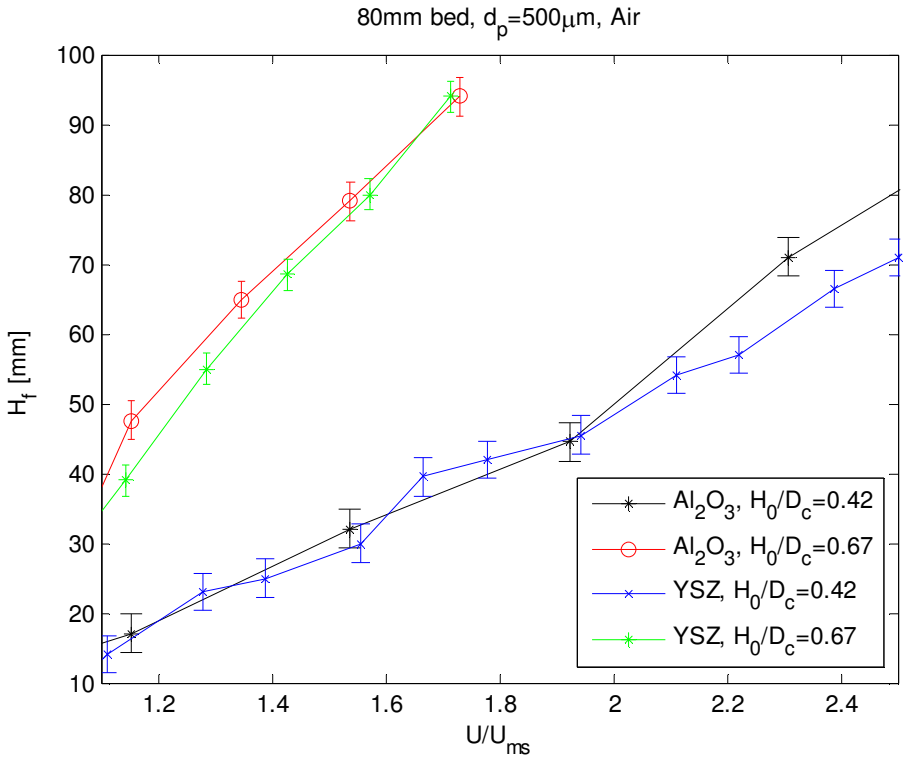

Figure A4.2: Effect of H_0/D_c and particle density on fountain height as a function of U/U_{ms} measured in the 80 mm bed at H_0/D_c=0.42 and 0.67 with 500 μm YSZ and Al_2O_3 particles of different density.

Effect of column diameter (D_c) on H_f

Figure A4.3 shows the effect of column diameter on the fountain height. The observations suggest that the larger the column diameter, the larger the fountain height everything else being equal. This effect is mainly due to the large gas flow rate required to spout a greater mass and depth of particles. However, for the 150 mm bed, the relationship between the fountain height and the gas flow rate is nonlinear due to the high dynamical variability that the fountains exhibit.

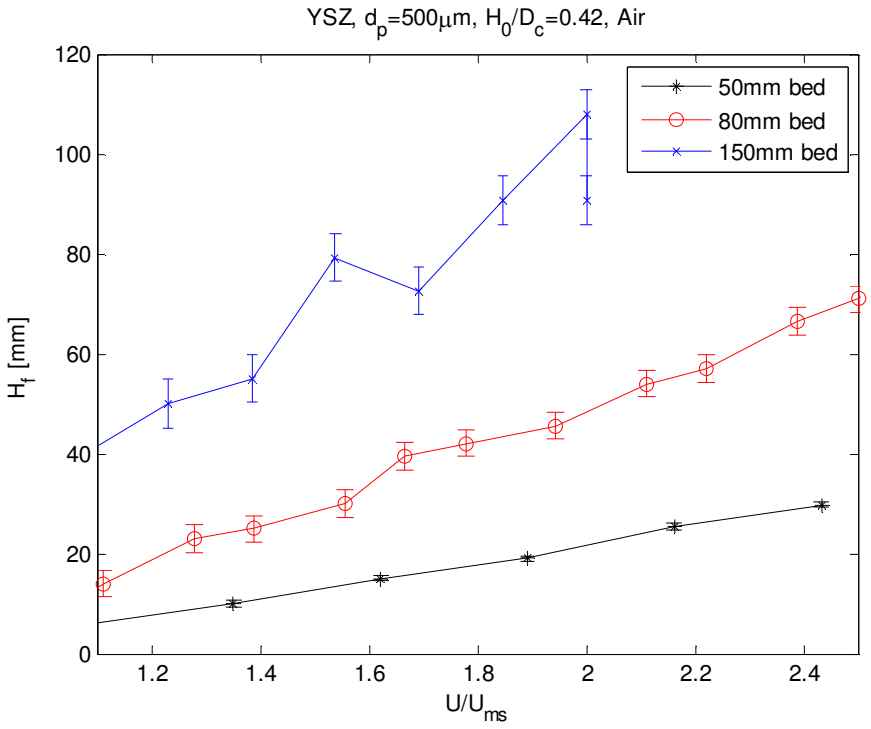

Figure A4.3: Effect of column diameter on fountain height for 500 μm YSZ particles at H_0/D_c=0.42.

Effect of gas density (ρ_g) on H_f

Figure A4.4 shows the effect of gas density on the fountain height; the larger the gas density, the larger the fountain height since the drag force increases with gas density, allowing the particles to reach higher distances through the spout zone.

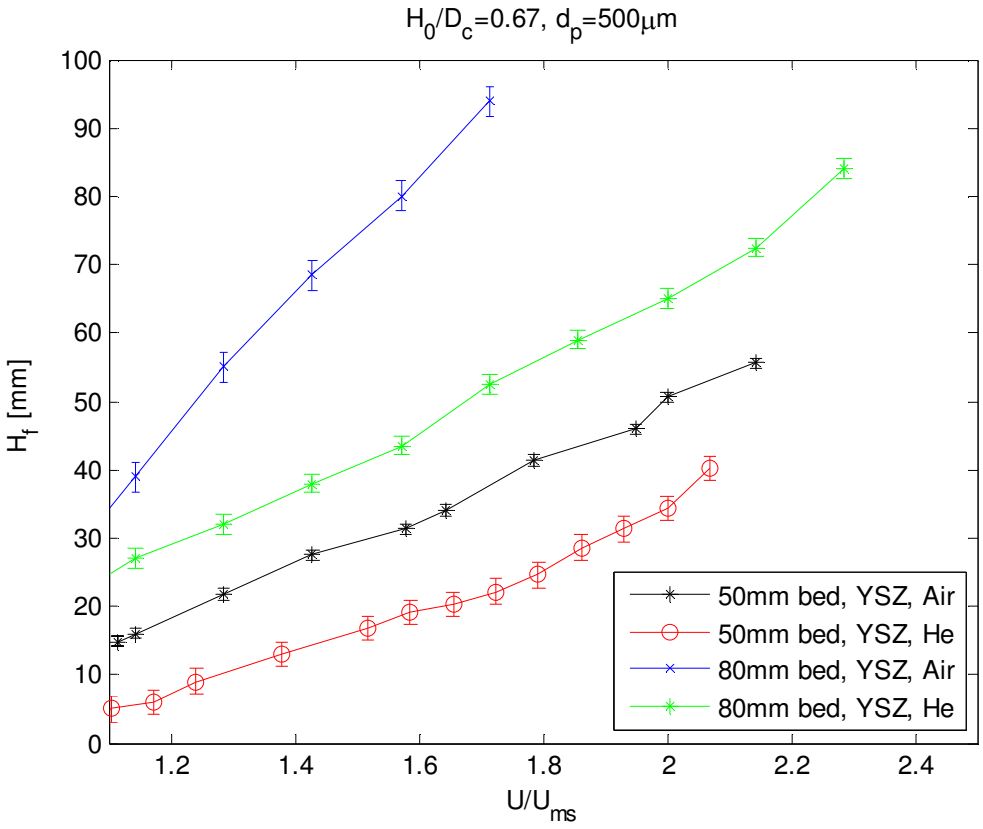

Figure A4.4: Effect of gas density on fountain height for 500μm YSZ particles.

Effect of particle diameter (d_p) on H_f

In general, fountain height increases with increasing particle diameter for shallow beds, as shown in Figure A4.5.

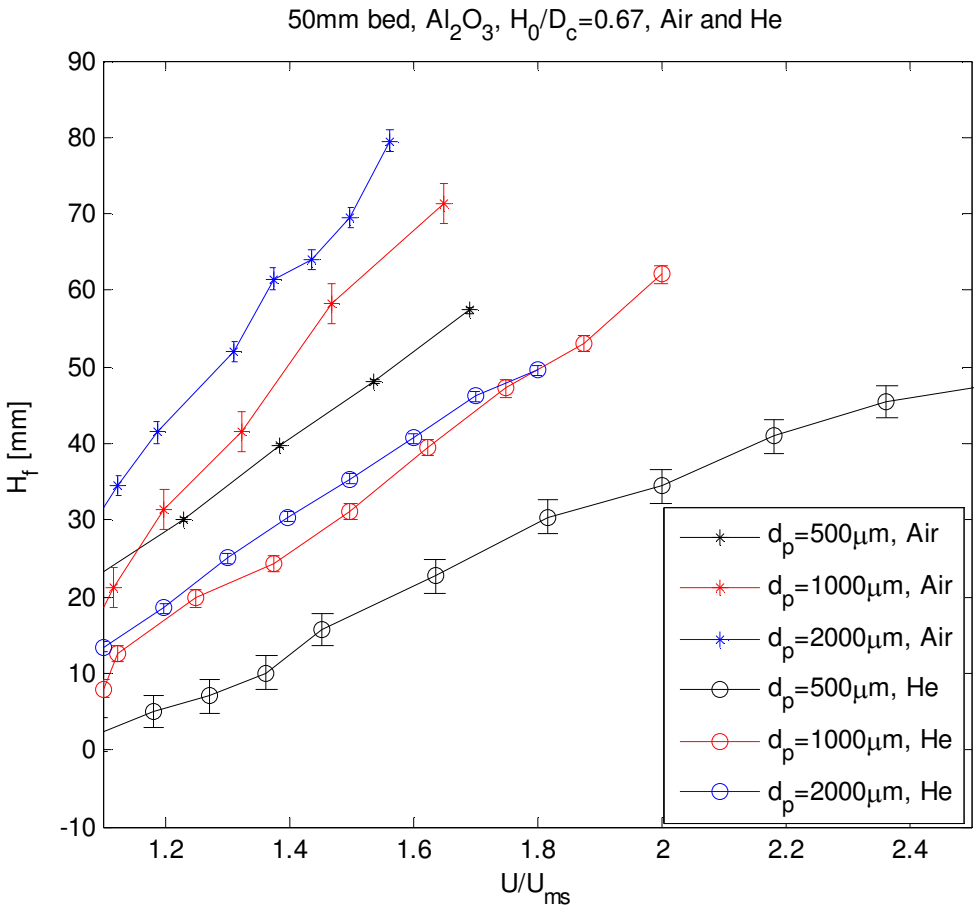

Figure A4.5: Effect of particle density on fountain height in the 50 mm bed.

APPENDIX B

Table B1.1: Bed pressure drop profiles classification and spouting regimes for the experiments performed in this investigation

D_c [mm]	ρ_s [kg/m^3]	d_p [µm]	H_0/D_c	ρ_g [kg/m^3]	U_{ms} [m/s]	ΔP_{ms} [Pa]	Bed pressure drop profile	Spouting regime
50	3880	500	0.42	1.18	0.06	408.03	Constant	Semi-regular
50	3880	500	0.67	1.18	0.11	604.23	Constant	Semi-regular
50	3880	500	1	1.18	0.18	858.18	Constant	Erratic
50	3880	1000	0.42	1.18	0.16	268.53	Decreasing	Regular
50	3880	1000	0.67	1.18	0.29	348.79	Decreasing	Regular
50	3880	1000	1	1.18	0.51	572.21	Decreasing	Regular
50	3880	2000	0.42	1.18	0.24	-64.14	Decreasing and negative	bimodal
50	3880	2000	0.67	1.18	0.68	-211.58	Decreasing and negative	Regular
50	3880	2000	1	1.18	0.98	-441.05	Decreasing and negative	Regular
50	6000	500	0.42	1.18	0.06	590.37	Constant	Regular
50	6000	500	0.67	1.18	0.12	880.71	Constant	Regular
50	6000	500	1	1.18	0.21	1126.79	Decreasing	Regular
50	6000	1000	0.42	1.18	0.20	412.63	Decreasing	Regular
50	6000	1000	0.67	1.18	0.34	516.86	Decreasing	Regular
50	6000	1000	1	1.18	0.55	841.46	Decreasing	Regular
50	6000	2000	0.42	1.18	0.32	448.33	Decreasing*	bimodal
50	6000	2000	0.67	1.18	0.68	548.58	Decreasing*	Regular
50	6000	2000	1	1.18	0.76	558.12	Decreasing*	Regular
50	7600	500	0.42	1.18	0.11	646.23	Decreasing	Regular
50	7600	500	0.67	1.18	0.21	875.00	Decreasing	Regular
50	7600	500	1	1.18	0.35	956.35	Decreasing	Regular
50	7600	1000	0.42	1.18	0.28	633.36	Decreasing	Regular
50	7600	1000	0.67	1.18	0.48	636.76	Decreasing and negative	Regular
50	7600	1000	1	1.18	0.79	230.19	Decreasing and negative	Regular
80	3880	500	0.42	1.18	0.04	559.78	Constant	Semi-regular
80	3880	500	0.67	1.18	0.09	1000.09	Constant	Semi-regular
80	3880	500	1	1.18	0.12	1442.08	Constant	Erratic
80	6000	500	0.42	1.18	0.06	929.51	Constant	Erratic
80	6000	500	0.67	1.18	0.12	1258.86	Constant	Regular
80	6000	500	1	1.18	0.21	1667.60	Decreasing	Regular
80	3880	1000	0.42	1.18	0.13	489.67	Decreasing	Regular

**Bed pressure drop decreases non linearly beyond U_{ms}*

Table B1.1: Bed pressure drop profiles classification and spouting regimes for the experiments performed in this investigation (Continued)

D_c [mm]	ρ_s [kg/m^3]	d_p [μm]	H_0/D_c	ρ_g [kg/m^3]	U_{ms} [m/s]	ΔP_{ms} [Pa]	Bed pressure drop profile	Spouting regime
80	3880	1000	0.67	1.18	0.24	636.72	Decreasing	Semi-regular
80	3880	1000	1	1.18	0.44	773.71	Decreasing	Semi-regular
80	6000	1000	0.42	1.18	0.15	776.71	Decreasing	Regular
80	6000	1000	0.67	1.18	0.28	1129.45	Decreasing	Regular
80	6000	1000	1	1.18	0.53	1579.40	Decreasing	Regular
80	3880	2000	0.42	1.18	0.31	295.25	Decreasing and negative	Regular
80	3880	2000	0.67	1.18	0.53	310.15	Decreasing and negative	Regular
80	3880	2000	1	1.18	0.87	-319.79	No data	Semi-regular
80	6000	2000	0.42	1.18	0.43	397.31	Decreasing and negative	Regular
80	6000	2000	0.67	1.18	0.66	1409.94	Decreasing and negative	Regular
150	3880	500	0.42	1.18	0.05	1160.11	Bisectionally constant	Erratic
150	3880	500	0.67	1.18	0.08	1922.00	Constant	Erratic
150	3880	500	1	1.18	0.15	2998.12	Constant	Erratic
150	6000	500	0.42	1.18	0.06	1815.27	Bisectionally constant	Erratic
150	6000	500	0.67	1.18	0.12	3299.47	Constant	Erratic
150	6000	500	1	1.18	0.18	3823.82	Decreasing	Erratic
50	3880	500	0.42	0.17	0.09	453.33	Constant	Semi-regular
50	3880	500	0.67	0.17	0.14	690.38	Constant	Semi-regular
50	3880	1000	0.42	0.17	0.27	395.40	Constant	Regular
50	3880	1000	0.67	0.17	0.49	576.11	Constant	Regular
50	3880	1000	1	0.17	0.80	558.43	Decreasing and negative	Regular
50	3880	2000	0.42	0.17	0.49	182.80	Decreasing and negative	Regular
50	3880	2000	0.67	0.17	1.23	151.57	Decreasing and negative	Regular
50	6000	500	0.42	0.17	0.12	665.64	Constant	Semi-regular
50	6000	500	0.67	0.17	0.18	1016.49	Constant	Semi-regular
50	6000	1000	0.42	0.17	0.30	581.89	Constant	Regular
50	6000	1000	0.67	0.17	0.56	897.95	Constant	Regular
50	6000	2000	0.42	0.17	0.68	607.79	Constant	bimodal
50	7600	500	1	0.17	0.56	1720.14	Constant	Erratic
50	7600	1000	0.67	0.17	0.89	692.78	Decreasing and negative	Regular

Table B1.1: Bed pressure drop profiles classification and spouting regimes for the experiments performed in this investigation (Continued)

D_c [mm]	ρ_s [kg/m^3]	d_p [μm]	H_0/D_c	ρ_g [kg/m^3]	U_{ms} [m/s]	ΔP_{ms} [Pa]	Bed pressure drop profile	Spouting regime
80	3880	500	0.42	0.17	0.06	619.85	Constant	Semi-regular
80	3880	500	0.67	0.17	0.13	1109.46	Constant	Semi-regular
80	3880	500	1	0.17	0.17	1746.45	Constant	Erratic
80	6000	500	0.42	0.17	0.09	1030.58	Bisectionally constant	Semi-regular
80	6000	500	0.67	0.17	0.17	1396.63	Constant	Semi-regular
80	6000	500	1	0.17	0.23	2405.72	Bisectionally constant	Erratic
80	3880	1000	0.42	0.17	0.22	556.14	Constant	Regular
80	3880	1000	0.67	0.17	0.41	742.37	Constant	Regular
80	3880	1000	1	0.17	0.70	1284.84	Decreasing	Regular
80	6000	1000	0.42	0.17	0.26	907.56	Constant	Regular
80	6000	1000	0.67	0.17	0.46	1327.22	Constant	Regular
80	6000	1000	1	0.17	0.82	1947.69	Decreasing	Regular
80	3880	2000	0.67	0.17	1.08	1199.42	Decreasing	Regular
80	6000	2000	0.67	0.17	1.25	1733.49	No data	Regular

VITA

Irma Deytia Lima Rojas was born in Mexico City on March 8, 1976. She attended the university "Universidad Autonoma Metropolitana" in Mexico majoring in energy engineering. She received her Bachelor degree in Energy Engineering in June 1998. After graduating, she started to work for an energy consulting firm in Mexico up to 1999, and from there she started her carrier as a researcher in the Research Electrical Institute of Mexico until 2005. Then, she began her PhD in Chemical Engineering in the University of Tennessee-Knoxville in August 2005.